



**HAL**  
open science

## Deterioration processes and modelling in urban drainage systems

S. Barraud, E H L R Bosco, François H L R Clemens-Meyer, Gersende Fernandes, Y. Le Gat, C. de Haan, R.A. Luimes, K. Makris, F.A.M. Rooyackers, I.C. Scheperboer, et al.

### ► To cite this version:

S. Barraud, E H L R Bosco, François H L R Clemens-Meyer, Gersende Fernandes, Y. Le Gat, et al.. Deterioration processes and modelling in urban drainage systems. Frédéric Cherqui; François Clemens-Meyer; Franz Tscheikner-Gratl; Bert van Duin. Asset Management of Urban Drainage Systems, IWA Publishing, pp.131-230, 2024, 9781789063059. 10.2166/9781789063059\_0131 . hal-04797670

**HAL Id: hal-04797670**

**<https://hal.science/hal-04797670v1>**

Submitted on 22 Nov 2024

**HAL** is a multi-disciplinary open access archive for the deposit and dissemination of scientific research documents, whether they are published or not. The documents may come from teaching and research institutions in France or abroad, or from public or private research centers.










L'archive ouverte pluridisciplinaire **HAL**, est destinée au dépôt et à la diffusion de documents scientifiques de niveau recherche, publiés ou non, émanant des établissements d'enseignement et de recherche français ou étrangers, des laboratoires publics ou privés.



Distributed under a Creative Commons Attribution - NonCommercial - NoDerivatives 4.0 International License

## Chapter 5

# Deterioration processes and modelling in urban drainage systems

S. Barraud<sup>1</sup>, E. Bosco<sup>2</sup>, F.H.L.R. Clemens-Meyer<sup>3,4</sup>, G. Fernandes<sup>5</sup>, Y. Le Gat<sup>6</sup>, C. de Haan<sup>7</sup>, R.A. Luimes<sup>2</sup>, K. Makris<sup>8</sup>, F.A.M. Rooyackers<sup>2</sup>, I.C. Scheperboer<sup>9</sup>, J. Skjelde<sup>10</sup> and A.S.J. Suiker<sup>2</sup>

<sup>1</sup>University of Lyon, Insa Lyon, DEEP, 1 1 Rue de la Physique, F-69621 Villeurbanne Cedex, France

<sup>2</sup>Department of the Built Environment, Eindhoven University of Technology, PO Box 513, 5600 MB Eindhoven, The Netherlands

<sup>3</sup>Department of Civil and Environmental Engineering, Norwegian University of Science and Technology, PO Box 8900, NO-7491 Trondheim, Norway

<sup>4</sup>SkillsInMotion BV, Esdoornlaan 11, 43454 HH De Meern, The Netherlands

<sup>5</sup>Univ Lyon, Université Claude Bernard Lyon 1, CNRS, ENTPE, UMR 5023 LEHNA, F-69518 Vaulx-en-Velin, France

<sup>6</sup>INREA-ETTIS, 50 avenue de Verdun, 33612 Cestas Cedex, France

<sup>7</sup>De Haan Watersolutions, Javastraat 104A, 6524 MJ Nijmegen, The Netherlands

<sup>8</sup>Partners4UrbanWater, Graafseweg 274, 6532 ZV Nijmegen, The Netherlands

<sup>9</sup>IKT Nederland, Tivolilaan 205, 6824 BV Arnhem The Netherlands

<sup>10</sup>COWI AS, PO Box 4220 Torgarden, N-7436 Trondheim, Norway

### ABSTRACT

This chapter discusses and assesses processes underlying the loss of functionality of (elements) of urban drainage systems. The chapter does not pretend to cover all literature nor do the authors claim to cover all processes involved. As the body of literature experiences a rapid growth, the authors want to provide the reader a comprehensive overview of the literature to-date to be used as an entry for further exploration. Several processes are described and the possibility to model them in a deterministic manner is discussed. The last sections provide a brief introduction to the use of statistical models based on condition classes (as is applied in practice) along with a brief overview of advancements made in machine learning applications.

**Keywords:** processes, timescales, deterioration, modelling.

| Symbol*   | Description                      | Units             |
|-----------|----------------------------------|-------------------|
| $E_c$     | Young's modulus (concrete)       | N/mm <sup>2</sup> |
| $G$       | Gravitation acceleration         | m/s <sup>2</sup>  |
| $G_{I,c}$ | Mode I toughness                 | N/mm <sup>2</sup> |
| $H$       | Capillar pressure head, height   | m                 |
| $H$       | Hydraulic head                   | m                 |
| $i(t)$    | Infiltration as function of time | m/s               |

(Continued)

© 2024 IWAP. This is an Open Access book chapter distributed under the terms of the Creative Commons Attribution License (CC BY-NC-ND 4.0) which permits copying and redistribution for non-commercial purposes with no derivatives, provided the work is properly cited (<https://creativecommons.org/licenses/by-nc-nd/4.0/>). The chapter is from the book *Asset Management of Urban Drainage Systems: if anything exciting happens, we've done it wrong!*, Frédéric Cherqui, François Clemens-Meyer, Franz Tschekner-Gratl and Bert van Duin (Editors).

| Symbol*    | Description                          | Units             |
|------------|--------------------------------------|-------------------|
| $I$        | Cumulated infiltration               | m                 |
| $K_s$      | Hydraulic conductivity at saturation | m/s               |
| $M$        | Shape parameter                      | —                 |
| $M_w$      | Water mass                           | kg                |
| $M_s$      | Solid mass                           | kg                |
| $N$        | Shape parameter                      | —                 |
| $R$        | Radius                               | m                 |
| $R$        | Isotope ration                       | —                 |
| $T$        | Time                                 | s                 |
| $Q$        | Flux                                 | m <sup>3</sup> /s |
| $Q(t)$     | Flow rate as function of time        | m <sup>3</sup> /s |
| $S$        | Surface area                         | m <sup>2</sup>    |
| $S_e$      | Effective saturation                 | —                 |
| $V_a$      | Air volume                           | m <sup>3</sup>    |
| $V_f$      | Fluid volume                         | m <sup>3</sup>    |
| $V_t$      | Total soil volume                    | m <sup>3</sup>    |
| $V_w$      | Water volume                         | m <sup>3</sup>    |
| $Z$        | Elevation                            | m                 |
| $\alpha$   | Empirical parameter, surface tension | m <sup>-1</sup>   |
| $\phi$     | Porosity                             | —                 |
| $\theta$   | Volumetric water content             | —                 |
| $\theta_r$ | Water content at saturation          | —                 |
| $\theta_s$ | Saturation                           | —                 |
| $\rho$     | Mass density                         | kg/m <sup>3</sup> |
| $\rho_b$   | Dry bulk density                     | kg/m <sup>3</sup> |
| $\rho_p$   | Particle density                     | kg/m <sup>3</sup> |

\*Other symbols are explained in the text where appropriate.

## 5.1 INTRODUCTION AND LAYOUT OF THE CHAPTER

Often the term ‘ageing processes’ is used in practice when it comes to describe changes in systems’ functionality and connected asset management (AM) activities. The use of ageing has an implicit meaning attached, as it suggests these processes are all time driven, which to a certain extent is correct. However, it does not imply that all processes involved can be modelled as if they are *continuous* in time or are inherently time dependent. To avoid this bias, we will use the term *deterioration process* in this chapter.

Deterioration refers to a spectrum of processes, or sequences of events, that affect the functionality of either elements in a system, part of a system or a system as a whole. Such a definition encompasses a very wide range of topics. The present chapter does not pretend to cover all possible processes, or combination of processes that may be relevant in the context of urban drainage (UM). The reason for this is simple: we cannot be sure we are aware of all processes that contribute to deterioration, but we are aware that, when it comes to the processes we are familiar with, knowledge is limited at best (i.e., there is a variety of known or suspected unknowns, and most likely a lot of unknown unknowns as well). A further complication is the diversity of processes encountered: physical, chemical, and biological processes and combinations or sequences of these, sometimes in concert with a dose of

human ignorance, are all in play. In addition, our systems consist of very diverse parts ranging from pipes to nature-based solutions (NBS) and, therefore, the diversity of failure mechanisms would overwhelm the scope of this book.

Consequently, this chapter merely tries to provide the reader with a selective overview of processes involved in deterioration in terms of characteristics (like time scales involved, or how to recognize a certain process or chain of events leading to a loss of functionality), introducing the very wide field of deterioration processes and associated models, touching upon statistical and deterministic models highlighting their strong and weak points. [Sections 5.2](#) and [5.3](#) discuss the infiltration and clogging processes that are of importance in many NBS that have been implemented over the past few decades. [Sections 5.4](#), [5.5](#), [5.6](#) and [5.7](#) discuss a range of ageing processes linked to PVC and concrete pipes (i.e., the most popular materials applied in UD) along with a range of processes influencing the properties of materials. Further processes like sedimentation, formation of FOG (i.e., fats, oils and grease) deposits is discussed, illustrated with case studies where available or appropriate. For some aspects comprehensive textbooks are available; for example, in the case of sewer sediments the reader is referred to [Ashley \*et al.\* \(2004\)](#), where it comes to micro-biological processes the reader is referred to [Hvitved-Jacobsen \*et al.\* \(2013\)](#).

[Section 5.8](#) presents processes involved in loss of hydraulic capacity, while [Section 5.9](#) goes into separation of flows and why they tend to keep mixing. [Section 5.10](#) presents an introduction to statistical modelling of (piped) UD systems as there is not yet sufficient data available for NBS to merit such an approach. This is the most applied approach in practice although some understanding or knowledge of the underlying processes can be beneficial. A good understanding of these processes is critical when making decisions about AM activities (e.g., when the reasons for failure of an element are clear, this knowledge tends to provide important information on how to remedy the failure and at what time scale action should be taken; statistical models do not provide that sort of information). In [Section 5.11](#) a brief overview of the application of machine learning techniques for deterioration modelling in Urban Drainage Asset Management (UDAM) is provided.

Statistical models are typically based on a set of reference images that allow for the identification and scoring of defect types, and subsequently the identification of a condition class (often from 0 to 5) indicating their 'hazard' level, with the lowest (or highest depending on the standard) condition class indicating an (almost) complete loss of functionality. This approach is basically descriptive, solely looking at the end result of an unknown number of deterioration processes. No information is obtained that allows for the quantification of a loss of functionality, for example, Class 4, which is caused by corrosion, does not denote the hydraulic roughness of a pipe wall nor the remaining 'healthy' material, nor the actual mechanical properties of the construction material.

This may be seen as the main reason that, for all practical purposes in UDAM, deterioration is modelled as a time-dependent process using statistical models that use a pool of (visual) observations to make prediction on the development of the condition class of elements for planning purposes (see e.g., [Caradot \*et al.\*, 2020](#)). Nevertheless, detailed deterministic descriptions of process and subsequent modelling of some of the processes involved in deterioration are available and can be used in AM to a certain extent. Their added value is found in:

- Knowledge of time and space scales of processes can be beneficial when judging a given situation.
- Understanding which processes may be responsible for the evolution of the technical state in a given situation, allowing for identifying and possibly removing the cause of the deterioration.

Given the complexity and the apparent lack of detailed knowledge, using very detailed deterioration models for practical applications seems unrealistic. Instead, a considerable body of literature is available on statistical models describing 'ageing' based on inspection data. For instance, applying condition classes discussed in Chapters 4 and 8. Apart from the complexity and limitations with respect to practical applicability, there are strong indications that processes occur in UD which are chaotic by nature. This implies that there is a fundamental limit regarding the prediction horizon of models representing these



processes (e.g., rainfall, rainfall-runoff processes or the transport of solid objects in complex flow fields that occur in UD systems [see e.g., [Rodrigues-Iturbe et al. 1989](#); [Sivakumar et al. 2009](#), or [Duinmeijer and Clemens, 2021](#)]). To complicate matters even more, deterioration of UD systems may well be the result of failure of other urban infrastructures (see e.g., [van Riel, 2016](#)). This aspect, however, will not be addressed in this chapter to limit the scope as to what reasonably can be covered.

The interested reader who wants to keep up with the developments in the field is referred to the proceedings of the IWA/IAHR conference series *Sewer Processes and Networks* that is organized on a regular basis by the Working Group on Sewer Processes and Networks (<https://www.sspwg.org/>) and the activities of the IWA/IAHR working group on Urban Drainage Asset Management (<https://udam.home.blog/>)

## 5.2 INFILTRATION

### 5.2.1 Introduction

The process of infiltration is one of the key processes in UD systems, even in the classical (pipelined) systems where infiltration plays a role in the rainfall-runoff process. It is a major component of recently developed concepts such as 'sponge cities' (see e.g., [Jiang et al., 2018](#)). In fact, in many NBS, infiltration is the essential process that is relied upon. It must be realized however that the quantification of the infiltration capacity is not straight forward and is inhomogeneous in time and space. A further aspect of infiltration is clogging which can be seen as the main factor that reduces the infiltration capacity over time.

Infiltration systems such as infiltration basins, raingardens, bioretention systems, swales, trenches, filter strips, soil cells with trees or shrubs, permeable pavements and so on have become widely implemented in urban strategies to manage stormwater over the past few decades.

They are recognized to provide significant benefits. For instance, they contribute to flood reduction when they are part of integrated stormwater management strategies ([Davis et al., 2012](#); [Petrucci, 2012](#)). They reduce the degradation of receiving water bodies (i.e., through smaller volumes of water and associated pollutant loads that are directly discharged), help to restore baseflows, which in some cases can be depleted due to urbanization ([Hamel & Fletcher, 2014](#); [Kauffman et al., 2009](#); [Smakhtin 2001](#)) and can contribute to groundwater recharge ([Bonneau et al., 2018](#)). When designed as NBS using vegetation, they also provide multiple co-benefits like enhanced landscape aesthetics, biodiversity preservation or creation and mitigation of the urban heat island ([Oral et al., 2020](#)).

While they have become increasingly implemented, a recurrent issue is their durability over time, particularly due to the potential decrease in their permeability, which can jeopardize:

- (1) Their hydraulic functioning. If clogging occurs, less water can be infiltrated, possibly resulting in permanent ponding and associated urban flooding.
- (2) Their performance in terms of water quality. As already mentioned, an infiltration device is effective in stormwater treatment as a result of both hydrological processes (i.e., reduction of stormwater volume discharged to receiving water bodies leading to a reduced discharge of pollutants transported by the runoff) as well as physical and chemical processes (such as filtration, adsorption or precipitation) that occur during the percolation of water through a substratum or a soil. When clogging occurs, less water can be infiltrated, and the excess water is diverted or remains at the surface without treatment.
- (3) Their aesthetic aspect and other uses of the space. Standing water is not only unaesthetic but it can also compromise the other uses of the space taken up by these assets when they are multifunctional. It can negatively impact vegetation and, if the water remains too long on the surface, it could contribute to the proliferation of mosquitoes ([Al-Rubaei et al., 2015](#); [Valdelfener et al., 2018](#)). However, this potential proliferation only occurs when standing water remains for at least 5 days ([Valdelfener et al., 2018](#)).

### 5.2.2 Soils

The Food and Agriculture Organization of the United States defines soils as ‘a natural body consisting of layers (soil horizons) that are composed of weathered mineral materials, organic material, air and water. Soil is the product of the combined influence of climate, topography, organisms (flora, fauna and human) on parent materials (original rocks and minerals) over time. As a result, soil differs from its parent material in texture, structure, consistency, colour, chemical, biological and physical characteristics.’ Soil thus is a living medium, at the interface between the atmosphere and the bedrock.

Soil provides numerous ecosystem services such as nutrient cycling, provision of food, fibre, fuel and construction materials. It also has hydrological functions such as storing water for plants and fauna, regulating the water cycle including reducing floods, regulating the climate (mainly by evapotranspiration) and adsorbing and/or facilitating the breakdown of pollutants which limits groundwater contamination. However, human activities tend to negatively impact its quantity and quality as both freshwater and soil are increasingly consumed by the increasing number of humans. The Intergovernmental Panel on Climate Change report (Olsson *et al.*, 2019) on climate change and land shows that human activity has caused soil degradation on about 25% of the Earth’s surface not covered by ice. For example, with monoculture, biodiversity and fertility of soil disappear and the soil surface is less strong and stable (Kutílek & Nielsen, 2015).

Soil is composed of gas, liquid and solid. The liquid and gas phases represent 30–60% of the soil volume. Some air is maintained in the soil, with a slightly different composition from the atmosphere. When water enters the unsaturated part of soil (i.e., the so-called vadose zone), the air within the pores is pushed away and replaced by water. Water can be found in soils in its liquid phase incorporating dissolved compounds. Its quantity and quality vary in the soil on both temporal and spatial scales as the result of climate, hydrological and paedological processes.

As a result of its granular nature, a soil can be seen as an assembly of particles (Figure 5.1). Basically, soils may be differentiated by two key characteristics: their texture and structure. The texture depends on both the type and shape of particles, differentiated according to their mean diameter size. According to the United States Department of Agriculture soil texture classification, clays have a diameter smaller than 0.002 mm, silt between 0.002 and 0.05 mm, and sand between 0.05 and 2 mm. In addition to the differences in size and shape of the particles, their packing is often irregular, creating the voids and channels that make up the pores (Figure 5.1), which is measured by the porosity (Table 5.1). The arrangement of the particles in the soil creates its structure. These two characteristics greatly influence the movement of water into and through the soil.

Soils can be analysed by measuring different parameters such as porosity, water content and effective saturation (Table 5.1).

The total porosity can be determined knowing the dry bulk density of the soil: in the field, a known volume of soil is excavated and then weighed, dried 24 h at 105°C and weighed again (Blake & Hartge, 1986). Using a gas pycnometer requires a sample chamber and a reservoir where a change of pressure is made to determine the volume (Danielson & Sutherland, 1986), thus allowing the determination of the particle density (after measuring the mass of the sample).

The water content can be determined most of the time by removing the water from the sample, as detailed by Gardner (1986), with direct and indirect methods. In the field, it can be measured

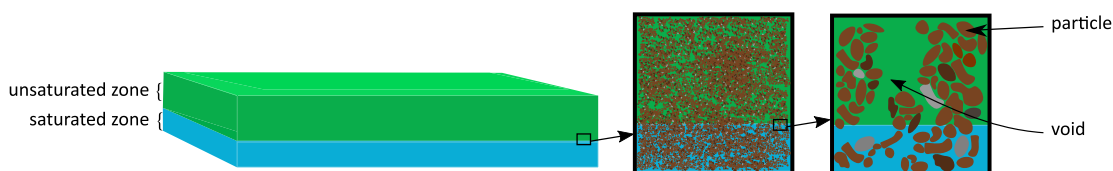
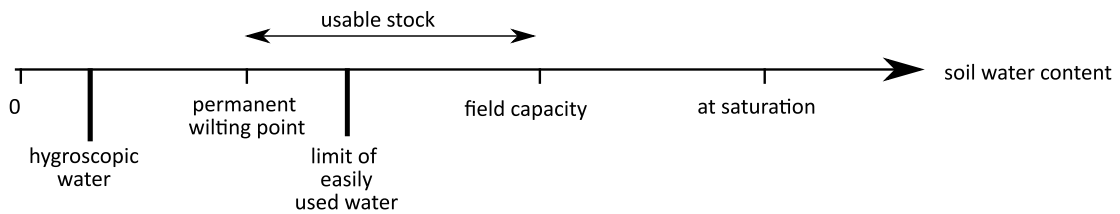


Figure 5.1 Scheme of soil texture and structure.

**Table 5.1** Key soil parameters with the fluid volume  $V_f$ , the total volume  $V_t$ , the water volume  $V_w$ , the air volume  $V_a$  and the solid volume  $V_s$ , the dry bulk density  $\rho_b$ , the particle density  $\rho_p$ , the water mass  $M_w$ , the solid mass  $M_s$ , the water density  $\rho_w$ , the relative water content  $\theta_r$  and the water content at saturation  $\theta_s$ .

| Parameter            | Porosity ( $L^3/L^3$ )  | Mass Water Content ( $M^3/M^3$ )   | Volumetric Water Content ( $L^3/L^3$ )                 | Effective Saturation (No Dimension)                   |
|----------------------|---|--|--|---|
| Calculation          | $\varphi = \frac{V_f}{V_t} = \frac{V_w + V_a}{V_w + V_a + V_s}$ $= 1 - \frac{\rho_b}{\rho_p}$ | $w = \frac{M_w}{M_s}$  | $\theta = \frac{V_w}{V_s}$ $= \frac{\rho_b}{\rho_w} w$ | $S_e = \frac{\theta - \theta_r}{\theta_s - \theta_r}$ |
| Determination method | Total porosity with particle and bulk densities or gas pycnometer                             | Direct method: gravimetry, drying<br>Indirect method: electrical conductivity, capacitance, neutrons probes... | Linked to the mass water content                       | Linked to the volumetric water content                |



**Figure 5.2** Key values of water content in soils linked to the capacity for vegetation to access it.

by a neutron probe (Bell, 1976) and other capacitance probe techniques (Robinson & Dean, 1993) like time-domain reflectometry (Whalley, 1993). The soil-water content is, for example, used to characterize the soil’s ability to support vegetation growth (Cassel & Nielsen, 1986): between two values of water content (i.e., corresponding to the field capacity and the permanent wilting point of the soil), the vegetation can access the water they need (Figure 5.2). In hydrology studies, when soil is naturally saturated, the volumetric soil water content is called ‘at saturation’ and is written as  $\theta_s$ . Thus,  $\theta_s$  is the maximum water content value reached for a given soil under natural conditions.

The soil composition tends to be highly heterogeneous with different lithofacies (material). Sedimentological studies aim to characterize the geological and sedimentological features of soils, that is, the lithofacies and their arrangement in soil (Goutaland *et al.*, 2007). The groundwater table is defined by the elevation of the saturated zone where the volumetric water content is equal to the maximum value  $\theta_s$ . If this value is not reached, the water content is lower than  $\theta_s$  and the soil is unsaturated. The unsaturated zone of soil composing the first metres is also called the vadose zone (Figure 5.1). With respect to the role of soils in UD the prime focus is on the unsaturated parts of the soil.

### 5.2.3 Hydraulic properties of soils

Another important soil parameter, the water pressure head,  $h$  [L], is used to characterize the energy status of water into the soil and represents the capillary pressure head. As water moves slowly in soils, the kinetic energy is assumed negligible and the hydraulic head  $H$  [L] is then the sum of the pressure head (i.e., capillary pressure head), the elevation and the osmotic force. For a soil in osmotic

equilibrium (i.e., with the same concentrations or equivalently similar quality of interstitial water), the total hydraulic head is given by:

$$H = h + z \quad (5.1)$$

where  $z$  [L] is the elevation and  $h$  [L] is the capillary pressure head. In the unsaturated zone, the pressure head  $h$  is negative, and its absolute value is called the water suction. Water flow is due to the gradient of the total hydraulic head  $H$  and the movement of water goes from high to low hydraulic heads (Angulo-Jaramillo *et al.*, 2016; Bruand & Coquet, 2005: *Les sols et le cycle de l'eau*; Hillel, 1998).

The capillary pressure head at standard temperature (20°C) and pressure conditions can be estimated for a vertical cylinder of radius  $r$  with the Jurin–Laplace law at standard conditions for temperature and pressure as

$$h = \frac{2\sigma \cos(\theta)}{r\rho g} \sim \frac{1.49}{r} \quad (5.2)$$

where both  $h$  and  $r$  are expressed in cm, with  $h$  corresponding to the height of liquid in the cylinder above a free water reference level,  $\sigma$  is the surface tension,  $\theta$  is the contact angle between the water and the cylinder wall,  $\rho$  is the mass density and  $g$  is the gravitational acceleration. Note that the pressure head is inversely proportional to the cylinder radius (Equation (5.2)). Thus, if we consider soil porosity as a set of cylinders of different diameters, the finer the pore diameter, the lower the pressure head needed to activate (i.e., saturate) the pore. In other words, when the soil dries, the larger pores empty before the smaller ones.

A water retention curve defines, at soil–capillary water equilibrium, the relationship between the volumetric water content  $\theta$  and the absolute value of the pressure head  $|h|$ . The S-shape of the curve depends strongly on both the texture and the structure of the soil (Figure 5.3a, b). Clays retain more water than sand and desaturate less easily. A less compacted soil for the same soil texture can have a higher water content at saturation, because of a higher porosity. Moreover, a phenomenon of hysteresis exists and changes the shape of the retention curve, as water is better retained by drying than by wetting soil (Figure 5.3c). Historically, Buckingham (1907) was the first to establish retention curves based on laboratory experiments on different textures of soils.

Van Genuchten (1980) developed the following analytical model for water retention curves:

$$\frac{\theta - \theta_r}{\theta_s - \theta_r} = \left(1 + |\alpha h|^n\right)^{-m} \quad (5.3)$$

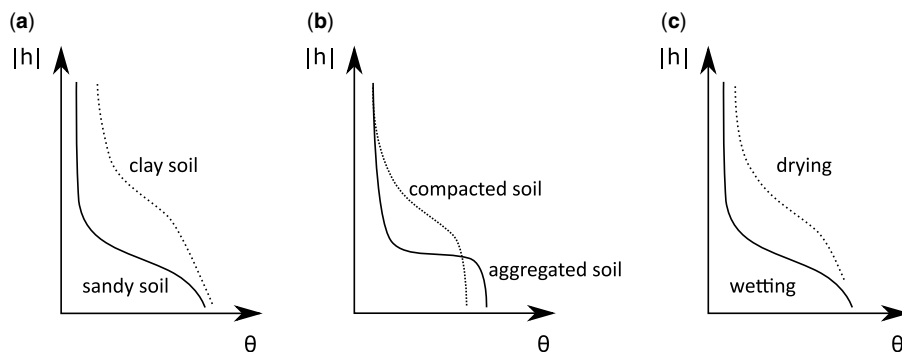


Figure 5.3 Influence of (a) texture and (b) structure on the water retention curve. (After Angulo-Jaramillo *et al.*, 2016).

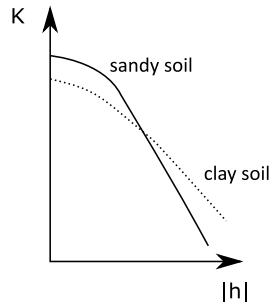


Figure 5.4 Water hydraulic conductivity curve.

with  $\theta_r$  is the residual volumetric water content (at negative infinite pressure head, smaller or equal to the wilting point),  $\theta_s$  is the saturated volumetric water content,  $\alpha$  is an empiric parameter (per  $L$ ) also called scale parameter for water pressure head and  $n$  and  $m$  is the shape parameters of the curve.

The hydraulic conductivity,  $K$  ( $L/T$ ) describes the ability of a fluid to move through pores. The hydraulic conductivity is calculated as the ratio of water flow to hydraulic gradient. It is a function of the pressure head and has the same dimension as a velocity ( $L/T$ ). This parameter highly depends on the water content in the soil, and the hydraulic conductivity at saturation  $K_s$ , as an intrinsic parameter of soils. The water hydraulic conductivity curve represents the link between the hydraulic conductivity and the pressure head or water content (Figure 5.4). Indeed, when the soil is unsaturated, only part of the pores is activated and conducts water, resulting in a lower hydraulic conductivity. Conversely, at saturation, all pores are activated and the hydraulic conductivity increases.

The Darcy equation (see e.g., Hillel, 1998) represents steady water flow conditions in a vertical soil column, with  $z$  in an upward direction, under uniform and saturated soil conditions:

$$q = -K_s \frac{\partial H}{\partial z} \quad (5.4)$$

with  $q$  is the flux [ $L/T$ ],  $K_s$  is the hydraulic conductivity at saturation and  $\partial H/\partial z$  is the vertical hydraulic gradient. The minus sign means that water always moves from high to low values of total hydraulic head.

Under unsaturated conditions, the hydraulic conductivity depends on pressure head (or the water content), and Darcy's law can be generalized as

$$q = -K(h) * \frac{\partial H}{\partial z} = -K(h) * \left( \frac{\partial h}{\partial z} + 1 \right) \quad (5.5)$$

Alternatively,  $K(h)$  may be written as a function of the water content,  $K(\theta)$ . This last relationship is preferred since hysteresis affects the function  $K(\theta)$  less than  $K(h)$ . For one-dimensional vertical flow, the combination of the continuity equation (Eq. 5.6) with the generalized Darcy's law (Equation (5.5)) gives the Richards equation that governs the flow of water in soils (Equation (5.7)).

$$\frac{\partial \theta}{\partial t} = - \frac{\partial q}{\partial z} \quad (5.6)$$

$$\frac{\partial \theta}{\partial t} = - \frac{\partial}{\partial z} \left( -K(h) * \left( \frac{dh}{dz} + 1 \right) \right) \quad (5.7)$$

The Richards equation is valid for non-deformable soils (e.g., non-swelling and shrinking soils), under isothermal conditions, and ignores the interaction with the air flow in the soil pores, when water pushes the air away. For more details on the Richards equation refer to [Angulo-Jaramillo \*et al.\* \(2016\)](#). The solution of the Richards equation consists of calculating the changes in  $h$  and  $\theta$  in both space and time using the hydraulic characteristic curves  $h(\theta)$  and  $K(\theta)$  of the soil and the initial and boundary conditions.

The pair of characteristic curves  $h(\theta)$  and  $K(\theta)$  (or  $h(\theta)$  and  $K(h)$ ) fixes the hydrodynamic identity of an unsaturated soil. Their estimation is one of the challenges in hydrology and hydrogeology. Different in situ experimental tests are used to estimate the parameters of the relationships ([Equation \(5.7\)](#)) from the analysis of the measured infiltration flux (see paragraph 5.2.5).

#### 5.2.4 Infiltration component of the water cycle

Infiltration concerns the physical process of water entry into the soil from the soil surface. The infiltration flux or Darcy's velocity corresponds to the flow rate entering the soil divided by the infiltration surface:

$$i(t) = \frac{Q(t)}{S} \quad (5.8)$$

Cumulated infiltration  $I$  (L) is the integral over time of the infiltration flux ([Equation \(5.9\)](#)), which implicitly corresponds to the total volume of infiltrated water divided by the soil surface. It has the same unit as rainfall amount, that is, the unit of length.

$$I(t) = \int_{t=t_0}^t i(t) dt \quad (5.9)$$

Water infiltrates first through the surface pores and moves vertically or horizontally because of gravitational or suction forces, thus replacing the air in the pores. When an amount of water is applied at the surface, a wetting front develops in the soil profile which moves downward. The soil between the surface and the wetting front is wetted at a water content that is in equilibrium with the water pressure head applied at the surface (assuming this remains constant over time).

The three variables detailed above,  $\theta$ ,  $h$  and  $K_s$ , characterize infiltration of water into the soil and the redistribution of this water after an infiltration (or rainfall or irrigation event). Infiltration thus depends on the capacity of the soil to let water move (i.e., as a function of its texture and structure) and on the changes in the energetic state between the surface, the groundwater and the unsaturated parts ([Bruand & Coquet, 2005](#)). The speed of infiltration depends also on the initial soil water. Other parameters not considered in the above equations and models include physical soil properties, particle dispersion, air retention, temperature and the presence of dissolved gases or salts in the water, and so on ([Chossat, 2005](#)).

For regular cases, where the infiltration of water is governed by capillary forces and gravity, allowing for the application of Richards' equations, the cumulative infiltration curve,  $I(t)$ , increases with an initial convex shape followed by an asymptote with a constant slope, illustrating the attainment of steady state conditions when water infiltrates mostly by gravity. Different equations exist to represent cumulative infiltration at the soil surface. Some are empirical, directly related to the soil in question studied (e.g. [Horton, 1941](#)), while others reflect the physics of the infiltration and movement of water in soils (e.g. [Green and Ampt, 1911](#)). However, many of these equations consider the soil as homogeneous, with a single porosity and hydraulic conductivity, and overlook the complexity and heterogeneity of the soil structure and texture. As water infiltrates mainly by capillary forces and gravity ([Angulo-Jaramillo \*et al.\*, 2016](#)), [Philip \(1957\)](#) was first to account for both the vertical and the horizontal infiltration components, introducing sorptivity as a '*measure of the capillary uptake or removal of water*'. Sorptivity is a crucial parameter with regards to the modelling of water infiltration into soils ([Angulo-Jaramillo \*et al.\*, 2016](#)).



## 5.2.5 *In situ* measurements and soil hydraulic characterization

### 5.2.5.1 *Field methods*

To determine the cumulative infiltration of water into soils in the field, the main concept consists of applying a known volume of water and recording the time needed for its complete infiltration. Two types of experimental methods exist. The first one, the unsaturated method, applies a negative pressure head on the soil surface, activating only the thinnest pores of the soil matrix. The wetting bulb created under the surface during the experiment is unsaturated and involves mostly the soil matrix. The second one, the saturated method, applies a null or positive pressure head on the soil, activating all pores, even the macropores. For both methods, the infiltrated volume is recorded as a function of time. The pressure boundary condition applied at the surface can be constant or variable over time.

The infiltration can take from a few minutes to several hours, depending on the volume injected, the initial soil condition or the intrinsic hydraulic properties of the soil. The spatial scale is also an important parameter to consider in determining the hydraulic parameters of the soil (Glaser *et al.*, 2019). Presented in this section are some field methods for both saturated and unsaturated soil conditions. In the field, most devices allow one to determine the infiltration rate  $i(t)$  ( $L/T$ ) and the cumulative infiltration  $I(t)$  ( $L$ ) [Equations (5.8) and (5.9), respectively]. The hydraulic properties of the soil are then estimated by the analysis of the measured  $i(t)$  or  $I(t)$  curves and fitting them to infiltration models.

One of the most used methods in civil engineering is called the Porchet essay (or 'percolation rate'). It consists of a hole filled with water until steady state conditions are supposed to have been reached. Then, a known volume of water is poured into the hole, and the infiltration over time is recorded. With Darcy's equation and the hypothesis of a uniform vertical hydraulic gradient, the hydraulic conductivity can be calculated. This method is easy and cheap but requires huge amounts of water and time. Moreover, it assumes both steady-state and one-dimensional flow conditions. Nevertheless, it is widespread and has been used for a long period of time for measuring infiltration fluxes between 0 and 10 m/day (Chossat, 2005).

Table 5.2 shows a brief overview of the main methods used in the field for the determination of the hydraulic parameters of unsaturated soils. In his book Chossat (2005) presented a table comparing the various devices found in the literature. Deb and Shukla (2012) also wrote a review of some devices.

### 5.2.5.2 *Modelling water infiltration to estimate soil hydraulic parameters*

The BEST (Beerkan Estimation of Soil Transfer parameters) protocol is one example of the various methods developed to determine water retention and hydraulic conductivity curves (Angulo-Jaramillo *et al.*, 2016). The BEST method combines the van Genuchten (1980) equation with the conditions of Burdine (1953) ( $m = 1 - 2/n$  in Eq. 5-3) in describing the water retention curve,  $K(\theta)$ , and with the Brooks and Corey (1964) equation in describing the unsaturated hydraulic conductivity,  $K(\theta)$ . The method uses a single ring infiltration experiment (i.e., a Beerkan test) to measure the infiltration curve and combines the data with additional field measurements including the particle size distribution, soil dry bulk density, and the initial and final water contents. The particle size distribution is modelled analytically to estimate the shape parameters of the water retention and hydraulic conductivity curves  $h(\theta)$ . The cumulative infiltration curve is then fitted to analytical models to derive the hydraulic conductivity and the sorptivity. The BEST method is one example of an analytical inversion method for water infiltration. Three BEST methods can be considered, BEST-Slope, -Intercept and -Steady, which are all based on the same principle. They only differ on how the analytical infiltration model is adjusted to the experimental cumulative infiltration data. The three BEST methods have been coded in Scilab (<https://www.scilab.org/>) with an easy-to-use graphic interface. All codes are open-source and can be found on the BEST website (<https://bestsoilhydro.net/>)

Šimůnek *et al.* (2008, 2016) developed a commercially available software package called HYDRUS that models the transport of heat, water, and solutes in a 1-D, 2-D or 3-D variably saturated medium. The Richards' equation for variably saturated water flow and advection-dispersion type



Table 5.2 Main field devices with their characterization.

| Name                 | Principle   | Tools/Device   | Hydraulic Conductivity Range, Soil Type and Experimental Period                              | Advantages  | Disadvantages   | References   |
|----------------------|---|--|--|---|---|--|
| Surface infiltration | Infiltration at constant negative pressure head   | Mariotte tower and water reservoir above a porous plate, from a few to a dozen cm<br>Commercialized and possibly automatized                       | 10 <sup>-4</sup> -10 <sup>-7</sup> m/s (minidisc infiltrometer) sand and silt approx. 30 min | Easy to use in the field more relevant results for near-saturated conditions one experimenter is enough tested and validated for different soil types and climates                                | Not representative of macropores can be perturbed by the sand layer which is added to improve conductivity  | Angulo-Jaramillo <i>et al.</i> (2016); Ankeny <i>et al.</i> (1988); Castiglione <i>et al.</i> (2005); Chossat (2005) |
| Single ring          | Infiltration at null or low pressure head in the ring (variable charge) or in a reservoir (constant charge) | A ring from 5 to 70 cm of diameter and 10-30 cm of height in general in inox with or without reservoirs<br>Commercialized and possibly automatized | All soils<br>30 min to a few hours   | Easy to use in the field precise result for the hydraulic conductivity at saturation one experimenter is enough tested and validated for different soil types and climates for all types of pores | Tends to overestimate hydraulic conductivity at saturation can compact the soil can create preferential flows along the edges of the ring water can also put particles in suspension, which can clog the soil | Bouarafa <i>et al.</i> (2019); Chossat (2005); Jačka <i>et al.</i> (2014); Zhao <i>et al.</i> (2020a, 2020b)         |

(Continued)

Table 5.2 Main field devices with their characterization (Continued).

| Name                     | Principle  | Tools/Device   | Hydraulic Conductivity Range, Soil Type and Experimental Period | Advantages   | Disadvantages   | References  |
|--------------------------|--|--|---|--|---|---|
| Double ring              | Infiltration at null or low pressure head considers the flow in the inner ring as 1D | Two concentric rings, one small in the centre (10–30 cm) and a biggest around (50–60 cm)<br>Commercialized | $10^{-4}$ – $10^{-8}$ m/s<br>30 min to a few hours              | Is supposed to be more precise and surface evaporation is limited<br>tested and validated for different soil types and climates                              | Can compact the soil<br>can create preferential flows along the edges of the ring<br>water can also put particles in suspension, which can clog the soil<br>limited representativeness of soil pores<br>heterogeneities | Chossat (2005); Gregory <i>et al.</i> (2005)  |
| Borehole infiltration    | Infiltration in a borehole constant pressure head                                    | Tube of a few cm of diameter and high height (until 2 m)<br>Commercialized                                 | $10^{-4}$ – $10^{-7}$ m/s<br>all soils approx. 1 hour           | Tested and validated for different soil types and climates<br>for all types of pores   | Can destruct and compact the soil<br>overestimates horizontal flows compared with vertical ones<br>water can also put particles in suspension, which can clog the soil  | Bosch and West (1998); Chossat (2005); Kodešová <i>et al.</i> (2010); Reynolds and Lewis (2012) |
| Philip-Dunne permeameter | Infiltration in a borehole at falling pressure head                                  | Flat hole with a few cm diameter   | $10^{-4}$ – $10^{-6}$ m/s<br>Silt loam, Sandy loam and sand     | Simple measure of the hydraulic conductivity at saturation for soils with a small permeability<br>tested and validated for different soil types and climates | Tube's installation can be complicated and allow for leaks to occur, similar to the Guelph permeameter<br>water can also put particles in suspension, which can clog the soil   | Alakayleh <i>et al.</i> (2019); Chossat (2005)  |

equations for heat and solute transport are numerically solved by HYDRUS. The flow equation can also account for dual-permeability or dual-porosity type flow. This software has been intensively used for the context of infiltration and solutes transfer modelling, with various add-on modules that expand its capabilities (Šimůnek *et al.*, 2016; Yilmaz *et al.*, 2013).

## 5.2.6 Addressing the complexity of processes

### 5.2.6.1 Pore characterization

The models and equations presented above are almost all based on Richards' equation and do not consider the heterogeneity of soils found in the field, according to Beven and Germann (1982). Thus, in the years after the publication of their paper, different equations were developed to represent macropores and preferential flows more precisely. As soils in the field are *never* homogeneous, they typically present pores of different sizes. The variety of pores may change the ability of the soils to move water as a function of associated water repellence, cracks and clogging.

Different types of pores are often distinguished: (I) the micropores, which arise from the inhomogeneous packing of the particles and which are responsible for governing water and solutes retention; (ii) the macropores, which are larger and are mainly created by roots, animal galleries and fractures; and finally, (iii) the mesopores, which are an intermediate class between the two previous classes. The Soil Science Society of America (<https://www.soils.org/publications/soils-glossary>) classifies the pore sizes as: micropores between 5 and 30  $\mu\text{m}$ , mesopores between 30 and 75  $\mu\text{m}$ , very fine to fine macropores between 75 and 2000  $\mu\text{m}$ , and medium and coarse macropores above 2000  $\mu\text{m}$ . The differences between the pore sizes are important for the representativeness of infiltration models. The presence of macropores tends to create preferential dual-porosity flows characterized by physical non-equilibrium (Beven & Germann, 2013).

Some soils are called water-repellent when infiltration is diminished or even prevented by a barrier that restricts the rate and amount of water absorption under dry conditions. The capillary rise in a very water-repellent soil will be zero, preventing soil particles from moistening, resulting in water droplets forming on the soil's surface which will frequently evaporate before being able to penetrate into the soil (Hallett, 2008). Water repellence can stem from an organic layer at the surface, which becomes hydrophobic when the soil is dry. The most used technique to determine water repellence is the water drop penetration time (WDPT) test, which measures how long it takes for a water drop to infiltrate. The presence of water repellent soils completely changes infiltration curves (Wang *et al.*, 2000).

Some clay soils can crack while drying, because of soil suction and soil mechanical properties, creating large voids (Morris *et al.*, 1992), which modify water infiltration (Cheng *et al.*, 2021). In arid and semi-arid areas, some clay soils can also shrink and swell which has an impact on the soil structure. As soil deformation is not reversible in all cases, it can introduce cracks and changes in porosity (Medjnoun & Bahar, 2016). Finally, clogging, which is characterized by a decrease in the soil's accessible pore volume, may also modify infiltration in soils (Jeong *et al.*, 2018). The processes mentioned above, and many others that reflect the complexity of the soil systems, favour the establishment of preferential flows.

### 5.2.6.2 Spatio-temporal variability

Even though the soil variability has the biggest impact on infiltration (Childs *et al.*, 1993), the spatial and temporal (i.e., reflecting both seasonal and weather impacts) scales should be identified and considered as they can influence the hydraulic parameters (Green *et al.*, 2003; Nielsen *et al.*, 1973). Infiltration depends on the spatial variability observed at all scales, from the micro-scale (i.e., mm) to the field scale (Gerke *et al.*, 2010; Hallett *et al.*, 2004; Haws *et al.*, 2004). The methods mentioned earlier give an estimation of the infiltration at a point scale, which could be different at other scales because of the slope of the land or soil heterogeneities. The conversion from small scale to larger scale parameters is still a subject of studies (Koppe *et al.*, 2022). Nevertheless, some methods have been developed to study infiltration directly at larger scales by multiplying the number of samples or tests

(Concialdi *et al.*, 2020; Zhao *et al.*, 2020b), by using non-invasive methods (Di Prima *et al.*, 2015; Gerke *et al.*, 2010), or by increasing the size of the device or the footprint of the experiment.

The parameters can also vary on a temporal scale between different seasons and even during one season. The infiltration pattern, the soil porosity and the main hydraulic parameters can change, mainly because of the evolving state of the soil (e.g., reflecting compaction, different activated zones over time, wetting and drying and so on, Childs *et al.*, 1993; Mubarak *et al.*, 2009). This seasonality may modify the runoff coefficient (Cerdà, 1996) and hydraulic parameters such as the infiltration rate (Cerdà, 1997). Moreover, the occurrence of several freeze-thaw cycles during the winter months can severely reduce the infiltration rate (Zaout *et al.*, 2022).

### 5.2.6.3 Preferential flow quantification

To quantify preferential flow, Allaire *et al.* (2009) reviewed the techniques used in laboratories and in the field to investigate the soil–structure dynamics. The authors suggested that complementary measurements to infiltration should be performed to obtain additional information on both soil heterogeneity and water flow: imagery scanning, resin impregnation, skeletization, photos and excavation, smoke injection, geophysical devices (ground penetrating radar (GPR), electrical resistivity tomography (ERT) and electromagnetic induction (EMI), see below), ring and tension infiltrometers under varying pressure heads, tracers and dyes, through breakthrough curves of solutes and particles.

Tracers such as salts and dyes like Brilliant Blue FCF or rhodamine are widely used to investigate macropore flow and interactions between macropores and the soil–matrix (Anderson *et al.*, 2009a, 2009b; Kodešová *et al.*, 2010; Nimmo *et al.*, 2009; van Schaik *et al.*, 2010). The tracers and dyes are usually used with one of the infiltration devices presented above. After an infiltration measurement with dyes, soils need to be excavated. For monitoring the tracers' pathways in the soil under the infiltration device, it is necessary to couple the infiltrometer with a non-invasive device capable of detecting the tracers. A difference of electrical conductivity with salts can be determined, for example.

Non or slightly invasive studies of infiltration at various scales of time and space have found value in geophysical approaches to introduce new information about water infiltration processes. Some geophysical methods using surface electrical resistivity measurements (i.e., ERT), changes in the apparent electrical conductivity (like EMI) or pulses of radar (like GPR) can image subsurface structures and thus can be used to monitor water infiltration into soils. They allow a broad view of flow pathways, at different and large scales, are non-destructive, are repeatable and can connect the dynamics of infiltration to underground structures (Fan *et al.*, 2020). A comparison of the three devices may be found in the review by Fan *et al.* (2020).

ERT is made up of four electrodes to reduce the impact of contact resistance at the interface between the electrode and the soil pore water (Daily *et al.*, 2005). Two electrodes are subjected to a known current, and the potential difference between the other two electrodes is measured. Daily *et al.* (1992) were the first to use ERT in the field to follow water movement in the unsaturated zone. They made two kinds of infiltration experiments and used the finite element method (FEM) with a  $7 \times 14$  mesh to model the reconstruction plane. The resistivity differences give an appreciation of the water mobility. More recently, ERT was used in a karst vadose zone (Watlet *et al.*, 2018). The methods for data gathering, storage, filtering, inversion and visualization were semi-automated, and data were time-lapse inverted to visualize resistivity variations.

EMI uses the fact that the physical and chemical characteristics as well as the morphology of soils are directly impacted by the depth and movement of water through the subsurface (Doolittle & Brevik, 2014). The EMI device is made of two sensors: one transmitter and one receiver. The fundamental electromagnetic field that they transmit causes electrical currents induced in the soil, and the sensor's receiver detects the secondary electromagnetic field produced by these currents. The latter is used to determine the 'apparent' or 'bulk' electrical conductivity (ECa) for the volume of soil profiled in circumstances referred to as 'operating under low induction numbers'. The EC changes as a function of the soil parameters, temperature and concentrations of ions in solution.

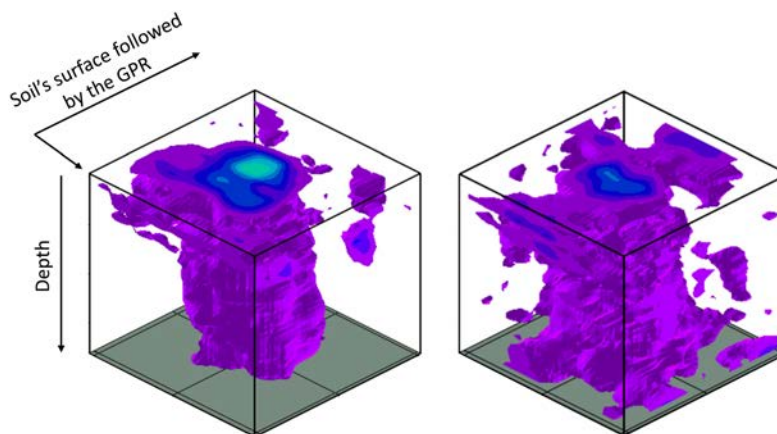


**Figure 5.5** Two examples of GPR visualization in 3D of water infiltration and preferential flow pathways.

GPR consists of two antennas, one emitter and one receptor, and is linked to an acquisition system for data storage and visualization (Utsi, 2017). The emitter generates electromagnetic waves through the soil. If the pulse meets a change in the nature of the materials, (textures and structure) or in the hydric conditions, based on electromagnetic properties, the signal is returned to the receptor antenna. GPR is also used to characterize preferential flow paths (Guo *et al.*, 2014). Different methods for data treatment exist, specifically developed to track water in soils (Allroggen & Tronicke, 2015; Di Prima *et al.*, 2020). For example, Figure 5.5 illustrates, in three dimensional, the preferential flow pathways obtained from a single ring infiltration experiment.

### 5.2.7 Modelling of preferential flow

Šimůnek *et al.* (2003) presented a review of models depicting preferential and non-equilibrium flows in the vadose zone. The two main model types are based on double porosity or permeability approaches. Dual-permeability and dual-porosity models both presuppose that the porous medium is composed of two zones that interact, one involving the inter-aggregate porosity, macropores or fractures, referred to as the fast-flow matrix, and the other made up of micropores inside the soil aggregates or the rock matrix, referred to as the soil matrix. Dual-permeability approaches consider water flows in both the fast-flow and the matrix regions while water stays stagnant in the matrix region for the dual-porosity approach. Similar in principle, multi-porosity and/or multi-permeability models also contain additional interacting pore zones.

The BEST method is not always valid, as shown by Angulo-Jaramillo *et al.* (2019): water repellent soils can show a negative intercept and are not well represented; the infiltration rate of some very fine soils can be over-estimated; the intercept of very coarse soils are not consistently estimated; soils with macropores are only represented with the BEST-steady method while the estimated hydrodynamics parameters of sealed soils are not representative.

A BEST method was developed to tackle the challenges associated with the presence of macropores (Lassabatere *et al.*, 2019). The principle is the same, but the equations are repeated, differentiating between the parameters for two regions, the matrix and macropores. Thus, the bulk and local volumetric water content, the bulk and local hydraulic conductivities and the volume occupied by both regions have different values. Additional research is being conducted to adapt the BEST methods to water-repellent soils (Prima *et al.*, 2021; Yilmaz *et al.*, 2022).

### 5.2.8 Concluding remarks on infiltration processes

UD systems (Fletcher *et al.*, 2015) include heterogeneous and living soils that evolve over time. Cracks, roots and animal galleries can appear (Bedell *et al.*, 2021, 2013; Fernandes *et al.*, 2022; Saulais *et al.*, 2011), facilitating water infiltration. However, infiltration systems have shown a general decrease of their infiltration capacities over time (Al-Rubaei *et al.*, 2015), mainly caused by clogging (Le Coustumer *et al.*, 2009). The complexity of the soil heterogeneity and its evolution over time, coupled with the impact of environmental and physical processes, is still a challenging research topic.

To better design and manage infiltration facilities, the determination of the hydrodynamic parameters and the water movement models should be more precise and monitored. Regular monitoring and maintenance could help retain high infiltration capacities for these systems (Al-Rubaei *et al.*, 2015; Bouarafa *et al.*, 2019).

For field measurements, the combination of experimental devices, with the use of geophysical measurements and/or automated devices appears promising. For example, some automated single ring infiltrometers were developed, facilitating the data acquisition and allowing several experiments at the same time (Di Prima *et al.*, 2015) which can be used with the BEST methods to evaluate the risk of disfunctioning UD systems (Bouarafa *et al.*, 2019). The use of GPR proved very efficient for the characterization of infiltration bulbs and the understanding of processes in the vadose zone, allowing for the determination of the main preferential flow pathways in a non-destructive way (Di Prima *et al.*, 2023, 2020).

## 5.3 CLOGGING

### 5.3.1 Introduction

As the decrease of the permeability/infiltration rate (in natural soils and in NBS) over time is inevitable and has been observed at both centralized systems (e.g., Dechesne *et al.*, 2005; Gonzalez-Merchan *et al.*, 2012; Hunt *et al.*, 2011; Le Coustumer & Barraud, 2007; Marsalek *et al.*, 2006) and source control facilities (e.g. Barraud *et al.*, 2014; Bergman *et al.*, 2011; Blecken *et al.*, 2017; Emerson *et al.*, 2010; Le Coustumer *et al.*, 2009; Winston *et al.*, 2016; Yang *et al.*, 2022 and so many others) such as bioretention facilities, swales, trenches or porous pavements, it is important to understand

- the way it develops,
- its spatial distribution (i.e., where does clogging occur first or most?),
- the temporal dynamics (i.e., how long does it take for a device to get clogged?), or
- when should maintenance procedure reasonably be triggered?

and the predominant factors to limit or prevent it.

The large diversity of devices, configurations, substrates and environments constitutes a real challenge in addressing the issue of clogging. The scales at which infiltration occurs and the pressure exerted on facilities directly influence the spatial and temporal distribution of clogging. For example, there could be a big difference between centralized structures (e.g., infiltration basins collecting stormwater from a large catchment with large sediment inputs) and source control facilities such as swales, bioretention systems, trenches and permeable pavements draining much smaller areas. But, even for the same type of facility there will be significant variability, for example, hydraulic loading ratios, composition, the presence or absence of pre-treatment provisions, splash pads, overflows, implementation in different contexts, and so on.

For all kinds of systems, the decrease in permeability can be classified into three types. It can be:

- physical/mechanical (which tends to be the most important one) due to:
  - the input of suspended solids brought by the stormwater from the tributary catchments,
  - natural compaction or compaction resulting from human activities when the facilities are accessible to the public, or
  - internal erosion (e.g., erosion of the sides of a swale clogging its bottom).



- biological due to the development of micro-organisms (e.g., algae, fungi, bacteria and protozoa) that form biofilms on the surface. This has been observed at large infiltration basins with a bare bottom at the onset of the clogging subjected to hot weather conditions ([Gonzalez-Merchan et al., 2012](#)). The use of vegetation or coarse gravels in the top layer generally eliminates this type of clogging.
- chemical: involving the precipitation and dissolution of minerals within the infiltrating substratum which can be accompanied by the development of bacteria reducing the porosity of the medium. As this clogging is closely linked to the previous ones, it is difficult to study it in isolation. However, it is minor compared to physical and biological clogging.

Clogging tends therefore to be the result of excessive deposition of debris and sediment (especially fine particles transported by runoff) or excessive inputs of organic matter ([Gonzalez-Merchan et al., 2012](#)). This accumulation of material can be due to a variety of site-specific factors, often occurring in tandem, including:

- poorly specified infiltration media (e.g., undersized infiltration systems, low initial hydraulic conductivity, media composed of too fine materials ([Beryani et al., 2021](#); [Le Coustumer et al., 2009](#)),
- a high hydraulic loading ratio (i.e., volumetric loading) for the size of the system, here (as done often) roughly estimated by the area of infiltration system divided by the size of the contributing catchment area,
- significant erosion of material or wash-off of deposits from the catchment, especially in the presence of construction sites with inadequate erosion and sediment control provisions which lead to high inputs of construction sediments ([Azzout et al., 1994](#); [Barraud et al., 2014](#); [Silva et al., 2010](#)),
- compaction (i.e., the re-arrangement and settling of the infiltration medium due to the weight of water or to the action of users ([Beryani, et al., 2021](#); [Blecken et al., 2017](#)),
- lack of maintenance.
- normal ageing process.

### 5.3.2 Approaches to determine the evolution of permeability

To assess the spatial distribution and temporal evolution of clogging, the general approach consists of defining one (or several) indicator(s), to evaluate or measure the performance and then compare the progression in the recorded values over time or against different parts of the facility of interest. Various approaches can be found in the literature as a function of the original intent, type and scale of the infiltration systems.

The most widely used indicator is the hydraulic conductivity (most often conducted for full saturation conditions to eliminate the variability of the media water content and preferably standardized using a specific temperature [e.g., 20°C] to get comparable results from one date to another). As explained in Chapter 4, the method consists of measuring the drop in water level in rings sunk in the media (e.g., calibrated simple ring infiltrometers or home-made devices [e.g., used by [Beryani et al., 2021](#); [Angulo-Jaramillo et al., 2016](#); [Le Coustumer et al., 2009](#); [Gonzalez-Merchan et al., 2014](#)], or double ring infiltrometers [e.g., [Al-Rubaei et al., 2015](#); [Kluge et al., 2018](#)]). This approach of measuring the hydraulic conductivity yields localized results and must therefore be repeated across the entire surface of the facility to provide an overview of the spatial distribution.

The method suits well and is easy to perform for small source control facilities with a rather flat bottom (e.g., swales, bioretention systems and rain gardens). Moreover, it requires few testing points because of the size of the facility. [Beryani et al. \(2021\)](#) noticed in a Swedish study on 36 biofilters less than 6 years old (and with footprints ranging from 8 to 700 m<sup>2</sup> accommodating runoff from catchments between 230 and 15,000 m<sup>2</sup>) that there was no significant difference between the three tested locations used (i.e., near the inlet, outlet and middle point along the flow path). The experience



of others was different in that order of magnitude differences were observed which is particularly problematic when such tests are conducted in conjunction with inspections at the time of project acceptance before it is turned over to the future owner. A large number of tests would then need to be conducted for the findings to be statistically significant (Erickson *et al.*, 2013). For that reason, flood tests with water supplied by either a hydrant or water truck have been conducted as illustrated in Section 9.5.2.

For systems with a large footprint (e.g., infiltration basin) approaches using the above hydraulic conductivity testing methods are not well suited to generate a good appreciation of the global hydraulic performance of the entire unit given its expected spatial heterogeneity being much higher. Thus, an alternate procedure should be applied which, incidentally, can also be used for smaller source control facilities. The aim is to evaluate the global hydraulic resistance by measuring the inflows, outflows (when an overflow is implemented) and water depths in the system during different events of a similar nature (e.g., events generating a water depth of more than 50 cm in an infiltration basin, or a few cm in an infiltration trench). The hydraulic resistance may be obtained by its calibration in, for instance, Bouwer's model with the data acquired (Bouwer, 2002). This method was applied many times including Gautier, 1998; Dechesne *et al.*, 2005; Le Coustumer *et al.*, 2007; Gonzalez-Merchan *et al.*, 2012 for infiltration basins and Proton, 2008; Barraud *et al.*, 2014; Emerson *et al.*, 2010 for swales or trenches. This method not only generates an appreciation of the global extent of clogging but also allows one to differentiate between the bottom and the sides of a facility. To be applied, the clogging process should have commenced with water visibly ponding. While this method has proven to be quite useful for research purposes and an overall understanding of the dynamic nature of clogging, it is rather difficult to carry out it for practical purposes due to the extensive data and relatively sophisticated monitoring needs.

Other global indicators may be used to get an appreciation of the drawdown or emptying time (e.g., the time taken for the maximum height of water in a facility to be completely drained out after a rainfall event) which has expectations or limits expressed in many design guidance documents or standards. For instance, Beryani *et al.* (2021) reported that most municipalities have a limit of 48 hours for biofilters, with some using shorter durations of 12–24 hours when there are concerns about the capacity of the facility to be restored for the next storm or in the presence of high pedestrian traffic or other governing factors.

Finally, the presence of standing water observed during inspections long after the end of an event is a simple visual indication of clogging. Such inspection is easy to perform and may trigger further investigations or preventive maintenance, see also Section 9.5 In the context of AM, the emergence of new methods to monitor the water depth with low-cost sensors or the use of still photos or video footage bear promise as to simplifying the tasks of drawdown assessment or the presence of standing water (Cherqui *et al.*, 2020; Yang *et al.*, 2022).

### 5.3.3 Where does clogging occur?

For most infiltration systems, including both centralized and source control facilities, clogging forms at the top of the infiltration media, only penetrating the first few cm. As the clogging results from sediment deposition and/or compaction, the clogging layer tends to be visible, easy to detect and clean or remove, if necessary. To a lesser extent, clogging may also occur at transition layers, specifically between the media of the infiltration facility and the substratum when the media is much more porous and permeable than the underlying soils. In that case it has been suggested that a geotextile between these layers can fix the clogging (e.g., Siriwardene *et al.*, 2007 on biofilters and Proton, 2008 on infiltration trenches), however in practise these geotextiles have shown to suffer from clogging as well, implementation of appropriate transitions in gradations of materials has been adapted instead (van Duin, 2023).

When a ponding zone exists within an infiltration facility, clogging mainly occurs at the bottom as shown in Figure 5.6 for a large infiltration basin (Gonzalez-Merchan *et al.*, 2012). The same process has been observed for smaller facilities like infiltration trenches (e.g., Proton, 2008) or biofilters (e.g., Blecken *et al.*, 2021). This means that the decline of the permeability of the sides tends to be negligible

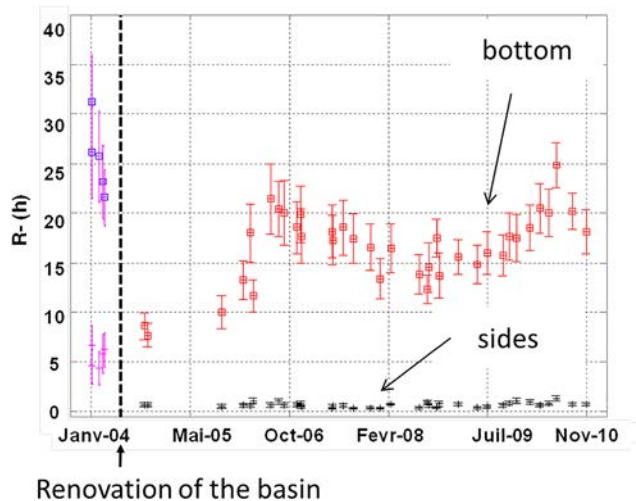


**Figure 5.6** Example of evolution of the hydraulic resistance ( $R$ ) of the sides and the bottom in the basin Django Reinhardt in Chassieu, France. The basin has an area of about 8000 m<sup>2</sup> accommodating a 185 ha catchment with a mean runoff coefficient equal to 0.4. In this case, the bottom got clogged but the basin continued to infiltrate properly along its sides. A basin is considered to have become clogged when  $R$  is higher than 24 hours. This occurred before it was renovated in 2004. The hydraulic resistance of the bottom decreased after spontaneous vegetation growth between 2006 and 2008. (Source: [Gonzalez-Merchan et al., 2012](#)).

over time. However, in some cases, the sides can contribute to clogging of the bottom when their slopes are steep, non-vegetated and thus highly erodible ([Blecken et al., 2021](#)).

For infiltration basins, the clogging process of the bottom shows a high degree of heterogeneity. Unsurprisingly, clogging develops primarily in the areas that are most exposed to the incoming water (i.e., primarily near the inlets). Over time, the footprint of the area influenced by the clogging extends until it occupies the entire surface. When the bottom is completely clogged, the sides provide the main avenue for infiltration. The provision of a forebay is generally a good practice to slow down this process. It also allows for easier maintenance.

Similarly, for linear infrastructure (e.g., swales, vegetated or non-vegetated permeable pavements along conventional roads or car parks), clogging first develops at the surface near the interface between the impermeable upstream areas and the infiltration facility (e.g., [Al-Rubaei et al., 2015](#)).

For the case of permeable pavement structures such as porous asphalt, clogging is also superficial. Clogging tends to occur in areas subject to high tangential stresses (e.g., turning or manoeuvring areas) that leads to the stripping of the top layer material ([Azzout et al., 1994](#)). It also occurs at the interface between the impermeable and permeable pavement areas, in the vicinity of construction activities or in areas fronting green spaces with overhanging vegetation ([Azzout et al., 1994](#); [Blecken et al., 2017](#)). To restore the permeability of such systems, many experiments on maintenance techniques were carried out (e.g., [Balades et al., 1995](#); [Chopra et al., 2010](#); [Drake and Bradford, 2013](#); [Faure and Lemaire, 1990](#); [Henderson and Tighe, 2011](#); [Van Duin et al., 2008](#); [Winston et al., 2016](#)). Water pressure cleaning systems coupled with immediate vacuuming are among the most efficient methods to restore an acceptable permeability. For permeable asphalt, a pressure of 4 MPa for preventive maintenance and from 10 MPa to 30 MPa for preventive maintenance were suggested by [Faure and Lemaire \(1990\)](#), [Balades et al. \(1995\)](#). For full restoration, surface milling turned out to be inevitable ([Azzout et al., 1994](#); [Winston et al., 2016](#)). However, standardized maintenance procedures still need to be developed. The major role that vegetation plays is addressed separately in [Section 5.3.5](#).

### 5.3.4 The dynamics of clogging

The temporal dynamics of clogging are very difficult to assess with the question of the time it takes for a specific facility to get clogged even more so. The longevity of facilities is highly site and condition specific as a function of the original design configuration, uses, environment, climate, maintenance and operation routines, and so on). Virtually no long-term studies exist that monitor an infiltration facility after it had originally been installed to complete clogging. In addition, the procedures employed in assessing the evolution of clogging have proven to be highly variable and often questionable. For instance, do low hydraulic conductivities equate to the occurrence of clogging? Experience has shown it to be not so simple. [Gonzalez-Merchan \*et al.\* \(2012\)](#) showed an example of an infiltration basin that had been suspected to be clogged, based on point measurements showing low permeability of the bottom. However, this 'apparent' clogging did not compromise the overall hydraulic performance during heavy storms after 8 years of operation. Similarly, [Le Coustumer \*et al.\* \(2009\)](#), in their review of 37 small Australian biofiltration systems, with age ranging from a few months to three years, concluded that more than 40% of them were below the recommended conductivity of 180 mm/hour but that they (fortunately) continued to perform well because they had effectively been oversized.

Without standardized long-term studies that would facilitate true comparisons (i.e., by using the same methodology, the same indicators and the same considerations with respect to clogging), answering the question of up to what point a structure can be considered clogged or in need of maintenance is difficult, for the time being here one has to rely on experts' judgement.

Despite these considerations, studies have been carried out all over the world. They illustrate the great diversity of the temporal evolution of clogging as a function of the local context. For large structures, the clogging dynamics reported in the literature are extremely diverse, ranging from a few years ([Lindsey \*et al.\*, 1992](#)) to decades ([Dechesne \*et al.\*, 2002](#)). The case of decades was observed on basins in the eastern part of the Lyon region in France implemented on fluvio-glacial soils and equipped with upstream settling tanks. The clogging was found to be progressive and take a long time, except in one particular case that corresponded to deficient rehabilitation (i.e., poorly removed sediment deposits).

With respect to smaller assets (e.g., bioretention systems, grassed swales, trenches), there is also a large variety of results ([Yang \*et al.\*, 2022](#)). They range from completely clogged assets to assets that, despite a decrease in permeability, still do the job in terms of infiltration after the same number of years in operation. For example, a German study ([Kluge \*et al.\*, 2018](#)), showed that the hydraulic conductivity of most of the 22 grassed swales studied with a substrate composed of sand and loam/silt still met the technical guideline requirement (i.e., between  $10^{-3}$  and  $10^{-6}$  m/s or 3.6 and 3600 mm/h) after 11–22 years of operation. The same trend was observed for biofilters reported by Austrian researchers ([Haile \*et al.\*, 2016](#)). Those facilities consisted of a small upstream sedimentation tank followed by a biofilter with a typical media composition. The results indicated that the hydraulic conductivity decreased 1–2 orders of magnitude after 5–7 years of operation but still complied with the Austrian design standard value which ranged from  $10^{-3}$  to  $10^{-5}$  m/s (36–3600 mm/h). This finding resulted in the recommendation of a preventative maintenance frequency of 7 years.

Other studies on bioretention cells ([Paus \*et al.\*, 2014](#); [Willard \*et al.\*, 2017](#)) suggest that the assets studied can provide many years of effective infiltration (i.e., more than 6 and 7 years, respectively). The experience gained in Lyon, France with respect to a campus car park with a porous structure and permeable asphalt pavement showed that clogging had been quite slow even considering it had not had any maintenance for over 10–20 years. In contrast, a Swedish study ([Al-Rubaei \*et al.\*, 2015](#)) carried out on two grassed swales made of sand with a crushed stone layer underneath were found to have been completely clogged after 9 and 14 years, respectively. The explanation included the use of too fine infiltration media, compaction caused by using the swale as temporary roadside parking, and the possible accumulation of additional fines due to winter maintenance of the roads themselves.

A study conducted in Brazil ([Barraud \*et al.\*, 2014](#)) showed completion clogging of an infiltration trench composed of crushed stone (i.e., without vegetated topsoil) on a silty soil after only one year. The global hydraulic resistance had increased by more than 9 times over this period. The clogging was

explained by the very high concentrations of suspended solids (reaching 2000 mg/L) brought to the system because of intense rain fall events.

Even if it is impossible to predict the lifespan of an infiltration system as far as clogging is concerned, some qualitative trends can be distinguished. Their design (e.g., sizing and composition integrating the consideration of environmental and social conditions) is crucial. The presence of vegetation as part of the assets, as discussed in the next section, may be able to reduce the advent of clogging.

### 5.3.5 Role of vegetation

Many infiltration assets are nowadays vegetated and designed as NBS. [Dagenais et al. \(2018\)](#) explored the scientific-based literature with respect to the global performance of bioretention systems and, in particular, the potential role of the vegetation in reducing clogging through four questions:

- (1) Are vegetated systems more effective than unvegetated ones?
- (2) Do plant species differ as to their effectiveness?
- (3) Are native species more effective than exotic ones?
- (4) Are diverse systems more efficient than monocultures?

With respect to the first question, the research studies confirm the beneficial effects of vegetation as to the evolution of permeability over time. The vegetated systems turned out to be more effective than the unvegetated ones. This has been demonstrated in both several column studies (e.g., [Le Coustumer et al., 2012](#) or [Fowdar et al., 2022](#)) and in the field ([Virahsawmy et al., 2014](#); [Gonzalez-Merchan et al., 2012, 2014](#); [Hatt et al., 2007, 2009](#)). The growth, senescence, death and degradation of plant roots create pores and macropores that can maintain soil porosity, permeability and thus retard clogging. The wind-induced movement of plant stems which loosens the surface of the filtering medium also helps to prevent surface clogging. This is true for both centralized and source control facilities as demonstrated by [Gonzalez-Merchan et al. \(2014\)](#): a study of an infiltration basin near Lyon, France compared the role of different zones covered by spontaneous types of plants (*Phalaris arundinacea*, *Polygonum mite*, *Rumex crispus*) found *in situ* versus similar non-vegetated zones during eight field campaigns in one year. The results clearly showed a positive impact of vegetation on the hydraulic performance, in particular during the growth of the plants over the summer months. The hydraulic conductivity over this period was two to four times higher than that for bare areas or in vegetated zones during the plant rest periods. The substratum of the basin was the original soil made of quaternary deposits.

[Virahsawmy et al. \(2014\)](#) carried out similar measurements albeit for smaller facilities, that is, seven raingardens less than ten years old in Melbourne, Australia. These sites had both vegetated and unvegetated areas. The vegetation species at the sites were the same consisting of grasses, sedges and rushes with an extensive and fibrous root system and a high proportion of fine roots. While the sites varied with respect to age and configuration. They had been all constructed using a similar fine sandy filter medium. The results confirmed that the infiltration rates around the plants were statistically much higher even when the sediment deposition was high.

With respect to the second question, scientific studies indicated that certain plant species are more suitable than others. For example, for bioretention systems, those with greater root mass density and root diameter were found to be most appropriate ([Goh et al., 2017](#); [Hart, 2017](#); [Le Coustumer et al., 2012](#)), in particular. In the presence of tree species ([Fowdar et al., 2022](#)), [Archer et al. \(2002\)](#) found a positive correlation between the volume of roots and the saturated conductivity of soil, especially for older roots that had undergone shrinkage and expansion over time. This was also demonstrated on larger systems (i.e., an infiltration basin) where spontaneous vegetation had developed ([Gonzalez-Merchan et al., 2014](#)).

With respect to the question pertaining to the use of native vegetation, no evidence was found to prove that native plants may be more efficient than exotic ones as far as retarding clogging is concerned. Larger centralized facilities are more prone to show the spontaneous introduction of various plant species (most often native but unfortunately often invasive species too) even if appropriate plant species

had been selected and planted when the basin was first constructed (Saulais, 2011). Maintenance is thus needed whatever the nature of the vegetation originally planned.

The last question addresses the appropriateness of using a diverse mix of plants rather than a monoculture in infiltration systems. The question is mainly relevant for source control facilities. After all, large, vegetated infiltration basins are usually planted with different species in the first place. In the long run, the plant assemblage generally evolves with a simplification of the original mix due to the dominance of certain species and the spontaneous emergence of exogenous, possibly invasive plants. Here again, maintenance is necessary as for other vegetated areas (Saulais, 2011). For bioretention systems, Dagenais *et al.* (2018) showed a lack of evidence to confirm the superiority of a diverse set of plants and a strong need for experiments comparing systems of different plant richness. This will help in determining not only if there is a measurable benefit for biodiversity but also to determine the best combination of plants based for example on their functional traits even though plant diversity can provide many benefits such as aesthetic value (and thus social acceptance), contribution to local biodiversity, and possibly greater resistance to disturbance. However, the choice of mixed or unmixed vegetation appears to be a secondary issue as far as clogging is concerned, the only issue being the presence and nature of the plants used.

### 5.3.6 Concluding remarks on clogging

NBS relying on infiltration offer many benefits but are prone to clogging. Managing them in space and time is, or should be, part of AM strategies. This is even more necessary given the increasing number of infiltration facilities installed. However, their AM depends on several aspects:

The first aspect (although not addressed so far because it does not explicitly concern clogging) pertains to the complexity of the global management of these infiltration facilities:

- Where are the facilities located? It is essential to identify the location of the devices implemented in our urban context. This is particularly the case for highly dispersed source control measures whose multifunctional nature sometimes masks their primary hydraulic function.
- Who manages them? As these facilities tend to be multifunctional, and can be private or public, they often involve many actors in their management which introduces complexity in terms of both maintenance and intervention (Cossais *et al.*, 2017; Werey *et al.*, 2016). For example, in Bordeaux, France, the regional water department looks after a facility when it is 'grassed and not planted'. However, if the facility is planted, its management is to be provided by the Parks Department of the local municipalities (Werey *et al.*, 2016).

A second aspect concerns the factors to prevent or limit the evolution of clogging. According to the surveys carried out on these systems, it is recognized that their durability (i.e., their proper hydraulic functioning) depends largely on the initial design and construction of the systems. The most sensitive points are:

- Properly characterize the soils in place and carefully formulate the added substrates/growing media, avoiding fines where possible, and ensuring good initial hydraulic conductivity. Typical compositions of added substrates from different guidelines are summarised in Beryani *et al.* (2021). In semi-arid regions, some fines and wicking systems may be needed to provide adequate moisture to sustain the vegetation. The hydraulic conductivity may be less in the early days of the facility until the structure of the infiltration bed is established, requiring temporary gravel-based chimneys to prevent standing water. Skorobogatov (2014) provides an introduction to the relation between vegetation and hydrological properties of soils.
- Use vegetation to the greatest extent possible, with vegetation having greater root mass density and diameter being most appropriate.
- Analyse the upstream catchment carefully to ensure that it does not produce too many fines. Pre-treatment (e.g., forebays or sumps) is also a good practice.
- Anticipate potential uses or abuses, especially those that may accelerate compaction.



Many relevant recommendations exist in published guidelines (e.g., [County of San Diego, 2014](#); [Fassman, \*et al.\*, 2013](#); [Melbourne Water, 2023](#); [NCDEQ, 2018](#)).

A third aspect concerns the methods for identifying and monitoring the proper operation of the infiltration facilities whatever their original design composition. Different techniques and methods exist to aid in detecting or measuring the evolution of clogging, as a function of the type of the system, the objectives and the means that the facility managers can implement. Unfortunately, at this stage, none of them is standardized. The method can consist of a simple visual inspection, for instance for the presence of standing water one or two days after a (heavy) storm event, significant sediment deposits, eroded areas, deterioration of the vegetation or simply unaesthetic aspects. This can be accompanied by hydraulic conductivity measurements, utilizing one of the various methods available. It can also be based on continuous measurements of water depths or even of inflows and/or outflows.

Given that the context of the implementation of infiltration facilities is increasingly uncertain (e.g., with climate change resulting in longer dry periods coupled with more intense wet spells) while their use is increasing as part of overall urban stormwater management strategies, knowledge pertaining to their hydraulic efficiency is becoming vital. Therefore, the development of rigorous monitoring methodologies may become imperative. They need to be nimble and inexpensive given the number of facilities. The use of low-cost sensors and photo or video footage seems promising. In any case, as far as the potential for clogging is concerned, preventive maintenance must be encouraged. It is simpler, cheaper and more effective. Recommended maintenance actions are well detailed in the scientific and technical literature (e.g., [Beryani \*et al.\*, 2021](#); [Blecken \*et al.\*, 2017](#); [CIRIA, 2007](#); [NCDEQ, 2018](#); [TRCA, 2016](#)) and discussed in more detail in Chapter 10.s

## 5.4 DETERIORATION OF PLASTIC PIPES

### 5.4.1 Introduction

Plastics are used for a wide range of commercial and industrial piping applications. Polyvinyl chloride (PVC), polyethylene (PE) and polypropylene (PP) are the most popular polymer materials for sewer systems. Fibre reinforced plastic (FRP) is an alternative for lighter pipes with higher stiffness requirements. Irrespectively of the construction material, numerous factors can potentially affect the physical, chemical and mechanical properties of plastic pipes. From the production process until the end of their operational lifetime, an overview of the governing factors and failure mechanisms is presented in this section.

### 5.4.2 Production phase

The most common production process for polymer particles is suspension polymerization. Additives and fillers are added to the polymer matrix during the production phase to improve the chemical and physical properties, respectively. The main applied additives include plasticizers and stabilizers which affect the behaviour and degradation rate of the product during its lifetime. In particular, the objective of plasticizers is the replacement of some of the monomers of the polymer chain, which leads to a higher degree of mobility and therefore higher flexibility. Stabilizers are used to enhance the material resistance against chemical attack (e.g., UV radiation) and other external factors ([Cardarelli, 2008](#)).

Each process within the production phase of plastic pipes and fittings can influence the durability of the end-product. For instance, the levels of water and oxygen during the polymerization stage affect the formation and quality of the produced PVC particles ([Butters, 1982](#)). Another factor is the level of gelation, which relates to the breaking of the boundaries of primary particles and the formation of a new continuous polymer chain ([Visser, 2009](#)). The gelation level is affected by the degree of polymerization ([Fujiyama & Kondou, 2004](#)) and plays a crucial role in the mechanical response of the polymer material ([Moghri \*et al.\*, 2003](#)). The mechanical properties are established based on the polymer's morphology ([Benjamin, 1980](#); [Kuriyama \*et al.\*, 1998](#)), as well as its orientation and molecular mobility ([Fillot \*et al.\*, 2006](#)). Furthermore, impurities and voids in the polymer composition, usually referred to in the literature as inherent defects, are introduced during production forming crack

initiators, while their occurrence seems to be inescapable (Johansson & Tornell, 1987). The wear observed at the surface of pipe extruders (Gladchenko *et al.*, 1997) is a possible source of inherent defects.

Additionally, imposing residual stresses during production is inevitable due to the different cooling rates between the inner and outer pipe surface (Siegmann *et al.*, 1981), influencing the mechanical performance of the produced pipe (Siegmann *et al.*, 1982). A faster cooling rate or a larger pipe wall thickness will most likely result in higher levels of residual stresses (Janson, 2003; Scholten *et al.*, 2016). Irrespective of their magnitude, residual stresses determine the crack propagation mechanisms as they modulate the stress profile through the pipe thickness (Chaoui *et al.*, 1987), increase the brittle-ductile temperature (Scholten *et al.*, 2016), and, accordingly, have a dreadful effect on the operational lifetime. The impact of the residual stresses is more profound in the case of pressurized pipes as the combination of internal pressure and tensile residual stresses is applied to the inner surface of the pipe (Hutař *et al.*, 2013; Poduška *et al.*, 2016).

Furthermore, nowadays non-pressurized PVC pipes are constructed with a structured wall composed of three layers, in which the middle layer consists of recycled or foamed material. This type can bear flexural deformations almost as efficiently as single-layer PVC pipes. Nonetheless, the performance is comparatively lower under conditions of tensile stresses (Makris *et al.*, 2021), which denotes a crucial potential failure factor in case of low-quality installation and/or differential soil settling.

#### 5.4.3 Installation phase

The installation phase includes the excavation of an open trench, preparation of the soil bedding, laying of the pipe, and soil covering and compaction. Nonetheless, during transport and installation, scratches and dents can occur on the pipe surface. Such permanent deformations are potential stress risers, which under certain operational conditions can eventually result in failure. Additionally, poor soil compaction leads to pipe ovalisation, imposing high tensile stresses at the 12 and 6 o' clock positions (top and bottom) of the inner pipe surface and at the 3 and 9 o' clock positions (right and left side) of the outer pipe surface. In pressurized pipes, the internal pressure is counteracted by a uniform external pressure on the pipe exerted by homogeneous soil embedding, lowering the probability of crack formation (Hutař *et al.*, 2011). An additional factor that can accelerate material degradation concerns the storage conditions prior to installation, especially concerning PVC pipes. Exposure to UV rays leads to photochemical degradation, affecting the mechanical properties of PVC pipes (Anton-Prinet *et al.*, 1999; Hussain *et al.*, 1995). Figure 5.7 presents a case of poor-quality installation in The Netherlands. The defect was classified as a 'complicated crack' according to visual inspection standard NEN 3399 and concerned a crack which had been initiated at the pipe crown and progressed to the side. The pipe was found during excavation to be in direct contact with the concrete cover of a pipe for district heating. In this case, the contractor was found to be responsible as an external piece of pipe was found to cover the damaged pipe section.

#### 5.4.4 Operational phase

Four main ageing mechanisms can be observed during operation: physical ageing, mechanical degradation, chemical degradation and environmental stress cracking.

Physical ageing is a known mechanism in polymers which imposes changes on certain properties of a material as a function of time, even at a constant temperature and independent of external factors (Hutchinson, 1995). Amorphous (or glassy) polymers, such as PVC, experience physical ageing because they were cooled to a temperature below their glass transition temperature, and, hence, are not in a thermodynamic equilibrium state. In this non-equilibrium state, the glassy polymer has excessive thermodynamic properties and there is a continuous effort to reach the equilibrium state (Hutchinson, 1995). Physical ageing can be traced by reduction in volume and enthalpy, but also by changes in the mechanical properties (Rabinovitch & Summers, 1992). The polymer becomes stiffer and more





**Figure 5.7** A case of poor-quality installation. An external piece of pipe was found to cover a PVC sewer pipe at the point of failure. (Courtesy K. Makris).

brittle (Figure 5.8), while its creep and stress relaxation rates decrease (Struik, 1977). In principle, physical ageing is an inevitable, although reversible process in polymers (Hutchinson, 1995), which is accelerated at higher temperatures (Visser *et al.*, 2011). The process of physical ageing occurs also in semi-crystalline materials, like PE and PP. In this case, physical ageing occurs in the amorphous part of the semi-crystalline polymer (Struik, 1977).

Mechanical degradation is the result of loadings that are applied on the pipe with their level surpassing the polymer's fracture threshold. It surfaces as fissures (e.g., crazes and cracks) or breaks.

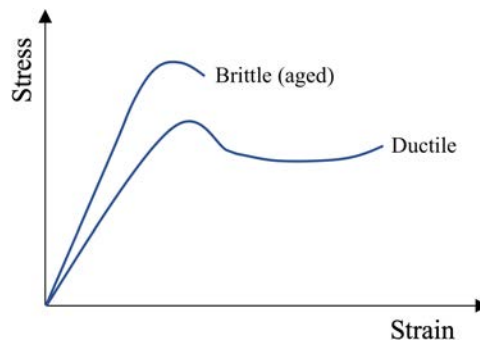


**Figure 5.8** Effect of physical ageing on the response of amorphous polymers to deformation. (Courtesy K. Makris).

The loadings include stresses from internal pressure (if any), deflections due to the vertical loading of soil and the production phase (i.e., residual stresses). Additional stresses can be exerted by axial bending due to improper installation and soil settling. The quality of the pipe production can be a critical factor for the durability of polymer pipes, since cracks initiate from built-in voids and impurities. Subsequently, the propagation (rate and direction) of the cracks is determined by the magnitude and direction of the applied stresses. This failure mechanism is known as slow crack growth (SCG). A usual cause of failure for plastic pipes concerns external impacts (e.g., when a pipe is hit by an excavator). In this case, mechanical degradation surfaces as rapid crack propagation (RCP). [Figure 5.9](#) illustrates the case of a breakage caused by external impact. The imprint of an excavator's bucket is obvious while the large number of other installations in the direct vicinity of the damaged pipe suggests extensive past excavation activities in the area.

Chemical degradation concerns the effect of chemical reactions that occur between the pipe material and the environment, inside and/or outside of the pipe. Chemical degradation can result in breakage of the polymer covalent bonds, which constitute the main back bone of a polymer chain. The breakage of covalent bonds leads to chain scission and molecular weight reduction. A known indication of chemical degradation is the discolouration that is often observed on PVC pipes ([Figure 5.10](#)). This effect is the result of dehydrochlorination, that is, HCl abstraction ([Breen, 2006](#)), which is caused by the formation of sequential conjugated polyenes ([Arnold, 2003](#)). The impact on the mechanical properties is usually expressed with the term 'stress corrosion cracking', which includes four individual stages ([Choi et al., 2005](#)): initiation of microcracks, slow crack growth, clustering of cracks and clusters growth. Research on PVC sewer pipes that had served for 40 years before excavation revealed that discolouration is limited to the pipe surface ([Makris et al., 2021](#)).

Last, environmental stress cracking (ESC) shares a similar failure pattern in terms of shape with slow crack growth. It is a purely physical process propagated by the applied stresses and accelerated by the effect of an active environment ([Bishop et al., 2000](#)), since diffusion is the mechanism that increases the sensitivity to fractures due to formation of plasticized layers and surface energy reduction ([Arnold, 2003](#)). Research on the ESC mechanism under gas and liquid environments indicate that the combined effect of environment and stress intensity results in a lower load bearing capacity ([Breen, 1993, 1994, 1995](#)). In general, a wide range of amorphous and semi-crystalline polymers was studied to explore their ESC resistance ([Robeson, 2013](#)), concluding that signs of ESC may initiate under



**Figure 5.9** A breakage of a PVC sewer pipe due to an external impact (hit by excavator). (Courtesy K. Makris).



**Figure 5.10** PVC pipe with obvious signs of discolouration on the external side. (Courtesy K. Makris).

certain combinations of ‘material-environment’. Finally, additional failure mechanisms to those of the polymer matrix can be found in FRP pipes. Fracture of one or multiple fibres could locally result in a lower stiffness (Alabtah *et al.*, 2021). Nonetheless, the addition of reinforcing fibres certainly adds to the durability, while their usual placement at two different directions within the pipe wall compensates for fibre failure, keeping the pipe operational (Fragoudakis, 2017). Further, detaching of the fibres from the polymer matrix, commonly known as debonding, can also be observed (Alabtah *et al.*, 2021).

## 5.5 BIOGENIC CORROSION OF CONCRETE

### 5.5.1 Introduction to biogenic sulphide corrosion of concrete sewer pipes

The assessment of the durability of concrete sewer pipes requires a thorough understanding of the underlying chemo-mechanical degradation processes. In aggressive chemical environments, concrete degradation may be promoted by the reaction of sulphates with the hydrated cement paste (Allahverdi & Skvara, 2000; Attiogbe & Rizkalla, 1988; Neville, 2004; Parker, 1945) or by alkali-silica reactions between reactive siliceous aggregates and the alkaline pore solution in hardened concrete (Farny & Kerkhoff, 1977; Rajabipour *et al.*, 2015). In both cases, the reaction products induce expansive strains in the concrete material, which may trigger micro-crack development. Another relevant chemo-mechanical damage process in concrete is carbonation, which is associated with the formation of calcium carbonates due to the reaction of carbon dioxide with the hydrated cement paste (Ismail *et al.*, 1993; Savija & Lukovic, 2016). This mechanism not only contributes to concrete degradation but also promotes corrosion of the steel reinforcement. This section particularly focuses on biogenic sulphide corrosion (Bielefeldt *et al.*, 2010; Cho & Mori, 1995; Davis *et al.*, 1998; Grengg *et al.*, 2015; Ismail *et al.*, 1993; Parker, 1945), which is a specific type of sulphate attack occurring in concrete sewer systems (Davies *et al.*, 2001). The content of this section is a summary of the work presented in Rooyackers *et al.* (2022).

### 5.5.2 Modelling of biogenic sulphide corrosion

The process of biogenic sulphide corrosion is schematically illustrated in Figure 5.11 and can be described as follows. The sewerage environment may be rich in sulphur compounds. Under anaerobic conditions, sulphate-reducing bacteria can reduce the sulphur compounds present in the wastewater into hydrogen sulphide gas ( $H_2S$ ). This gas is released from the wastewater into the sewer atmosphere and then makes contact with the wet inner surface along the upper parts of the pipe, where it is



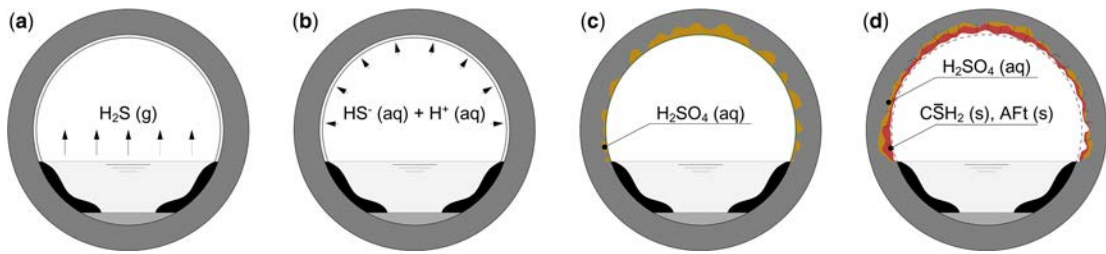


**Figure 5.11** Schematic representation of the process of biogenic sulphide corrosion in concrete sewer systems. (a) Hydrogen sulphide gas ( $H_2S$ ) is formed from sulphur compounds present in the wastewater which is subsequently released into the upper parts of the sewer pipe. (b) Hydrogen sulphide gas reaches the thin moisture layer present along the inner surface of the sewer pipe whereby it dissolves into ionic species  $HS^-$  and  $H^+$ . (c) The dissolved hydrogen sulphide species are converted into sulphuric acid ( $H_2SO_4$ ) by bacteria, as indicated by the yellow colour, which may diffuse into the porous structure of cement. (d) sulphuric acid reacts with cement to form gypsum ( $C\bar{S}H_2$ ) and ettringite (AFt), as indicated by the red colour, which may lead to the formation of micro-cracks and damage along the concrete pipe. The figure has been reprinted from [Rooyackers et al. \(2022\)](#).

dissolved into ionic species, that is, bi-sulphide ( $HS^-$ ) and hydrogen ions ( $H^+$ ). In the presence of sulphur-oxidizing bacteria, the dissolved hydrogen sulphide species are converted into sulphuric acid ( $H_2SO_4$ ) ([Bielefeldt et al., 2010](#); [Cho & Mori, 1995](#); [Marquez-Penaranda et al., 2015](#); [Parker, 1945](#)). Sulphuric acid may diffuse into the porous structure of the cement matrix, where it reacts with dissolved constituents of the hydrated cement paste, resulting in the formation of gypsum ( $C\bar{S}H_2$ ) and ettringite (AFt) ([Attigbe & Rizkalla, 1988](#)). This chemical process affects the mechanical resistance of concrete for two reasons. First, gypsum and ettringite form a porous corrosion layer with inferior mechanical properties compared to the original cement paste ([Marquez-Penaranda et al., 2015](#)). Second, the expansive nature of these reaction products induces tensile stresses in the remaining, intact cement paste ([Attigbe & Rizkalla, 1988](#); [Eriksen, 2003](#); [Mittermayr et al., 2015](#)). If these stresses exceed the tensile strength of the cement paste, they may result in the initiation and propagation of micro-cracks ([Monteny et al., 2000](#)). The net effect of these two aspects is that the amount of undamaged concrete material across the wall thickness of a sewer pipe is reduced over time, which can have serious consequences for the structural load bearing capacity of the pipe. As demonstrated in a recent experimental-numerical study ([Scheperboer et al., 2021](#)), a reduction of 20% of the concrete wall thickness may already reduce the load bearing capacity of a sewer pipe by approximately 40%. Hence, it is important to obtain a thorough understanding of the process of biogenic sulphide corrosion and the consequent degradation of concrete.

This paragraph summarizes the computational modelling framework recently developed in [Rooyackers et al. \(2022\)](#), which can be used for simulating the coupled chemo-mechanical behaviour of concrete sewer pipes under biogenic sulphide corrosion. The process of biogenic sulphide corrosion was modelled by considering a source of sulphuric acid that is produced by sulphur-oxidizing bacteria, which gets into contact with the inner surface of a concrete sewer pipe. The consequent chemical processes were described in terms of a set of diffusion-reaction equations, which include the reactions of calcium hydroxide dissolution, calcium silicate hydrate dissolution and gypsum formation, as well as the corresponding diffusion-reaction processes of the associated ionic species. The diffusion-reaction equations were coupled with a continuum damage model that describes the process of material degradation up to complete failure. One coupling between the chemical and mechanical fields was realized through the definition of a chemically induced growth strain, which determines the expansion effect by gypsum formation on the stresses generated in the concrete. Another coupling followed from the introduction of a chemical damage variable that quantifies the degradation of concrete as a result of calcium silicate hydrate dissolution. Since the presence of damage promotes

the diffusion of chemical species (i.e., damage-enhanced diffusion), the diffusion coefficients of the chemical processes were prescribed to be a function of the generated material damage, by which the model formulation became two-way coupled.

The chemo-mechanical model was implemented within a FEM framework, whereby the numerical update procedure of the coupled chemical and mechanical problems was performed in a so-called segregated fashion. The model predictions were validated by performing dedicated laboratory experiments on cuboidal concrete specimens exposed to a sulphuric acid solution over different time periods, which mimics the temporal development of biogenic sulphide corrosion in concrete sewer pipes. The finite element analyses thus represented the chemo-mechanical response of a cuboidal concrete sample that is exposed at its external boundaries to a specific sulphuric acid solution. The cube had edges of length  $2L = 150$  mm. Due to symmetry of the problem in terms of the geometry and the initial and boundary conditions applied, the main features of the corrosion process in the three-dimensional configuration could be captured accurately by a two-dimensional analysis of the left upper quarter part of the concrete sample, in accordance with the  $L \times L$  computational domain illustrated in [Figure 5.12](#). The computational domain was discretized by 7310 quadrilateral finite elements, with a local refinement close to the left and upper external boundaries to accurately describe the relatively strong concentration gradients that initially may appear at these boundaries. The specific chemical and mechanical material parameters and the initial and boundary conditions applied on the system, respectively, can be found in [Rooyackers \*et al.\* \(2022\)](#).

### 5.5.3 Corrosion experiment

For the validation of the proposed chemo-mechanical model presented in [Section 5.5.2](#), a corrosion experiment was performed in which a set of concrete specimens was exposed to a sulphuric acid solution for different time durations. At two opposite sides of the cube the upper part was equipped with a 50 mm cantilever extension, see [Figure 5.13a](#), which enables hanging the cubes using a PVC support structure in a container with the sulphuric acid solution, as described in more detail below. The composition of the casted concrete specimens included coarse granite aggregates, sea sand and ordinary Portland cement – CEM I 42.5N. The composition is representative of the dry-cast concrete used since the 1950s for sewer pipes in the Netherlands. The water–cement ratio of the composition

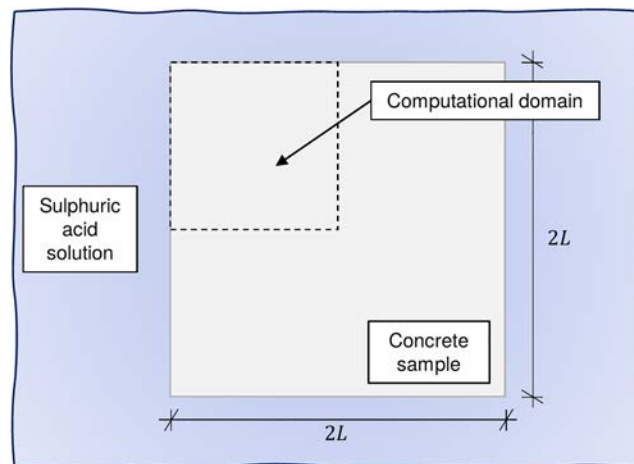


**Figure 5.12** Cuboidal concrete sample exposed to a fixed, sulphuric acid solution. Due to symmetry, the computational domain considers one quarter of the sample geometry. The figure has been reprinted from [Rooyackers \*et al.\* \(2022\)](#).

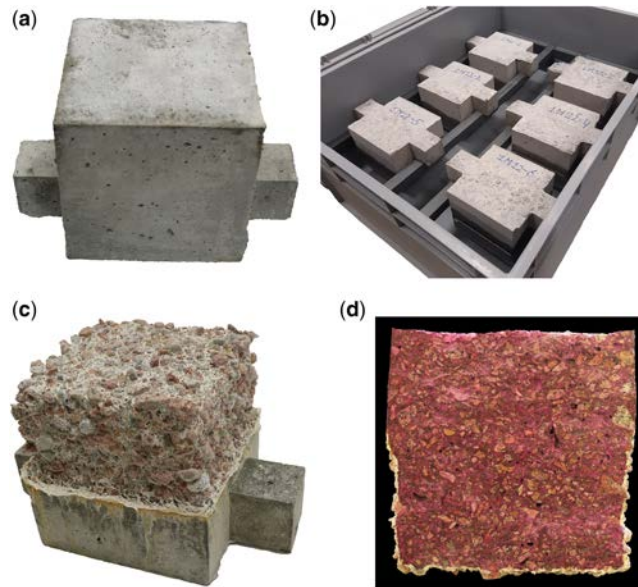


**Figure 5.13** Corrosion experiment on concrete specimens. (a) Cuboidal concrete specimen. (b) Container and PVC support structure used for simultaneously exposing six concrete specimens to a sulphuric acid solution. (c) Corroded specimen after 12 months of exposure to a sulphuric acid solution with a pH of 1. (d) Cross-section of a corroded specimen after 12 months of exposure to a sulphuric acid solution with a pH of 1. From a phenolphthalein test the inner concrete region (pink) and the unspalled part of the outer gypsum layer (beige) can be clearly identified. The figure has been reprinted from [Rooyackers et al. \(2022\)](#).

was equal to 0.35. The formwork of the casted specimens was removed after 24 hours, after which the specimens were kept in water for a hydration period of 28 days. Subsequently, the dimensions of the hardened specimens were measured from 27 different spatial points that were uniformly distributed across the cube. Accordingly, their reference geometry was determined, from which corrosion depths after exposure to sulphuric acid could be measured. The corrosion profiles of the specimen were analysed for six different exposure times, namely 1, 2, 4, 6, 8 and 12 months. Since the assessment of corrosion requires a destructive analysis of the specimens (as described below), for each exposure time six specimens were prepared, resulting in a total number of 36 specimens. Per exposure time the sulphuric acid solution was kept in a separate container. Using a PVC support structure, the concrete specimens were suspended into the container, whereby the bottom part of the cubes was exposed to the sulphuric acid solution, see [Figure 5.13b](#). The pH level of the solution was equal to 1. During the experiment the pH level of the sulphuric acid solution was monitored frequently, whereby it was observed that it slowly increased with time because of the release of hydroxide ions from the cement. The increase in pH level was kept within acceptable bounds by renewing the sulphuric acid solution once per month. The temperature in the experiment was kept constant at 20°C. [Figure 5.13c](#) shows a concrete specimen after twelve months of exposure to the sulphuric acid solution. The degradation effect of chemical corrosion can be clearly observed from the spallation of the outer part of the cube at the bottom. It can be further seen that aggregates have become visible, and that the cement in between the aggregates changed into a white substance with a soft texture, as representative of gypsum. The sediment found in the container underneath the specimen contained the aggregates and gypsum spalled from the specimen. In the experiment, the evolution of the spallation profile over time was not monitored in detail, because of the complexity following from the high sensitivity of spallation to the

local morphology of the concrete material, in combination with the long duration of the experiment. For each of the six exposure times, the average value and standard deviation of the thickness of the corroded layer were computed from the dimensions of the corroded cube in question in relation to its original dimensions. For this purpose, the corroded cubes were halved by means of a tensile splitting test, after which the average thickness and standard deviation of the corroded layer were calculated from measurements taken across the specimen width at five different locations along the cross-sectional height of the corroded (bottom) part of the sample, as performed for six samples per exposure time. Hence, for each exposure time the two statistical values were calculated from 30 measurements in total. An additional refinement of the estimated corrosion layer thickness was necessary to account for the degree of corrosion generated inside the cube. This was done by performing a phenolphthalein test, whereby one of the fracture surfaces was sprayed with a phenolphthalein solution. In the presence of a relatively high pH value, the phenolphthalein took a pink colour, thereby indicating the region in which the sulphuric acid did not penetrate, and the concrete was uncorroded. Conversely, for a low pH value, the phenolphthalein remained transparent, and thereby identified the corrosion depth corresponding to the gypsum formed inside the specimen. For a concrete specimen exposed to the sulphuric acid concentration for a period of twelve months, Figure 5.13d depicts the fracture surface sprayed with phenolphthalein. In this figure the inner concrete region (pink) and the unspalled part of the outer gypsum layer (beige) are clearly recognizable.

#### 5.5.4 Comparison between the experimental and numerical results

Figure 5.14a depicts the experimental (left) and numerical (right) quarter cross-sections of the concrete specimen after exposure to the sulphuric acid solution for a period of twelve months. It can be observed that the unspalled, experimental corrosion layer of gypsum (depicted in beige) has developed rather uniformly along the specimen boundary, with some small undulations caused by inhomogeneities (e.g., aggregates) present in the inner concrete region (depicted in pink). The maximum thickness of the gypsum layer is in good correspondence with that computed by the numerical simulation (depicted in red). Clearly, the undulations are absent in the numerical profile, since the concrete in the inner

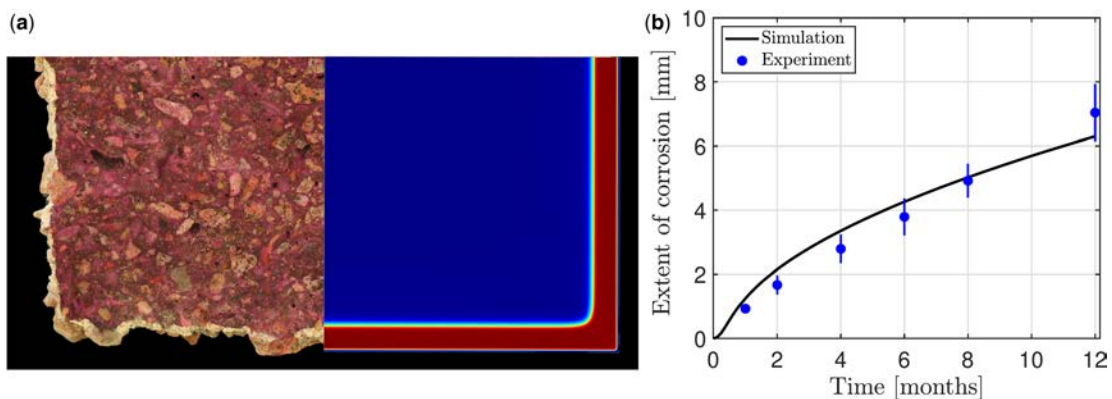


**Figure 5.14** Comparison between experimental results and the numerical simulation results computed with the chemo-mechanical model of Rooyackers *et al.* (2022). (a) Quarter cross-section of one specific concrete specimen after exposure to a sulphuric acid solution for a period of 12 months. In the experimental profile (left) the unspalled gypsum layer is indicated in beige, and the inner concrete region in pink. In the numerical profile (right) the gypsum layer is indicated in red, and the inner concrete region in blue. (b) Time evolution of the corrosion depth. The mean values of the experimental data are indicated by blue solid circles; the corresponding error bar represents the standard deviation. The results of the numerical simulation are designated by the black solid line. The figure has been reprinted from Rooyackers *et al.* (2022).



concrete region (depicted in blue) is modelled as homogeneous. The specific effect of the aggregates on the chemo-mechanical response can be accounted for in the present model by explicitly simulating the heterogeneous concrete micro-structure, see for example, [Bosco \*et al.\* \(2020\)](#), which is a topic for future study. The evolution of the experimental corrosion depth with time is presented in [Figure 5.14b](#) for the six exposure times applied in the test procedure, with the average value and standard deviation indicated by the blue solid circles and the blue error bars, respectively. The trend computed by the numerical model is denoted by the black solid line. It can be observed that the rate of corrosion initially is relatively high, but that it gradually decreases with increasing time. The numerical result adequately corresponds to the experimental result for all six exposure times; at larger times it consistently falls within the standard deviation of the average experimental response, whereby the final corrosion depth corresponding to the gypsum layer formed after twelve months 6.3 mm. It was confirmed that the evolution of the corrosion depth with time as computed by the numerical model can be closely approximated by a power law of which the exponent equals 0.53, indicating that the development of the corrosion depth scales approximately with the square root of time. In summary, it may be concluded that the coupled chemo-mechanical model is able to adequately describe the important features of chemical corrosion observed in the experiments. This demonstrates that the model is suitable for being applied in the numerical analysis of biogenic sulphide corrosion processes taking place in in-situ sewer pipe systems to predict their long-term chemo-mechanical degradation behaviour under practical, relatively complex environmental conditions.

Finally, as systematically demonstrated in [Rooyackers \*et al.\* \(2022\)](#), the process of biogenic sulphide corrosion occurs as follows. Driven by the relatively low ionic concentrations of calcium and hydroxide ions at the external boundary of the cuboidal concrete sample, the calcium hydroxide and calcium silicate hydrates species present in concrete gradually dissolve from the boundary in an inward direction. The calcium ions generated by these dissolution processes subsequently react with the excess of sulphate ions to form gypsum. The excess of sulphate ions in the outer boundary region of the sample results from their inward diffusion, as caused by a relatively high ionic concentration at the boundary under biogenic reactions. The formation of gypsum ends at a specific material point once the calcium hydroxide and calcium silicate hydrates species have fully depleted. The thickness of the outer region increases with time, whereby the associated chemical growth strain is constrained by the inner concrete region. This induces a tensile stress in the inner core region that typically leads to mechanical damage, whereby the amount of damage increases from the core of the sample towards the interface with the outer gypsum layer. The speed of the growth of the gypsum layer and the amount of damage generated in the inner concrete region are significantly increased by the process of damage-enhanced diffusion. Furthermore, the diffusion coefficient has a strong impact on the degradation behaviour of the system, while the chemical growth strain influences the amount of damage but has almost no effect on the thickness of the gypsum corrosion layer.

In [Luimes \*et al.\* \(2023\)](#) the chemo-mechanical degradation of unreinforced concrete sewer pipes applied in domestic service locations is assessed through a systematic, integrated experimental approach, considering 18 new and 35 used sewer pipes. The characteristics and environmental conditions of the sewer pipes are reported, and data obtained from surface condition classification, residual alkalinity tests and XRD analyses are combined to identify the type and degree of chemical attack of the used sewer pipes. Concrete material properties are determined by material tests on sewer pipe samples, providing quantitative insight into the age dependency of the Young's modulus, compressive strength, tensile strength and mode I toughness. All relatively old pipes (installed in the 1920s and 1950s) show substantial chemical attack by biogenic sulphide corrosion (at the inner side of the pipe) and carbonation (at the outer side of the pipe). The time development of the corresponding corrosion depths on average follows a linear trend, whereby the corrosion rate for biogenic sulphide corrosion is about a factor of 1.3 larger than for carbonation. Due to these chemical processes, the mechanical properties of concrete may significantly depend on the age of the sewer pipe. In particular, the average compressive strength and average tensile strength decrease approximately linearly with

the age of the pipe, in correspondence with relative reductions of, respectively, a factor of 1.7 and 1.5 over a period of almost 100 years. The values and time-dependent trends found for the concrete properties and corrosion depths of sewer pipes can serve as input for practical analyses and advanced numerical simulations on their bearing capacity and time-dependent degradation. The experimental results also emphasize the importance of regularly assessing the amount of chemical degradation of (especially older) *in situ* sewer pipes, by determining the (decrease in) effective wall thickness via core sampling and laser profiling.

## 5.6 SUBSURFACE SOIL EROSION AROUND A SEWER PIPE

### 5.6.1 Introduction

Soil erosion by water is a degradation process in which particles are detached from the soil structure and carried away by flowing water. This process can be activated both by overland and subsurface flow (Bernatek-Jakiel & Poesen, 2018). When soil erosion takes place by the way of subsurface flow, its temporal and spatial evolution of the erosion profiles are not visible on the surface, so that the process may remain unnoticed for a long period of time. This aspect makes it generally difficult to monitor and analyse subsurface erosion, which is likely the reason that the number of research studies on subsurface erosion – also referred to as internal erosion – are disproportional compared to those on surface erosion (Bernatek-Jakiel & Poesen, 2018; Poesen, 2018). However, subsurface erosion has been reported as a highly relevant and widespread process (Poesen, 2018), and is the cause of various catastrophic failure phenomena with large societal impact, such as sewer collapse, dam breaks, the formation of sinkholes and the instability of earth dams (Bonelli *et al.*, 2018; Davies *et al.*, 2001; Foster *et al.*, 2000; Walthan *et al.*, 2005; Yang *et al.*, 2019).

One important example of subsurface erosion processes is *soil piping*, whereby relatively large porous networks are created under preferential flow paths (Bernatek-Jakiel & Poesen, 2018; Bernatek-Jakiel *et al.*, 2017; Jones, 2010). Soil piping has been observed in various types of soils, such as loess-derived soils, organic soils, clayey soils and sandy soils (Bernatek-Jakiel *et al.*, 2017), and may be initiated when the soil contains a high percentage of fine particles that are smaller than the average pore space in the soil. When the process starts and small particles are eroded, the pore space increases and individual pores become connected and form channels, which increases the hydraulic permeability and may trigger the release of coarser particles (Bernatek-Jakiel & Poesen, 2018; Jones, 2010). The pipe network that develops may lead to subsidence of the soil structure, and eventually even to severe structural failure, such as an abrupt collapse of the pipe network and the overlying soil structure – termed a sinkhole – or landslides (Bernatek-Jakiel & Poesen, 2018; Walthan *et al.*, 2005). Whether or not a pipe network collapses depends on the loading conditions and on the level of migration of soil particles. If, under the specific hydraulic conditions applied, only the finer particles erode and the coarser particles to some extent maintain a particle contact force fabric, the soil structure preserves its load bearing capacity and does not collapse. This process is denoted as *suffosion* (Fannin & Slangen, 2014; Hunter & Bowman, 2018; Moffat *et al.*, 2011). Conversely, the erosion process is characterized as *suffosion* if, under a strong flow of water, the transport of fine particles is accompanied by the collapse of the contact force fabric of the coarser particles, whereby some form of catastrophic structural failure is induced (Fannin & Slangen, 2014; Hunter & Bowman, 2018; Moffat *et al.*, 2011).

Another important type of subsurface erosion is *void formation*, which may occur around buried concrete pipe systems, such as sewer pipes, industrial discharge lines, tunnels, culverts and storm drains (Meguid & Kamel, 2014; Peter *et al.*, 2018; Wang *et al.*, 2014). Erosion voids can emerge due to ageing or improper construction procedures of pipe systems, with defects (i.e., cracks or gaps) in the pipe system initiating a water flow that locally washes away the soil support. Under continuous growth the erosion void may eventually evolve into a suffosion sinkhole, whereby the bearing resistance of the supporting soil vanishes and the soil structure above the pipe collapses (Indiketiya *et al.*, 2019; Walthan *et al.*, 2005). Sinkhole failures have been reported to happen

within the lifetime of the pipe system, as well as during the period of construction (Walthan *et al.*, 2005), indicating that the rate of the underlying erosion processes is strongly variable and determined by local hydro-mechanical conditions. Various experimental and numerical studies have addressed the effect of erosion voids on the stresses generated in pipe systems and in the surrounding soil, whereby the stress redistribution caused by the appearance of an erosion void is found to be characterized by its location, size and contact angle (Meguid & Dang, 2009; Peter *et al.*, 2018; Tan, 2007; Wang *et al.*, 2014; Yasuda *et al.*, 2017). During void erosion the load transfer from the surrounding soil to the pipe generally takes place more localized, whereby the load magnitude increases. Accordingly, the susceptibility of the pipe system to cracking and damage, and thus to catastrophic failure, also increases (Meguid & Kamel, 2014; Scheperboer *et al.*, 2021; Talesnick & Baker, 1999; Wang *et al.*, 2014).

The following section presents a coupled hydro-mechanical bulk erosion model that may be used for studying soil piping and erosion void formation near and around a sewer pipe system. The content of this section is a summary of the work presented in Scheperboer *et al.* (2022).

### 5.6.2 Modelling of subsurface soil erosion

The erosion model developed by Scheperboer *et al.* (2022) treats the soil as a two-phase porous medium composed of a solid phase and a liquid phase, and accounts for its elasto-plastic deformation behaviour caused by frictional sliding and granular compaction. The kinetic law characterizing the erosion process is assumed to have a similar form as the type of threshold law used in interfacial erosion models (Horton, 1945; Knapen *et al.*, 2007). The degradation of the particle structure under erosion is considered to reduce the effective elastic stiffness of the porous medium and increase its permeability. The reduction in elastic stiffness is accounted for via an *erosion degradation parameter*  $D_{er}$ , which depends on the actual porosity of the soil and quantifies how effectively the mechanical degradation under erosion takes place. Its value ranges as  $0 \leq D_{er} \leq 1$ , whereby the limit cases  $D_{er} = 0$  and  $D_{er} = 1$  represent uneroded and fully eroded soil materials, respectively. The coupled hydro-mechanical model was implemented in the commercial FEM program ABAQUS, whereby the solutions of specific problems were computed in an incremental-iterative fashion using a staggered update scheme. The details of the model formulation and the numerical implementation can be found in Scheperboer *et al.* (2022).

Two practical case studies are considered that relate to a sewer system embedded in a sandy soil structure. The first case study treats *soil piping* caused by *suffusion* near a sewer system subjected to natural ground water flow, and the second case study considers the formation of a *suffosion erosion void* under strong ground water flow near a defect sewer pipe. The defect is located at the bottom of the pipe and has a width of 20 mm, representing a gap created by a sudden failure of a pipe joint. The effects on the erosion profile and the soil deformation behaviour by plasticity phenomena are elucidated by comparing the computational results to those whereby the constitutive behaviour of the granular material is modelled as elastic. The results of this comparison study illustrate the importance of including an advanced elasto-plastic soil model in the numerical simulation of erosion-driven ground surface deformations and the consequent failure behaviour.

The specific geometry considered in the hydro-mechanical analyses is depicted in Figure 5.15. The soil structure consists of a top layer of dry sand with a thickness of 2.27 m, which is supported by a fully saturated sand layer with a thickness of 1.50 m, followed by a relatively thick, fully saturated clay layer. The location of the centre of the sewer pipe corresponds with the ground water table at 2.27 m depth. The inner diameter and wall thickness of the round sewer pipe are 400 and 65 mm, respectively. The sewer system is covered by 2 m of dry sand, which is representative of the conditions in The Netherlands (Bolderman *et al.*, 2003). The specific part of the geometry simulated with the FEM model is indicated in Figure 5.15 by the light shaded rectangular section of  $6 \times 3 \text{ m}^2$ . The mechanical and hydrological initial and boundary conditions used in the FEM analyses and the material parameters of the sandy soil and concrete sewer pipe can be found in Scheperboer *et al.* (2022).

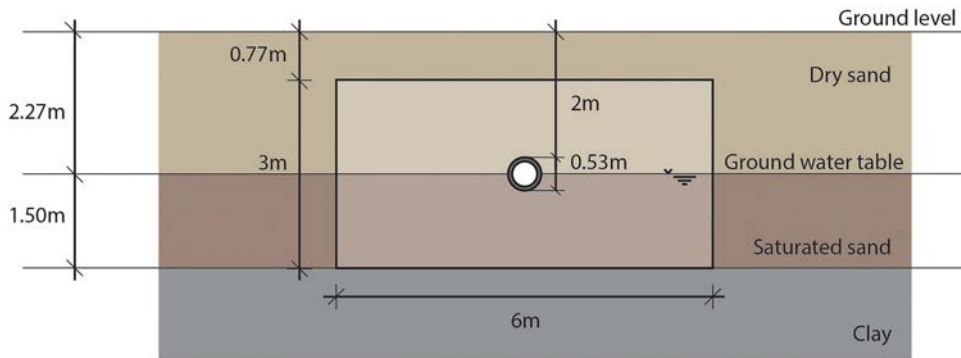
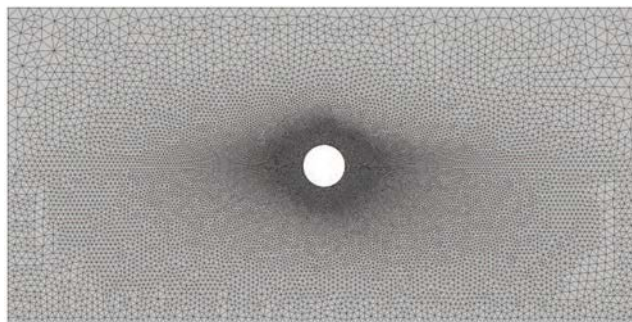


**Figure 5.15** A round sewer pipe embedded in a stratified soil structure consisting of a 2.27 m thick, dry, sandy upper layer, followed by a 1.50 m thick saturated sandy layer, and finally a virtually impermeable, thick clay layer; the location of the centre of the sewer pipe corresponds to the ground water level at 2.27 m depth, and the light shaded area of  $6 \times 3 \text{ m}^2$  indicates the computational domain used in the FEM simulations. The figure has been reprinted from [Scheperboer et al. \(2022\)](#).

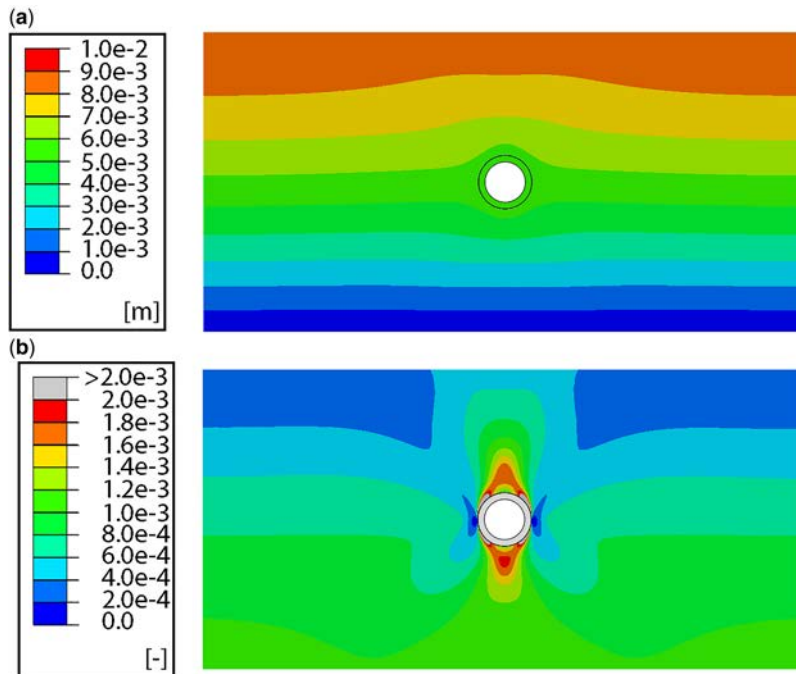
The computational domain was modelled as two-dimensional, assuming a plane-strain condition in the out-of-plane direction. The soil structure with the elasto-plastic sand behaviour was discretized with 47,046 plane-strain 6-node iso-parametric coupled temperature-displacement elements, which were equipped with a 3-point Gauss quadrature. The sewer pipe was simulated as elastic and was discretized by 2089 plane-strain 6-node iso-parametric elements with a 3-point Gauss quadrature. As indicated in [Figure 5.16](#), the mesh of the soil structure was refined towards the (coherent) interface with the sewer pipe to accurately simulate the local erosion profile. A preliminary mesh refinement study had indicated that the present discretization was sufficiently fine for obtaining converged numerical results for the two case studies.

### 5.6.3 Soil piping due to natural groundwater flow near a sewer system

The FEM simulation started with the application of the initial loading generated by the dead weight of the soil structure and the concrete pipe. The vertical settlement profile resulting from the dead weight loading is depicted in [Figure 5.17a](#), and the corresponding deviatoric plastic deformations are illustrated in [Figure 5.17b](#). The plastic deformations are reflected in the contour plot by the deviatoric invariant  $\bar{\gamma}^p = \sqrt{(2/3)\gamma^p : \gamma^p}$  with  $\gamma^p$  the deviatoric plastic strain. It can be observed from



**Figure 5.16** Finite element discretization used in the two case studies. The figure has been reprinted from [Scheperboer et al. \(2022\)](#).



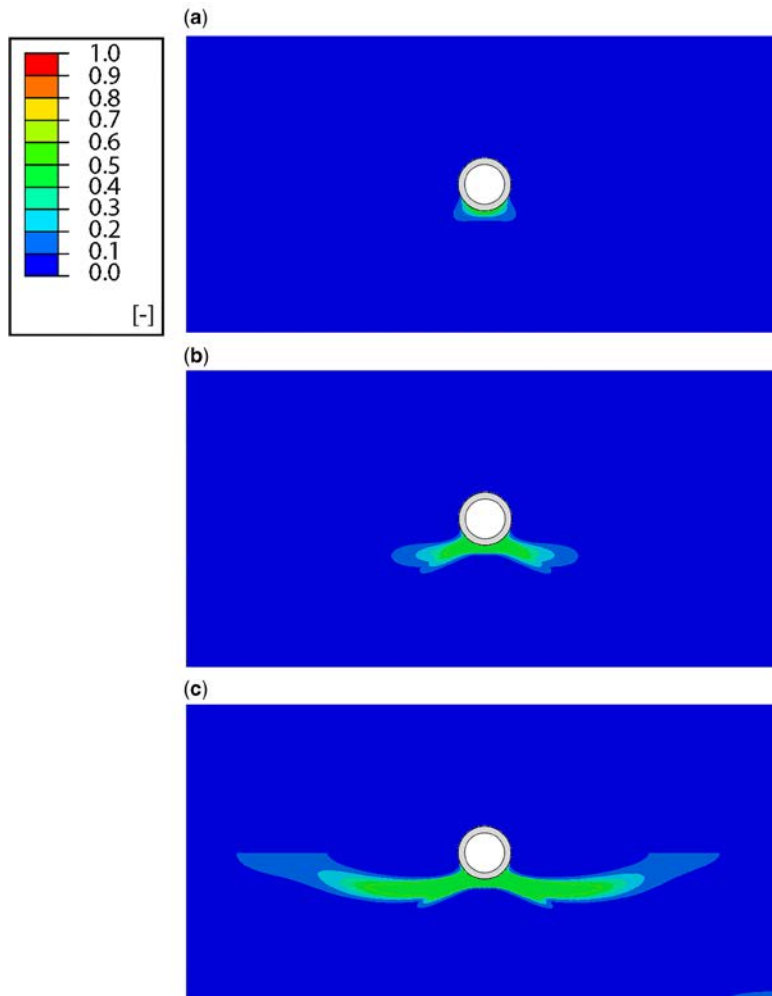
**Figure 5.17** FEM solution resulting from the application of the initial, dead weight loading; the figure shows the spatial variation of (a) the vertical displacement  $w$  (in m) and (b) the deviatoric plastic strain invariant  $\bar{\gamma}^p$ . The figure has been reprinted from [Schepherboer et al. \(2022\)](#).

Figure 5.17a that the initial settlement profile was fairly uniform along the horizontal direction, with the settlements above the sewer pipe being slightly smaller than those at the left and right domain boundaries. Obviously, this difference may be ascribed to the relatively low effective density of the hollow sewer pipe. As indicated in Figure 5.17b by the grey-hatched area, the deviatoric plastic deformation was maximal at the top-left and top-right of the pipe circumference, reaching a value of  $\bar{\gamma}^p = 0.45\%$ . It can be further observed that the whole domain underwent plastic deformations after the application of the dead weight loading. The initial coefficient of lateral earth pressure for the non-cohesive sand could be computed from the ratio between the horizontal and vertical normal stresses,  $K = \sigma_{xx}/\sigma_{zz}$ , and varied between  $K = 0.25$  and  $K = 0.36$  going from the bottom to the top along the left (or right) boundary of the computational domain. In accordance with the range defined by the initial and maximum friction angles of the sand material,  $29^\circ \leq \phi \leq 40^\circ$ , this means that the sand along the left (or right) domain boundary experienced a horizontal stress state that approached the condition of active lateral earth pressure, as characterized by  $K = (1 - \sin\phi)/(1 + \sin\phi)$  (Verruijt & van Baars, 2007). In contrast, right next to the sewer pipe the vertical stress generated by the dead weight loading was considerably smaller than the horizontal stress, in correspondence with  $K = 3.29$ , which was caused by a local arching of the sand material located along the upper half of the sewer pipe.

The application of a groundwater flux of  $10^{-6}$  m/s (typical of *in-situ* conditions) at  $t = 0$  at the left boundary of the computational domain initiated a groundwater flow from the left to the right domain boundary. Due to the relatively large permeability of the sand material, at sufficient distance below the sewer pipe the groundwater flow within a few minutes of time reached an almost uniform steady-state profile in the horizontal direction, whereby the flux value was equal, or close to, the applied boundary flux  $\|\mathbf{q}_{fm}\| = 10^{-6}$  m/s. and the spatial pattern of  $\mathbf{q}_{fm}$  had become virtually symmetric with respect to



the vertical centreline of the FEM model. The time evolution of the erosion profile developing under the groundwater flow is sketched in [figure 5.18](#), by plotting the erosion degradation parameter  $D_{er}$  with  $0 \leq D_{er} \leq 1$ , at three different time instants, namely 7 years ([Figure 5.18a](#)), 13 years ([Figure 5.18b](#)) and 20 years ([Figure 5.18c](#)). The erosion profile started to grow at the bottom of the sewer pipe, and subsequently spread in a more or less horizontal direction towards the left and right domain boundaries, thereby creating a soil piping profile. Note that the green colour in the contour plot designates the area in which the erosion degradation parameter has reached the prescribed, maximum value for *suffusion* erosion,  $D_{er} = D_{er}^{max} = 0.5$ , and that the characteristic time scale associated with the development of the erosion profile is much larger than that of the process of ground water flow, that is, in the order of tens of years.



**Figure 5.18** Time evolution of the erosion profile (soil piping) under natural groundwater flow (first case study), as characterized by the spatial development of the erosion degradation parameter  $D_{er}$  after (a) 7 years, (b) 13 years and (c) 20 years, whereby  $D_{er}^{max} = 0.5$  (as representative of suffusion). The figure has been reprinted from [Schepherboer et al. \(2022\)](#).



The groundwater flux profiles after 7, 13 and 20 years are depicted in Figure 5.19 a, b and c, respectively, using the Euclidian norm of the flux,  $\|\mathbf{q}_{fm}\|$ , as the contour plot variable. It can be confirmed that the area in which the groundwater flux  $\|\mathbf{q}_{fm}\|$  is larger than the critical threshold value of  $q_{fm,cr} = 10^{-6}$  m/s (below which erosion does not occur) indeed corresponded to the geometry of the erosion profile shown in Figure 5.18. Further, the groundwater flux appeared to be maximal directly below the pipe, whereby the flux value increased when erosion developed, as caused by an increase in soil permeability.

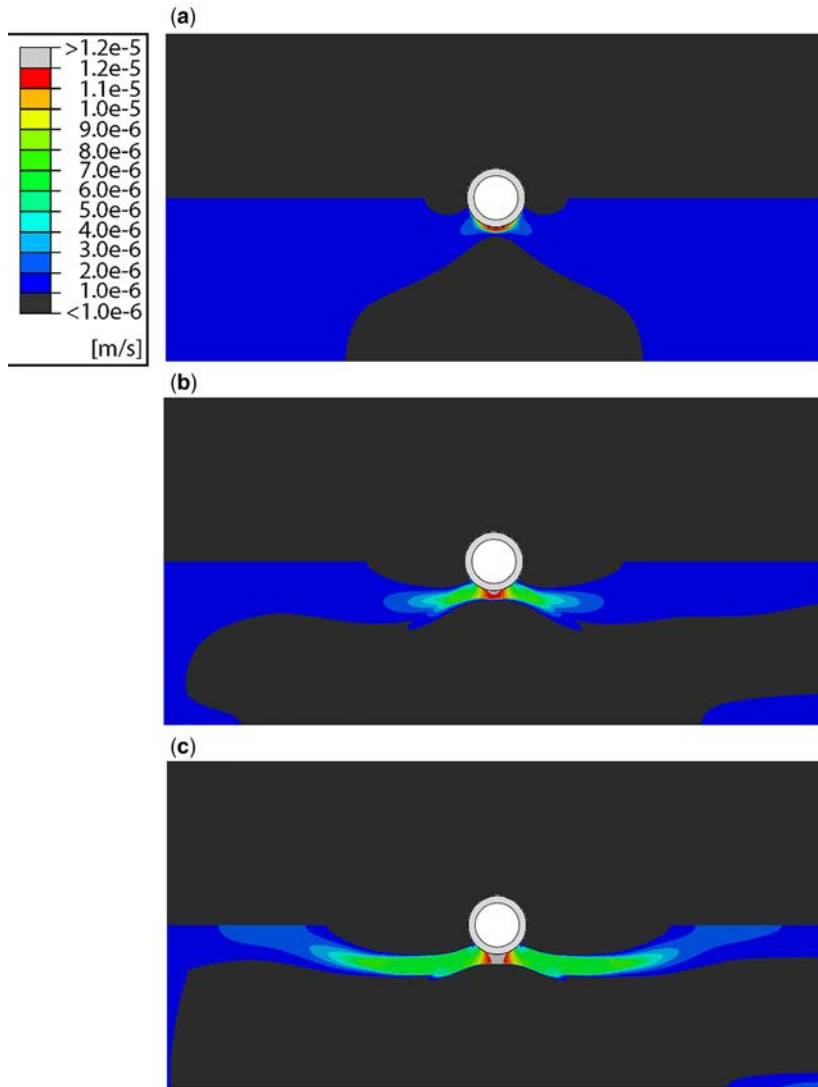


**Figure 5.19** Time evolution of the porewater velocity field under natural groundwater flow (first case study), as characterized by the spatial evolution of the norm of the flux  $\|\mathbf{q}_{fm}\|$  (in m/s) after (a) 7 years, (b) 13 years and (c) 20 years; the black colour indicates the area within which the value of  $\|\mathbf{q}_{fm}\|$  is lower than the critical threshold value  $q_{fm,cr} = 10^{-6}$  m/s for erosion. The figure has been reprinted from Schepers *et al.* (2022).

Figure 5.20 depicts the contour plot with the deviatoric plastic deformations, as evaluated after the application of the dead weight loading and an erosion process of 20 years. For clarity, in the contour plot the same scale division is used as for the deviatoric plastic deformations generated after the application of only the dead weight loading, see Figure 5.17b. In comparison with the deviatoric plastic deformations generated after the dead weight loading, left and right below the pipe the erosion process has led to a maximal increase in plastic strain of about a factor of two, in correspondence with a value of  $\bar{\gamma}^p = 0.74\%$ .

The evolution of the surface displacement, measured above the centre of the sewer pipe, is depicted in Figure 5.21. In order to clearly identify the displacement contribution caused by plastic deformations, the surface response is compared to that from a simulation in which erosion takes place on a fully elastic soil material. The elastic soil model was obtained from the elasto-plastic formulation by setting the yield strength artificially high. Figure 5.21 illustrates that for an elasto-plastic sand material the surface displacement monotonically increases with the development of erosion, whereby the value reached after 20 years equals 0.60 mm. The response for an elastic soil material shows a similar trend, whereby the deformation reached after 20 years is 25% less, that is, 0.45 mm. Since the surface displacements remained rather small, the practical suitability of using these as a monitoring parameter for the detection of a suffusion type of erosion under natural groundwater flow appears to be limited. This conclusion aligns with other scientific studies that report that soil pipes are only observable at the soil surface when a pipe roof collapses; accordingly, they are considered ‘apparently inactive’ over a long period of time, until clear surface evidence appears (Bernatek, 2015; Bernatek-Jakiel & Poesen, 2018; Verachtert *et al.*, 2011).

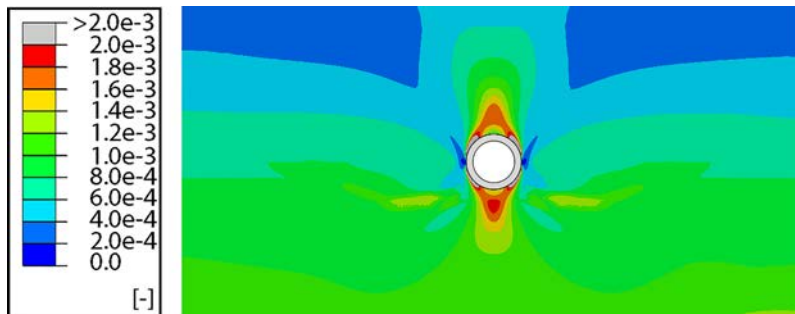


Figure 5.20 Spatial variation of the deviatoric plastic strain invariant  $\bar{\gamma}^p$  after the application of the dead weight loading and an erosion process of 20 years under natural groundwater flow (first case study). The figure has been reprinted from Schepers *et al.* (2022).

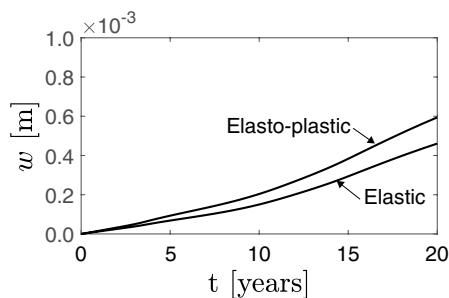
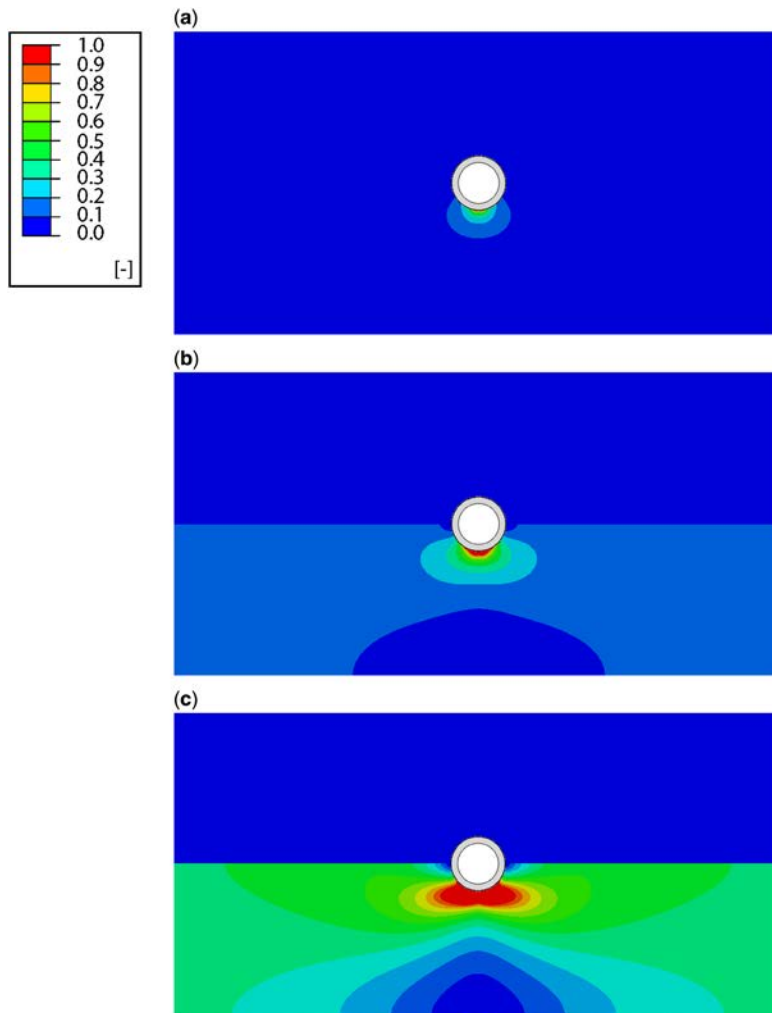


Figure 5.21 Time evolution of the vertical displacement  $w$  (in mm) of the ground surface – measured above the centre of the sewer pipe – under natural groundwater flow (first case study) for (i) an elasto-plastic sand material and (ii) an elastic sand material. The figure has been reprinted from Schepers *et al.* (2022).

#### 5.6.4 Void formation due to strong groundwater flow near a defect sewer system

Like the process discussed in the previous section, the FEM analysis of soil erosion near the defect sewer pipe started with the application of the dead weight loading of the soil structure and the sewer pipe. The atmospheric pressure applied at  $t = 0$  as a boundary condition across the gap width at the bottom of the sewer pipe initiated a relatively strong groundwater flow into the sewer pipe. The erosion profile caused by this flow profile is depicted in Figure 5.22 at three different moments in time, namely 47 days (Figure 5.22a), 93 days (Figure 5.22b) and 140 days (Figure 5.22c). It can be seen from the contour plot variable  $D_{er}$  that the erosion indeed started near the location of the gap, and subsequently extended along the bottom part of the pipe in a downward direction. At 140 days the erosion below the pipe had become quite severe and had induced a void with a depth of approximately half of the pipe diameter



**Figure 5.22** Time evolution of the erosion profile (void formation) under strong groundwater flow near a defect sewer pipe (second case study), as characterized by the spatial development of the erosion degradation parameter  $D_{er}$  after (a) 47 days, (b) 93 days and (c) 140 days, whereby  $D_{er}^{\max} = 0.93$  (as representative of suffosion). The figure has been reprinted from [Scheperboer et al. \(2022\)](#).

(red colour) within which the erosion degradation parameter was maximal,  $D_{er} = D_{er}^{max} = 0.93$ . Hence, the erosion void is of the *suffosion* type, with its volume for 95% filled by ground water, and only for 5% by remaining soil particles. It can be further observed that almost the complete saturated sand layer at this stage had undergone some degree of erosion, in agreement with an erosion degradation parameter larger than zero and below the maximum value,  $0 < D_{er} < 0.93$ . It is further interesting to observe that the erosion profile developed much faster than in the first case study on soil piping, see Figure 5.18, which clearly demonstrates that the characteristic time scale of an erosion process very much depends on the type of problem and the corresponding hygro-mechanical conditions.

The groundwater flow patterns after 47 days, 93 days and 140 days are illustrated in Figure 5.23a, b and c, respectively, and show to be in agreement with the erosion profiles in the area in which the

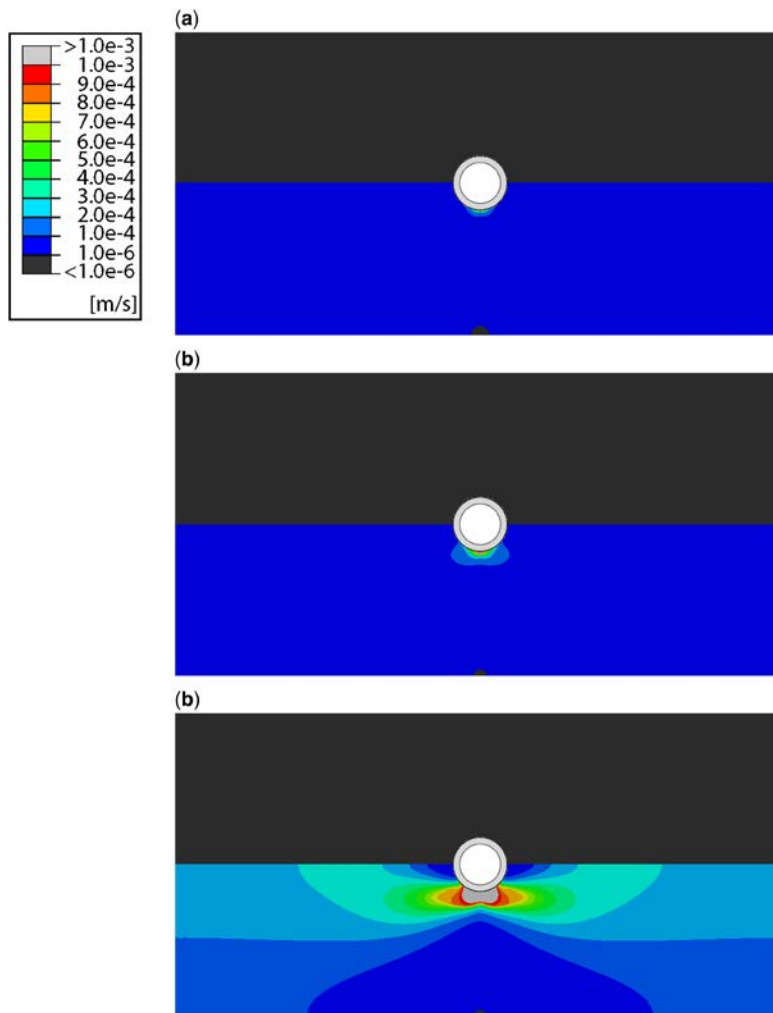


**Figure 5.23** Time evolution of the porewater velocity field under a strong groundwater flow near a defect sewer pipe (second case study), as characterized by the spatial evolution of the norm of the flux  $\|\mathbf{q}_{fm}\|$  (in m/s) after (a) 47 days, (b) 93 days and (c) 140 days; the black colour indicates the area within which the value of  $\|\mathbf{q}_{fm}\|$  is lower than the critical threshold value  $q_{fm,cr} = 10^{-6}$  m/s for erosion. The figure has been reprinted from Schepboer *et al.* (2022).

flux threshold value of  $q_{fm,cr} = 10^{-6}$  m/s was exceeded. Within the erosion void the permeability of the remaining 'soil structure' was maximal and corresponded to a value of  $k = 2.0 \times 10^{-2}$  m/s. This value is 200 times larger than the initial permeability  $k_0 = 10^{-4}$  m/s of the sand material.

The deviatoric plastic deformations generated under the dead weight loading and the subsequent erosion process are illustrated in Figure 5.24 representing the passage of 140 days. In comparison with the deviatoric plastic deformations generated under only the dead weight loading, see Figure 5.23b, the deviatoric plastic deformation in the soil material directly left and right of the sewer pipe had substantially increased by more than a factor of 10 to a value of  $\bar{\gamma}^p = 5.4\%$ . Furthermore, at the bottom-left and bottom-right of the pipe the deviatoric plastic strain had reached a maximum value of  $\bar{\gamma}^p = 14.4\%$ . Obviously, this strong, local increase in deviatoric plastic deformation was caused by the stress redistribution that balanced the local loss of soil resistance in the suffusion erosion void below the sewer pipe; the specific local shear failure zones in the soil next to the sewer pipe are indicated in Figure 5.24 by the grey hatched areas.

Figure 5.25 depicts the vertical surface displacement as a function of time for both an elasto-plastic and an elastic sand material. The surface displacement initially grew moderately, but after  $\sim 100$  days started to increase rapidly due to the formation of the erosion void below the sewer pipe. The surface displacement after 140 days equalled 5.8 and 4.4 mm in the case of the elasto-plastic soil model and

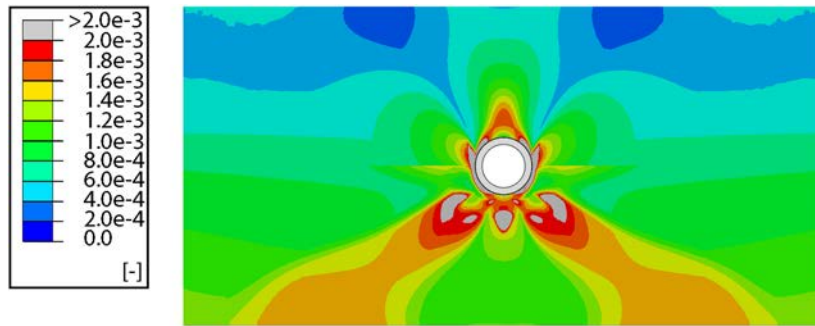


**Figure 5.24** Spatial variation of the deviatoric plastic strain invariant  $\bar{\gamma}^p$  after the application of the dead weight loading and an erosion process of 140 days under a strong groundwater flow near a defect sewer pipe (second case study). The figure has been reprinted from Schepërboer *et al.* (2022).

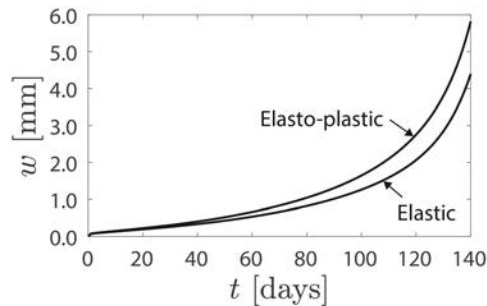


**Figure 5.25** Time evolution of the vertical displacement  $w$  (in mm) of the ground surface – measured above the centre of the sewer pipe – under a strong groundwater flow near a defect sewer pipe (second case study) for (i) an elasto-plastic sand material and (ii) an elastic sand material. The figure has been reprinted from Schepërboer *et al.* (2022).

the elastic soil model, respectively. The relative difference between these displacements is substantial, that is, 32%, which indicates the importance of accurately modelling the constitutive behaviour of the soil in erosion simulations by means of an elasto-plastic model. Also, it is interesting to notice that the ground surface deflections in [Figure 5.25](#) are much larger than those generated under soil piping erosion, see [Figure 5.21](#).

Additional simulations not presented here have shown that a decrease of the gap width in the sewer pipe by a factor of 40 to a value of 0.5 mm led to a similar surface deflection evolution as illustrated in [Figure 5.25](#). Essentially, the decrease in gap width reduced the flow area at the bottom of the sewer pipe, which was accompanied by an increase in the local flow velocity, such that, as a net effect, the erosion void developed in a more or less comparable fashion. Nevertheless, the value of the surface deflection at 140 days was about 11% smaller, namely 5.2 and 3.9 mm in the case of an elasto-plastic and an elastic sand material, respectively. Note hereby that the assumption of a small gap width of 0.5 mm ignored the fact that the relatively large particles in the sand material cannot flow into the pipe, so that the real surface deflections for this case would be smaller.

Finally, it needs to be emphasized that the remaining stability of the suffosion type of erosion void illustrated in [Figure 5.14c](#) is limited, as its bearing capacity was (virtually) generated by the fluidic mixture inside; hence, as soon as the groundwater table lowered and the fluidic mixture left the erosion void, the sewer pipe drops down into the erosion void, whereby the overlying soil structure is likely to collapse into a sinkhole. Accordingly, the abrupt increase in surface settlement registered after 100 days can be considered as a critical warning for catastrophic failure. Since the subsequent surface displacements are in the order of several millimetres, in practice it should be possible to detect these changes with satellite radar interferometry ([Chang & Hanssen, 2014](#); [Malinowska et al., 2019](#)), which may help to prevent the eventual collapse into a sinkhole.

The above numerical analyses on soil piping and erosion void formation illustrate that the numerical model developed by [Scheperboer et al. \(2022\)](#) realistically predicts the size, location and characteristic time scale of the generated erosion profiles and the deformations of the surrounding soil structure. Hence, the erosion profiles computed by the model may be used as input for a detailed analysis of the local, residual bearing capacity and stress redistribution of buried concrete pipe systems. Additionally, the modelling results may support the early detection of *in situ* subsurface erosion phenomena from ground surface deformations recorded with satellite radar interferometry. The analyses further show that the characteristic time scales of the erosion process and the generated ground surface deflections strongly depend on the geometry and features of the problem, as reflected by the specific hydro-mechanical conditions.

## 5.7 STRUCTURAL FAILURE OF CONCRETE SEWER PIPES

### 5.7.1 Introduction

In [Dirksen et al. \(2013a\)](#) it is shown that the accuracy and reliability of visual inspection data may be low, with 25% of the damage not being detected. In addition, in [Stanic et al. \(2013\)](#) and [Stanic et al. \(2017\)](#) it is demonstrated that no evident correlation exists between visual inspection data and the material properties obtained from core samples taken from the sewer pipe. Moreover, an accurate database on the actual condition of sewer systems is lacking ([Dirksen et al., 2013a](#); [Wirahadikusumah et al., 2001](#); [van Riel et al., 2016](#)), and the effects of biochemical deterioration and ageing on the structural performance of a sewer pipe are yet not well understood, and therefore difficult to take into account in the assessment procedure ([Grengg et al., 2018](#); [Monteny et al., 2000](#); [O'Connell et al., 2010](#); [Stanic et al., 2017](#)).

For the development of a good understanding of the failure behaviour of concrete pipe systems, over the past decades various full-scale field studies ([Erdogmus & Tadros, 2009](#); [Hill et al., 1999](#); [McGrath et al., 1999](#); [Nehdi et al., 2016](#)) and laboratory studies ([Brachman et al., 2001](#); [MacDougall et al., 2016](#); [Peter et al., 2018](#); [Stanic et al., 2017](#); [Trautmann & O'Rourke, 1985](#); [Younis et al., 2020](#); [Zoladz et al.,](#)



1996) have been performed, among which geocentrifuge tests to account for specific interactions with the surrounding soil structure (Rakitin & Xu, 2014; Schofield, 1980; Xu & Shen, 2020). Accordingly, for diverse pipe geometries the bearing strength, deformation behaviour and crack patterns were measured under representative loading and boundary conditions, thereby identifying aspects such as the susceptibility to joint failure and leakage, the most unfavourable loading conditions, and the role of local soil collapse. The experimental failure behaviour of concrete pipes has been complemented and validated by numerical simulations (Kang *et al.*, 2007; Meguid & Dang, 2009; Tan, 2007; Xu *et al.*, 2017), and translated to practical recommendations and design procedures.

In the present section, this line of research is continued by presenting a comprehensive, systematic experimental–numerical study of the structural failure behaviour of unreinforced round and egg-shaped concrete sewer pipes. The main purpose of the study is to obtain thorough insight into the load bearing capacity and failure mechanisms of concrete sewer pipes, and to understand the influence by degradation effects typical of soil erosion, changes in lateral earth pressure, biochemical processes, and ageing. The study considers sewer pipe types most commonly used in the Netherlands, which are (i) two different round pipes with an inner diameter of 400 and 500 mm, respectively and (ii) an egg-shaped pipe with a horizontal inner diameter of 400 mm and a vertical inner diameter of 600 mm. The concrete sewer pipes are subjected to biaxial loading conditions in an experimental set-up customized from the test specifications provided in Stanic *et al.* (2017), whereby the horizontal pressure loading is set equal to 1/3 times the vertical pressure loading. This loading condition is considered to be representative of a concrete sewer pipe embedded in a well-graded sandy gravel and subjected to neutral horizontal earth pressure. The elasto-fracture properties of the concrete are determined from material tests performed on small samples taken from the sewer pipes. The experimental failure responses of the round and egg-shaped sewer pipes are validated by dedicated FEM analyses. Subsequently, a parameter variation study is carried out using the FEM of the round sewer pipe with an inner diameter of 400 mm. Accordingly, the sensitivity of the overall failure response of the sewer pipe to several parameters is investigated, which are the load contact area (to mimic the effect of soil erosion), the ratio between the applied horizontal and vertical loadings (to analyze the effect by a change in lateral earth pressure), the wall thickness (to simulate the effect of biochemical degradation), and the tensile strength, mode I toughness and Young's modulus of the concrete (to model the effect of biochemical degradation and/or ageing). The outcome of the experimental–numerical study provides a scientific basis and practical guidelines for municipalities in their decision making process regarding the maintenance and replacement of concrete sewer pipe systems. The content of this section is a summary of the work presented in Scheperboer *et al.* (2021).

## 5.7.2 Experimental programme

The load bearing capacity and failure mechanisms of new concrete sewer pipes are assessed by means of full-scale experiments. The test specimens, experimental set-up, test procedure and measuring devices are specified below.

### 5.7.2.1 Test specimens

In the experimental programme, three different unreinforced concrete sewer pipes were considered, namely dry-cast round pipes with an inner diameter of 400 and 500 mm, labelled as R400 and R500, respectively, and dry-cast egg-shaped pipes with a horizontal and vertical inner diameter of respectively 400 and 600 mm, labelled as E400/600. The sewer pipes were manufactured by the production companies Kijlstra and De Hamer located in the Netherlands. The strength and stiffness parameters of the specific concrete used were determined by material tests (Scheperboer *et al.*, 2021). The pipes were 1–4 years old and had not been exposed to in-situ conditions. A number of specimens with a manageable length of  $\sim$  one metre were sawn from the sewer pipes, whereby the socket and spigot were removed. The specimens were kept moist prior to testing in order to mimic in-situ hydrological conditions. The internal and external surfaces of the pipe specimens were inspected visually to

ensure the specimens did not have noticeable defects. For each of the three sewer pipe types the test repeatability was explored by testing six similar pipe specimens. Both the outer and inner specimen height and width and the wall thickness were measured (Scheperboer *et al.*, 2021).

### 5.7.2.2 Experimental set-up

An overview of the experimental set-up is shown in Figure 5.26. The test frame was composed of steel HEB 300 members, which are sufficiently stiff to marginalize the frame deformations generated during the testing procedure. The horizontal loads were applied by four jacks – two at each side – positioned at the half height of the test specimen, and the vertical load was applied at the top of the test specimen by means of three jacks. The jacks were equally spaced along the specimen length. The ratio between the horizontal and vertical loads was set equal to 1/3. This ratio is representative of a sewer pipe embedded in a well-compacted sandy gravel with an ultimate friction angle  $f$  in the range of  $40^\circ$ – $45^\circ$ , for which the coefficient of neutral horizontal earth pressure, in accordance with Jaky's empirical formula,  $K_0 = 1 - \sin(f)$ , is  $\sim 1/3$  (Verruijt & van Baars, 2007). During the testing the specimen behaviour was recorded by means of two cameras placed at the front side of the specimen. At the top and the two lateral sides of the test specimen, the loading was transferred to the curved outer surface of the specimen by placing a steel member, a steel plate, several plywood boards, an air cushion and a rubber foil between the jacks and the specimen surface. The steel member and plate were used to spread the applied load evenly across the specimen surface, the plywood boards filled up some space between the steel plate and the test specimen, and the rubber foil served to protect the air cushions from mechanical damage. Once filled with air, the air cushions were observed to accurately follow the curved outer surface of the pipe specimen. For each sewer pipe type, the average contact width of the air cushions was measured from photographs taken prior to failure (Scheperboer *et al.*, 2021).

Throughout the test procedure the relative change in loading contact area turned out to be minor; in specific, the change was less than 5% after the air cushions had been sealed, which allows the loading contact area to be taken as constant. For the round sewer pipes the support at the specimen bottom consisted of an air cushion with a rubber foil, followed by plywood boards, a steel plate and a steel member. Since the bottom of egg-shaped pipes is flat, for these pipes an adequate contact at the support was simply established with a softboard plate with a thickness of 10 mm, instead of an air cushion.

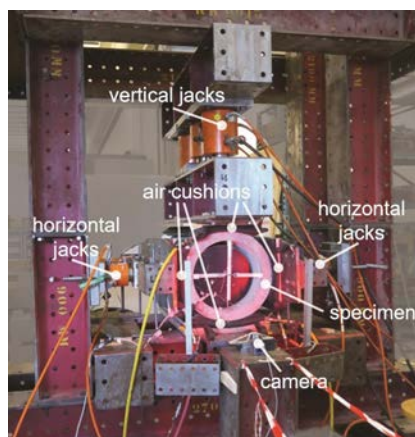


**Figure 5.26** Full-scale experimental set-up for a sewer pipe subjected to biaxial loading conditions. The figure has been reprinted from Scheperboer *et al.* (2021).

### 5.7.2.3 Test procedure

The test protocol adopted for safely and accurately performing the mechanical tests on the sewer pipes is as follows. Firstly, the air cushions at the lateral sides of the pipe were inflated in order to ensure adequate contact between the pipe and the horizontal jacks and to prevent the round pipes from rotating about their length axis. After the cushions had generated a horizontal load of 3 kN, the air cushions at the top and bottom surfaces of the pipe were inflated up to a vertical load of 9 kN, in correspondence with the horizontal to vertical loading ratio of 1/3. Subsequently, all four air cushions were simultaneously inflated further until the horizontal and vertical loads reached the values of 20 and 60 kN, respectively, after which the air cushions were sealed. The inflation of the air cushions was controlled in a manual fashion, whereby the selected horizontal to vertical loading ratio of 1/3 was maintained as close as possible. After the sealing of the air cushions, the jack system was activated and the horizontal and vertical loads were increased up to failure of the pipe specimen. The mechanical testing was performed in a quasi-static, load-controlled fashion, using vertical loading speeds of 6 and 10 kN/min for respectively the round pipe specimens and the egg-shaped pipe specimens. Correspondingly, the test duration was  $\sim$  30–45 min for the round pipes and 45–60 min for the egg-shaped pipes.

### 5.7.2.4 Measuring devices

The mechanical response was determined by measuring the applied load and the generated deformation at regular time intervals of 1 s. The horizontal and vertical loads were monitored by means of HBM 500 bar pressure sensors that measure the oil pressure inside the tubes activating the jacks. The displacements in horizontal and vertical directions were measured at the front and back sides of the sewer pipe using Solartron SM3 linear variable displacement transducers (LVDTs). The local strains were monitored employing Tokyo Sokki Kenkyujo PL-60–11 strain gauges (SGs). At the top, bottom, left and right sides of the sewer pipe, strain gauges were placed on the inner surface of the pipe, both near the front side and back side. In addition, strain gauges were placed on the front and back surfaces of the sewer pipe, at the top, bottom, left and right sides, at a distance of 10 mm from the outer pipe circumference. The denotations 'left side' and 'right side' hereby relate to a viewpoint taken at the front side of the pipe specimen, so that for the front and back sides the adjectives 'left' and 'right' refer to the same specimen side. Three additional strain gauges were placed at equal mutual distance along the length of the sewer pipe. An HBM X60 two-component adhesive was used to glue the strain gauges to the sewer pipe surfaces. At regular time intervals, photographs were taken of the sewer pipe front surface, which were correlated to the load and deformation recorded at the front side of the specimen.

### 5.7.3 Numerical model

The experimental results of the concrete sewer pipes are validated by means of 2D plane-strain FEM analyses. The numerical simulations are carried out with the FEM, using the commercial software package ABAQUS Standard. The FEM models are based on 2D plane-strain continuum elements that simulate the elastic (bulk) behaviour of the concrete sewer pipe. The fracture behaviour of concrete is simulated with interface elements endowed with the mixed-mode damage model presented in [Cid Alfaro \*et al.\* \(2009\)](#), which is implemented in ABAQUS as a user-supplied subroutine (i.e., a UMAT). The essential input parameters of this model are the ultimate fracture strength  $t^u$  and the toughness  $G_c$  of the concrete material under pure modes I and II loading conditions. The model further contains parameters that (i) allow for including rate-dependent fracture effects and (ii) assist in regularizing fracture responses with complex trajectories towards a physically realistic result. For more details on the formulation and the numerical discretization of this model, the reader is referred to [Cid Alfaro \*et al.\* \(2009\)](#).

In accordance with the modelling strategy originally proposed in [Xu and Needleman \(1994\)](#), the interface elements are located between all continuum elements, so that the mechanisms of crack bifurcation, crack coalescence and crack branching at arbitrary locations and in arbitrary directions are simulated in an automatic fashion. The accuracy and efficiency of the above approach have been

successfully demonstrated in previous fracture studies for a variety of materials. The set of equilibrium equations is solved through an incremental–iterative update procedure, based on an implicit Euler backward scheme combined with a full Newton–Raphson iterative update strategy. The arc-length method is adopted to account for a possible softening and snap-back behaviour in the quasi-static, load-controlled simulations (Riks, 1979).

The geometry, boundary conditions and FEM discretizations of the round and egg-shaped sewer pipes are illustrated in Figure 5.27a and b, respectively. The geometries of the modelled sewer pipes are in close agreement with those used in the experiments. The inner diameters of the modelled geometries are 400 and 500 mm for the round R400 and R500 pipes, and 400 mm/600 mm for the E400/600 egg-shaped sewer pipe, respectively. The wall thickness of the pipes is taken as the average value measured in the experiments, and equals 62 and 72 mm for, respectively, the R400 and R500 pipes, and 70 mm for the upper part of the E400/600 pipe, see Table 5.1. The loads are introduced on the sewer pipe by means of horizontal and vertical surface pressures  $\sigma/3$  and  $\sigma$ , respectively, in correspondence with the horizontal to vertical loading ratio of 1/3 used in the experiments. The projected contact width  $l_c$  along which the surface pressure is applied equals 250, 280 and 290 mm, for the R400, R500 and E400/600 pipe types, respectively, which is in close correspondence with the widths of the contact zones applied in the testing procedure, see Table 5.1. Accordingly, the total vertical load used in the presentation of the computational results is  $F_v = \sigma l_c L$ , where  $L = 1$  m equals the length of the sewer pipe specimen. The round pipes are restrained against rigid body motions by three roller supports, see Figure 5.27, which are located at the side of the sewer pipe wall that is loaded in compression. The soft board plate used for vertically supporting the egg-shaped pipe has a thickness of 10 mm. As sketched in Figure 5.27b, the soft board is supported in the vertical and horizontal directions by roller supports, and is coherently connected to the pipe specimen. The sewer pipe geometries are discretized by 3-node iso-parametric plane-strain elements equipped with a 1-point Gauss quadrature, whereby the small-strain assumption is adopted. The cracking paths defining the failure response of the sewer pipe are modelled via 4-node interface elements equipped with a 2-point Gauss quadrature. As mentioned above, the interface elements are located between all triangular continuum elements, which allows crack initiation and propagation to be determined by the actual geometry and boundary conditions of the sewer pipe. The detailed cracking paths characterizing the failure response of the sewer pipes are unknown a priori; however, for warranting accurate numerical results, based on the experimental results the areas within which cracks are expected to

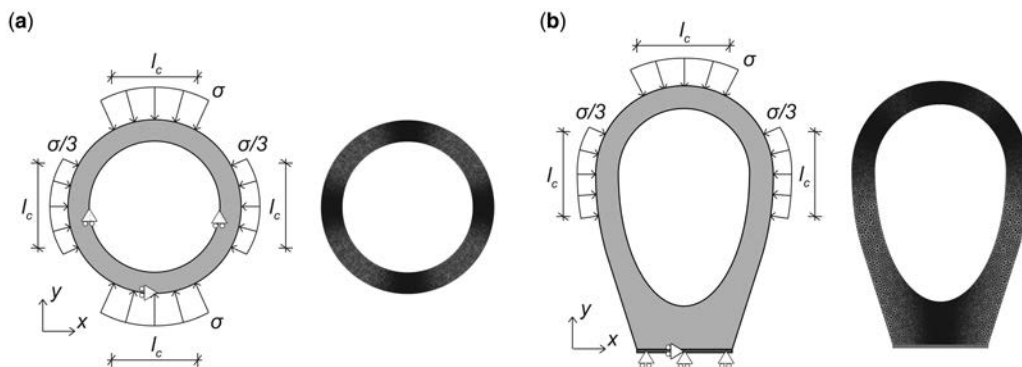


**Figure 5.27** Applied biaxial loading and boundary conditions (left) and finite element discretization (right) for (a) a round sewer pipe, and (b) an egg-shaped sewer pipe. The horizontally and vertically projected contact width  $l_c$  along which the distributed normal loadings  $\sigma$  and  $\sigma/3$  are applied equals 250, 280 and 290 mm for the R400, R500 and E400/600 pipe type, respectively. The figure has been reprinted from Schepherboer *et al.* (2021).

emerge are discretized by a relatively fine FEM mesh. The specific number of continuum and interface elements used in the FEM models depends on the actual pipe geometry considered and varies between 34,000–55,000 continuum elements and 50,000–61,000 interface elements, see [Figure 5.27](#) for two examples. Although the spatial discretization of the modelled geometry in principle can have an effect on the location and direction of the cracking path, the FEM meshes used in the present study are sufficiently fine to marginalize this effect. It should be further emphasized that the mesh fineness is bounded by a maximum in order to avoid artificial response contributions related to the use of an elastic interface stiffness  $K$  in the traction separation law, see [Cid Alfaro \*et al.\* \(2010a\)](#) for a detailed discussion of this aspect. The set of equilibrium equations obtained for the FEM models is solved by using an incremental-iterative update approach, which is based on an implicit backward Euler scheme combined with a full Newton–Raphson iterative update procedure. The arc-length method is adopted to robustly simulate a possible snap-back or softening behaviour in the quasi-static, load-controlled simulations ([Riks, 1979](#)).

The Young's modulus  $E_c$  of the continuum elements describing the elastic behaviour of concrete was determined from uniaxial compression tests, in close conformity with the regulations from Eurocode NEN-EN 12390-13 ([European Committee for Standardization, 2013](#)). Accordingly, from each of the three sewer pipe types a total of 12–15 small samples were sawn, whereby the Young's moduli measured for the samples were averaged over the corresponding total number of samples ([Schepelhoer \*et al.\*, 2022](#)). The value of the Poisson's ratio  $\nu_c$  is taken from the Eurocode EN 1992-1-1 ([European Committee for Standardization, 2005](#)), in accordance with concrete strength class C50/60. The tensile strength  $t_t^u$ , and mode I toughness  $G_{I,c}$  used in the interface damage model were determined experimentally from three-point bending tests, with the specimen dimensions and loading procedure based on [Hordijk \(1991\)](#). Accordingly, from each of the three types of sewer pipes 18 concrete notched beam specimens were sawn, whereby the average values of the experimental sample strength and toughness listed were calibrated from dedicated FEM analyses that accurately mimic both the experimental fracture path and the load–displacement response of the beam specimens. The combined experimental–numerical calibration procedure applied here is similar to that recently performed for determining the tensile strength and toughness parameters of oak wood, as described in detail in [Luimes \*et al.\* \(2018\)](#). For simplicity, the shear strength  $t_2^u$ , of concrete is taken equal to the tensile strength  $t_t^u$ , and the mode II toughness  $G_{II,c}$  is set equal to two times the mode I toughness  $G_{I,c}$  ([Reinhardt & Xu, 2000](#)). The soft board plate supporting the E400/600 egg-shaped sewer pipe has a Young's modulus  $E_{sb} = 3.0 \text{ N/mm}^2$ , which is the average value measured from 8 uniaxial compression tests on soft board samples. Poisson's ratio  $\nu_{sb}$  of the soft board is set equal to 0.20 ([Moarcas & Irle, 1999](#)). In all simulations the elastic stiffness  $K$  of the interface damage model was prescribed to have a relatively high value, for which it was confirmed that the overall elastic response of the sewer pipe remained virtually unaffected by this parameter and was determined almost completely by the elastic properties of the surrounding continuum elements. In addition, the material parameters related to the rate-dependency of the kinetic law were chosen such that the fracture response closely approximates the rate-independent limit case. More details on these aspects can be found in previous numerical studies performed with the interface damage model ([Cid Alfaro \*et al.\*, 2009, 2010a, 2010b](#)).

## 5.7.4 Comparison of experimental and numerical results

### 5.7.4.1 Load–displacement response of round sewer pipes

[Figure 5.28a](#) and [b](#) illustrate the simulated load–displacement response (red line) of respectively the round pipes R400 and R500, together with the corresponding experimental responses (black lines). The vertical loading  $F_v$  is plotted against the net vertical displacement  $d_v$  in [Figure 5.28](#). The comparison related to the horizontal load–displacement response of the pipes is similar to that of the vertical response, and is therefore left out of consideration. It can be seen that the agreement between the numerical and experimental results generally is good. The initial elastic response of the sewer pipes is captured accurately by the FEM models, and the vertical peak load appears to be in good agreement



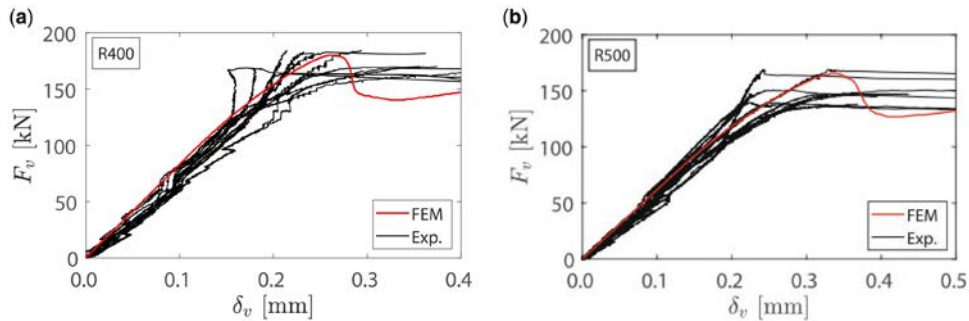


**Figure 5.28** Vertical load  $F_v$  versus vertical net displacement  $d_v$  of (a) the round R400 and (b) the round R500 sewer pipe, as obtained by experiments (black lines) and an FEM simulation (red line). The figure has been reprinted from [Scheperboer et al. \(2021\)](#).

with the corresponding experimental peak load. In specific, the numerical vertical peak loads of the R400 and R500 sewer pipes are 180.0 kN and 165.5 kN, which overestimate the average experimental peak loads by 5% and 11%, respectively. After passage of the peak load, the numerical response is characterized by an unstable softening branch, whereby the external load temporarily decreases with increasing displacement, until it reaches a residual value of about 0.8 times the peak load. The experimental response does not show a softening behaviour, due to the fact that the experiments were performed in a load-controlled fashion. Instead, the instability emerging after passing the peak load changed the experimental response from quasi-static to dynamic.

### 5.7.5 Local strain response of round sewer pipes

[Figure 5.29a](#) and [b](#) illustrate the experimental (black lines) and numerical (red line) load–strain responses at two specific locations along the inner diameter and near the outer diameter of the R400 pipe, that is, the bottom-inside and the right-outside locations. The correspondence between the experimental and numerical responses generally is good; both the initial linear elastic regime and the response towards the peak load are captured accurately. Since the load–strain responses of the R500 sewer pipe specimens with a larger diameter of 500 mm are comparable to those of the R400 specimens shown in [Figure 5.29](#), with a similar agreement between the experimental and numerical results, the discussion of these curves is omitted here.

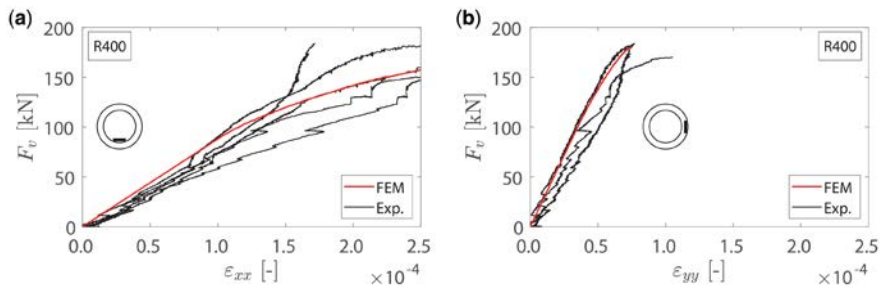


**Figure 5.29** Experimental (black lines) and FEM (red line) load–strain response for the round R400 sewer pipe. Vertical load  $F_v$  versus the normal strain  $\epsilon_{xx}$  or  $\epsilon_{yy}$  as measured at (a) the bottom-inside and (b) the right-outside locations. The corresponding location of the strain gauge is indicated in the inset of the figures. The figure has been reprinted from [Scheperboer et al. \(2021\)](#).



### 5.7.6 Fracture pattern of round sewer pipes

The contour plots in Figure 5.30 show the maximum principal stress in the R400 pipe at four consecutive stages (a)–(d) of the failure process, as indicated in the added load–displacement diagram. Since the macroscopic failure cracks develop in the post-peak regime, the deformation range in the load–displacement diagram needed to be chosen relatively large. For clarification, the deformations of the pipe geometry are magnified in the contour plots by a factor of 50. At stage (a) in the load–displacement diagram the sewer pipe reaches its load bearing capacity, whereby macroscopic failure

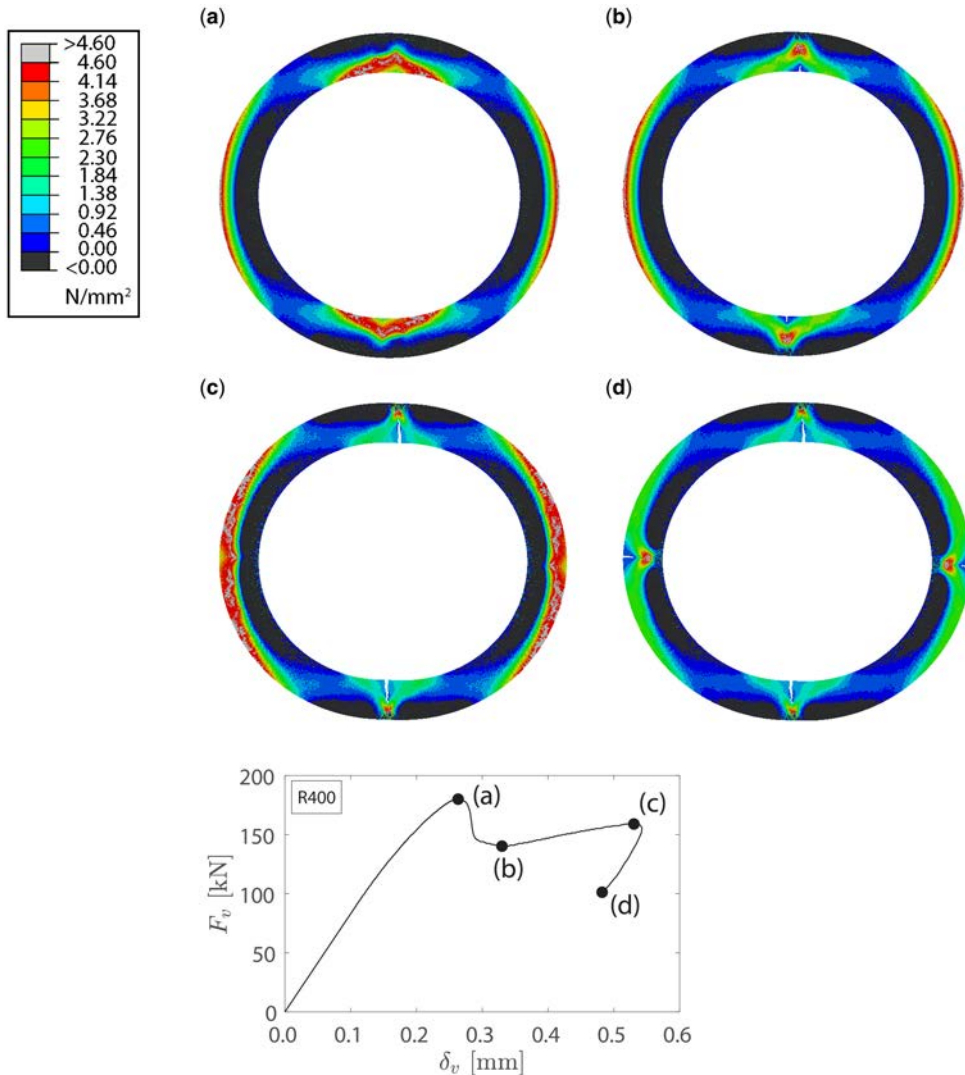


**Figure 5.30** Maximum principal stress at crack nucleation (a) and crack propagation (b)–(d) in the round R400 sewer pipe under the applied biaxial loading schematized in Figure 5.27. For clarification, the deformations of the pipe geometry are magnified in the contour plots by a factor of 50. The four failure states (a)–(d) are indicated in the corresponding load–displacement diagram. The figure has been reprinted from Schepboer *et al.* (2021).

cracks nucleate at the inner top and bottom parts of the sewer pipe. As can be observed from the contour plot in Figure 5.30a, at the locations of these two cracks the maximum principal stress has reached the material tensile strength of 4.6 N/mm<sup>2</sup> (depicted in red). When the two cracks start to propagate, the micro-cracks appearing in the vicinity of these cracks start to close, by which the crack pattern becomes more localized, see Figure 5.30b. Simultaneously, the maximal external load defining the crack nucleation stage drops in magnitude by approximately 20% in accordance with a structural softening behaviour, after which the sewer pipe reaches its residual strength, indicated by stage (b) in the load–displacement diagram. Upon further growth of these cracks, the external load slightly increases with deformation, until reaching stage (c) at which two additional failure cracks nucleate at the outer left and right sides of the sewer pipe, see Figure 5.30c. The development of these failure cracks is illustrated in Figure 5.30d, and causes that the external vertical load substantially decreases under a decrease in the net vertical displacement, in correspondence with reaching stage (d) in the load–displacement diagram. The failure branch from stage (c) to stage (d) commonly is referred to as a ‘snap-back behaviour’, and preludes catastrophic failure of the sewer pipe. The numerical failure pattern displayed in Figure 5.30d appeared to be in close agreement with the experimental failure pattern (Schepërboer *et al.*, 2021). In addition, the crack sequence presented in Figure 5.30 is in accordance with the experimental and numerical values for the local strains, with the largest tensile strain appearing at the bottom-inside (and top-inside) of the sewer pipe, and the smaller tensile strain emerging at its right-outside (and left-outside) (Schepërboer *et al.*, 2021).

#### 5.7.6.1 Load–displacement response of egg-shaped sewer pipe

In Figure 5.31 the experimental load–displacement response (black lines) of the egg-shaped sewer pipes is compared against the numerical response (red line), by depicting the vertical load  $F_v$  versus the vertical net displacement  $\delta_v$ . The FEM response reflects the average of the experimental responses at the front and back sides of the pipe quite well; the vertical ultimate load  $F_{v,max}$  following from the FEM simulations equals 363.7 kN, and is 9% larger than the average value of 334.3 kN obtained from the experiments. The local strain response Figure 5.32X.7 shows the applied vertical load  $F_v$  as a function of the local normal strains  $e_{xx}$  or  $e_{yy}$ , for two specific locations along the inner circumference and near the outer circumference of the E400/600 pipe, that is, the bottom-inside and the right-outside locations. The experimental and numerical strain responses are similar, especially along the initial elastic branch of the load–strain diagrams. It can be observed that the response obtained by the plane-strain FEM analysis approximately follows the average of the experimental responses.

The contour plots in Figure 5.33 illustrate the maximum principal stress in the egg-shaped pipe at four successive stages (a)–(d) during the failure process, which are indicated in the added load–displacement diagram. Observe from Figure 5.33a that the first failure crack nucleates at the inner

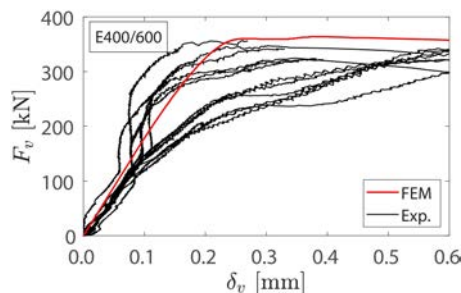


**Figure 5.31** Vertical load  $F_v$  versus vertical net displacement  $\delta_v$  of the egg-shaped E400/600 sewer pipe, as obtained by experiments (black lines) and an FEM simulation (red line). The figure has been reprinted from Schepërboer *et al.* (2021).

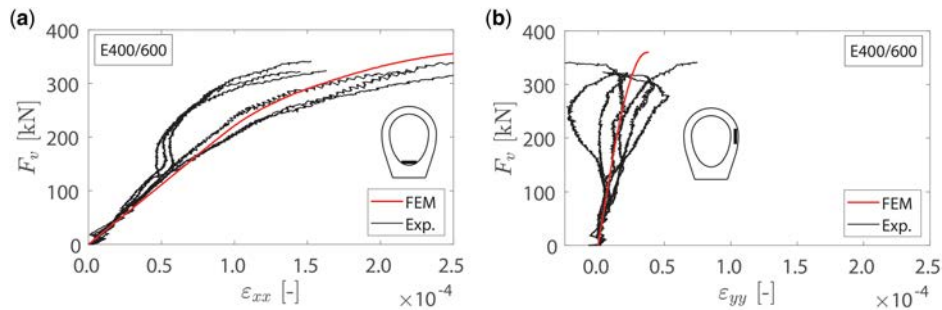


**Figure 5.32** Experimental (black lines) and FEM (red line) load–strain response for egg-shaped E400/600 sewer pipe specimens. Vertical load  $F_v$  versus the normal strain  $e_{xx}$  or  $e_{yy}$  as measured at (a) the bottom-inside and (b) the right-outside locations. The corresponding location of the strain gauge is indicated in the inset of the figures. The figure has been reprinted from [Schepers et al. \(2021\)](#).

top of the sewer pipe, in correspondence with stage (a) in the load–displacement diagram. When the vertical load is slightly increased towards the ultimate value  $F_{v,max}$  at stage (b), this failure crack grows and a second failure crack nucleates at the inner bottom of the sewer pipe, see [Figure 5.33b](#). As indicated in [Figure 5.33c](#), both failure cracks further develop under the appearance of a minor structural softening behaviour from stage (b) to stage (c). Ongoing structural softening towards stage (d) eventually leads to the nucleation and growth of two additional failure cracks, located at the outer top-left and top-right sides of the pipe, see [Figure 5.33d](#), after which the sewer pipe loses its mechanical strength and fails. As for the round pipe, for the egg-shaped pipe the locations of the four numerical failure cracks illustrated in [Figure 5.33d](#) are in excellent agreement with those observed experimentally ([Schepers et al., 2021](#)). In addition, the crack sequence as presented in [Figure 5.33](#) is confirmed by the experimental results for the local strains, with the highest tensile strain emerging at the top-inside of the pipe, followed by the tensile strain at the bottom-inside, and subsequently the tensile strain at the right-outside (and left-outside) of the pipe.

### 5.7.7 Parameter variation study for the R400 sewer pipe

The good agreement between the experimental and numerical results allows the FEM models to be used for studying the influence of various geometrical and material parameters on the failure response of a sewer pipe. Accordingly, this section treats a parameter variation study for the round R400 sewer pipe, whereby the failure response of the pipe is computed through dedicated FEM simulations that successively consider the influence of (i) the load contact area, (ii) the horizontal to vertical load ratio, (iii) the wall thickness of the sewer pipe, (iv) the tensile strength of concrete, (v) the toughness of concrete and (vi) the Young's modulus of concrete. The load contact area has been included in the parameter variation study since under in-situ conditions the amount of contact of a sewer pipe by the surrounding soil may strongly fluctuate, due to the presence of voids generated by soil erosion ([Indiketiya et al., 2019](#); [Meguid & Kamel, 2014](#); [Peter et al., 2018](#); [Schepers et al., 2022](#)). Further, the variation of the horizontal to vertical loading ratio provides insight into the sensitivity of the pipes' failure resistance to a change in lateral earth pressure, which in practice may range from active, through neutral, to passive earth pressure. Variations in the lateral earth pressure experienced by a sewer pipe may be caused by near excavations, or by other types of ground work. A reduction in wall thickness can occur under (bio)chemical corrosion, such as biogenic sulphuric acid aggression ([Belie et al., 2004](#); [Gu et al., 2018](#); [Vollertsen et al., 2008](#)). This is also the reason that the tensile strength, toughness and/or Young's modulus of the concrete can decrease in time ([Bosco et al., 2020](#); [Fan et al., 2010](#); [Ortega et al., 2019](#); [Shaowei et al., 2018](#)). In the parameter variation study, the specific FEM

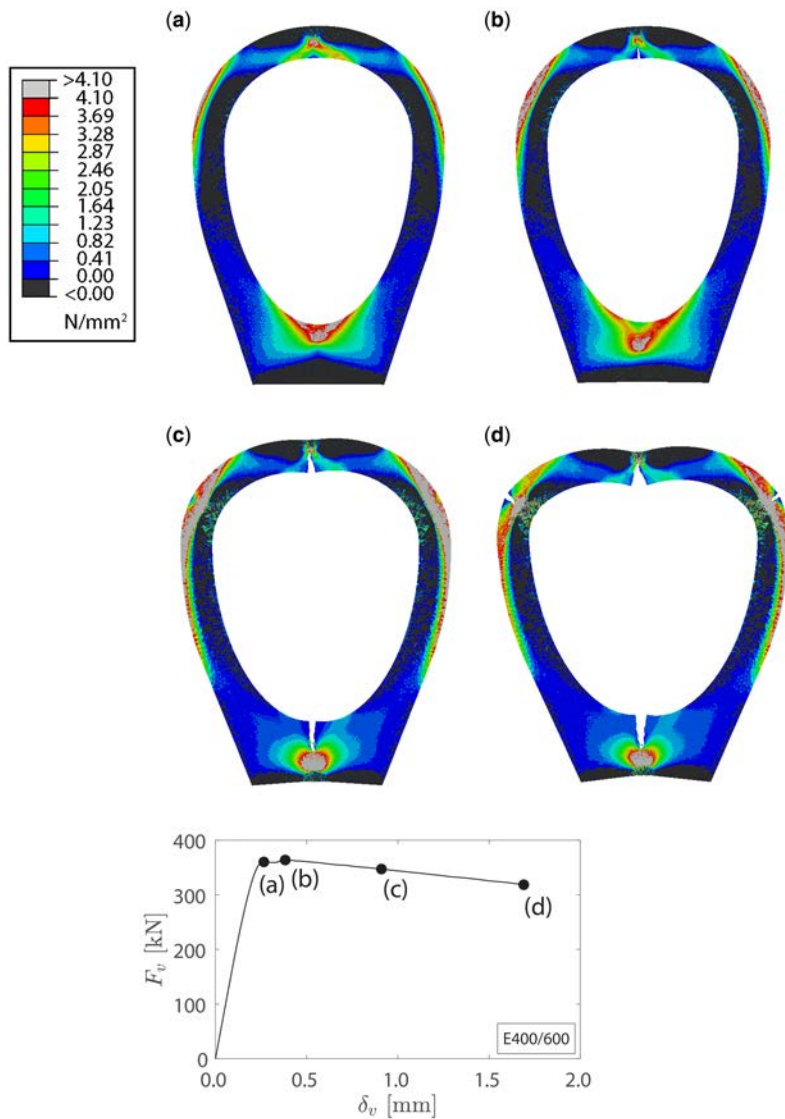


**Figure 5.33** Maximum principal stress at crack nucleation (a) and crack propagation (b)–(d) in the egg-shaped E400/600 sewer pipe, as generated under the applied biaxial loading schematized in Figure 5.27. For clarification, the deformations of the pipe geometry are magnified in the contour plots by a factor of 50. The four failure states (a)–(d) are indicated in the corresponding load–displacement diagram. The figure has been reprinted from Schepboer *et al.* (2021).

model of the R400 pipe used in the experimental validation in Section 5.7.4 will be referred to as the reference case, for which the results will be plotted by using a distinguishable red line or red symbol. The effect of the load contact area on the failure response of the round R400 sewer pipe is studied by using the (dimensionless) relative circumferential contact length  $\bar{L}_c$ , which represents the proportion of the outer pipe circumference that is in contact with the applied vertical and horizontal loads. The

relative circumferential contact length can be expressed in terms of the projected contact width  $l_c$  – illustrated in Figure 5.27a – via

$$\bar{L}_c = \frac{4}{\pi} \sin^{-1} \left( \frac{l_c}{D} \right) \quad \text{with} \quad 0 \leq \bar{L}_c \leq 1 \quad (5.10)$$

where  $D$  is the outer diameter of the round pipe. For a horizontal to vertical loading ratio of 1/3, at the lower limit  $\bar{L}_c = 0$  of zero contact area, the pipe is locally loaded at the top and bottom by a vertical point load  $F_v$ , and at the left and right outer sides by a horizontal point load  $F_h = F_v/3$ . Conversely, at the upper limit  $\bar{L}_c = 1$ , the complete pipe circumference is in contact with the applied loading, whereby the top and bottom quarter segments of the circular pipe are loaded by a distributed normal load  $\sigma$ , and the left and right quarter segments by a distributed normal load  $\sigma/3$ . For the reference case with  $l_c = 250$  mm and  $D = 524$  mm sketched in Figure 5.27a, Eq. (1) results in an intermediate value of  $\bar{L}_c = 0.63$ . Figure 5.34a depicts the vertical load  $F_v$  versus the net vertical displacement  $d_v$  of the R400 sewer pipe for a selection of contact lengths in the range  $\bar{L}_c \in [0, 1]$ , and Figure 5.34b displays the corresponding ultimate failure load  $F_{v,max}$  versus the contact length  $\bar{L}_c$ . It can be observed from Figure 5.34a that under an increasing contact area both the ultimate failure load and the associated vertical displacement increase, and that the elastic resistance against deformation becomes larger. The increase in bearing strength is caused by the fact that under a growing load contact area the pipe becomes predominantly loaded under compression, and therefore becomes less sensitive to fracture. Figure 5.34b shows that the increase in ultimate failure load is about a factor of three in the transition of a sewer pipe with a poor load contact area,  $\bar{L}_c \leq 0.2$ , to a sewer pipe with a full load contact area,  $\bar{L}_c = 1.0$ . Since the appearance of erosion voids in the soil structure embedding a sewer pipe typically leads to a more localized load transfer, such voids may substantially reduce the load bearing capacity of the pipe. Hence, to obtain a ‘damage tolerant design’ for practical sewer systems, the design procedure should account for the presence of voids, in correspondence with a reduced load contact area,  $\bar{L}_c < 1$ .

The effect of the load contact area  $\bar{L}_c$  on the failure response of the three different sewer pipe types is illustrated in Figure 5.35, by plotting the vertical load  $F_v$  against the net vertical displacement  $d_v$  for (i) the reference case shown in Figure 5.27 and (ii) a sewer pipe with a full load contact area. Note that for the R400 pipe these two load contact scenarios correspond to the curves plotted in Figure 5.34a for  $\bar{L}_c = 0.63$  and  $\bar{L}_c = 1.0$ , respectively. For the egg-shaped pipe, the case of a full load contact area has been realized by applying the vertical pressure  $\sigma$  in the same fashion as for the two round pipes, that is, at the quarter circular segment defining the top part of the egg-shape pipe geometry. In addition, the remaining left and right sides of the egg-shaped pipe were exposed across their full

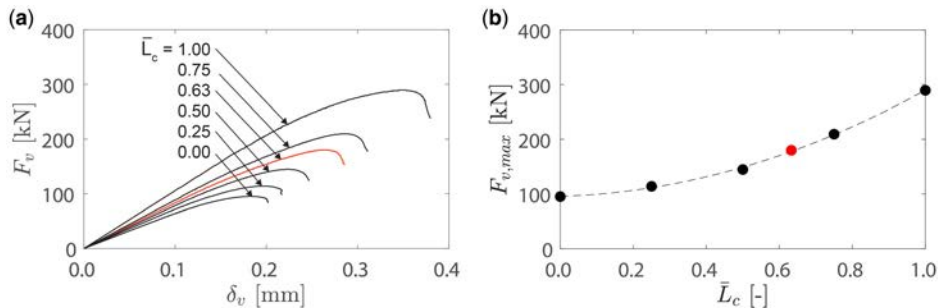


**Figure 5.34** Influence of the relative circumferential contact length  $L_c$  on the failure response of the round R400 sewer pipe. The results for the reference case shown in Figure 5.27 are depicted in red. The dashed line in the figure for  $F_{v,max}$  indicates the best fit to the FEM results. The figure has been reprinted from Scheperboer *et al.* (2021).



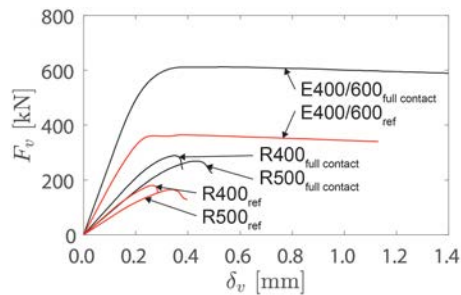


**Figure 5.35** Load–displacement response of the R400, R500 and E400/600 sewer pipes with (i) a load contact area corresponding to the reference case shown in [Figure 5.27](#) (red lines) and (ii) a full load contact area (black lines).

length to a horizontal pressure  $\sigma/3$ , in correspondence with a horizontal to vertical loading ratio of  $1/3$ . It is observed that for all three pipe types the elastic stiffness, as well as the ultimate failure load and the associated vertical displacement, increase with increasing load contact area. The load bearing capacity under full load contact is 289.4, 268.9 and 612.0 kN for the round R400 and R500 pipes and the egg-shaped E400/600 pipe, respectively. In comparison to the respective values of 180.0, 165.5, and 363.7 kN related to the reference case, the relative increase in load bearing capacity is 61%, 62% and 68%, respectively, which thus appears to be similar for the three sewer pipe types.

A mutual comparison of the ultimate failure loads of the three pipe types for the case of a full load contact area shows that the ultimate failure load of the round R500 pipe is a factor of  $289.4/268.9 = 1.08$  smaller than that of the round R400 pipe, and a factor of  $612.0/268.9 = 2.28$  smaller than that of the egg-shaped E400/600 pipe. Note that these values are comparable to the corresponding values of 1.16 and 2.25 measured in the experiments (whereby, as shown in [Figure 5.27](#), the load contact area is smaller), see Section 3.3.

As explained above, for the construction of [Figure 5.34](#) the load contact area  $\bar{L}_c$  has been varied simultaneously at the four specific locations of the external loading applied in the full-scale experiments, that is, at the top, bottom, left and right sides of the pipe specimen. Other studies that consider the influence of soil erosion voids on the mechanical strength of concrete pipes consider alternative profiles of limited load contact area ([Meguid & Kamel, 2014](#); [Peter et al., 2018](#); [Scheperboer et al., 2022](#)). Nevertheless, similar to the present study, such studies also demonstrate that a reduction of the load contact area may significantly reduce the load bearing capacity of the pipe.

### 5.7.7.1 Horizontal to vertical load ratio

The effect of the horizontal to vertical load ratio on the failure response of the R400 sewer pipe is examined by varying the horizontal to vertical load ratio  $K$  in the range  $K \in [0, 1]$ , see [Figure 5.36](#). The value  $K = 0$  relates to uniaxial compression. Here, the horizontally distributed load equals zero, and the pipe is effectively subjected to a vertically distributed load, as the net horizontal component of the normal pressure load  $\sigma$  applied at the both the top and bottom of the pipe is also zero, see also [Figure 5.27a](#). In addition,  $K = 1$  effectively corresponds to equibiaxial compression, whereby the horizontally and vertically distributed loads are equal to each other. Note that the reference case is in agreement with an intermediate value,  $K = 1/3$ . It is seen from the load–displacement diagram in [Figure 5.36a](#) that under an increasing value of  $K$  the ultimate vertical failure load and the vertical displacement at failure first both increase. However, the vertical displacement at failure starts to decrease when  $K$  approaches unity,  $K = 1$ , whereby the post-peak response becomes characterized by a snapback behaviour, instead of a softening behaviour that typifies the post-peak responses for lower values of  $K$ . The fracture behaviour at  $K = 1$  is also different compared to that for lower values of  $K$ ; as indicated in the contour plot shown in [Figure 5.37](#), at failure the polar shear stress  $\Sigma_{rt}$  in the thickness direction

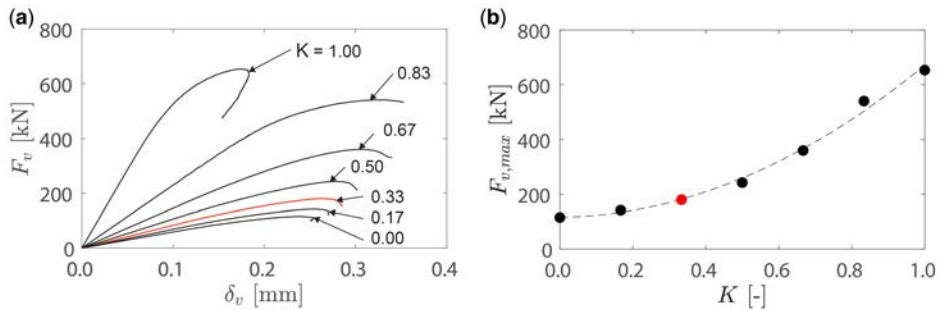


**Figure 5.36** Influence of the horizontal to vertical load ratio  $K$  on the failure response of a round R400 sewer pipe. The results for the reference case shown in Figure 5.27 are depicted in red. The dashed line in the figure for  $F_{v,max}$  indicates the best fit to the FEM results. The figure has been reprinted from [Scheperboer et al. \(2021\)](#).

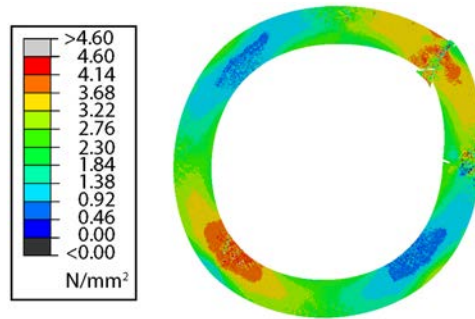


**Figure 5.37** Polar shear stress  $\sigma_{rt}$  (along the pipe thickness direction) at failure under equibiaxial compression, whereby the vertical loading  $\sigma$  sketched in Figure 5.27a equals the horizontal loading, in correspondence with a load ratio  $K = 1$ . For clarification, the deformations of the pipe are magnified in the contour plot by a factor of 100. The figure has been reprinted from [Scheperboer et al. \(2021\)](#).

of the pipe (with the subscripts ‘r’ and ‘t’ indicating the radial and tangential directions, respectively) has reached the mode II fracture strength  $t_u^2 = \pm 4.6$  N/mm<sup>2</sup> (indicated by the red and blue colours in the contour plot) at locations oriented under an angle of  $\pm 45^\circ$  with the horizontal  $x$ -axis, that is, at the top-left, top-right, bottom-left and bottom-right sides of the pipe. Accordingly, at the top-right side of the pipe a mode II failure crack develops. The stress redistribution generated under this progressive mode II crack makes that the other three regions with maximum shear stress start to unload, and that a small mode I crack with limited crack length emerges halfway the right specimen side. Although the specimen here effectively fails under mode II cracking, it is emphasized that this fracture behaviour is characterized by the selection of modes I and II fracture strengths of equal magnitude,  $t_u^1 = t_u^2 = 4.6$  N/mm<sup>2</sup>, and thus may change when the ratio between the magnitudes of the mode II and mode I fracture strengths is larger than unity.

Figure 5.37b illustrates the ultimate failure load as a function of the horizontal pressure coefficient  $K$ . The reference case with  $K = 1/3$  mimics a practical situation of neutral horizontal earth pressure, so that  $K < 1/3$  and  $K > 1/3$  cover the regimes of active and passive horizontal earth pressure, respectively. The failure resistance of the pipe is the lowest in the regime of active earth pressure, although the ultimate failure load remains fairly constant for  $0 \leq K < 1/3$ . When entering the regime of passive earth pressure,  $K > 1/3$ , the failure resistance of the pipe substantially increases under an increasing

value of  $K$ , eventually reaching an equibiaxial failure load at  $K = 1$  that is more than three times higher than the failure load under neutral earth pressure,  $K = 1/3$ . Hence, for practical pipe design a conservative approach is to determine the pipes' failure resistance in correspondence with critical loading conditions representative of the range of active to neutral earth pressures,  $K \leq 1/3$ .

### 5.7.7.2 Wall thickness

The influence of a reduction in wall thickness on the failure response of the R400 sewer pipe is explored by keeping the outer diameter of the pipe fixed and varying the inner diameter. Accordingly, the reduced wall thickness is considered to be the result of a (bio)chemical corrosion process that takes place from the inside of the pipe. The reduced wall thickness is expressed in terms of the relative thickness ratio  $t/t_{\text{ref}}$ , with  $t$  the wall thickness of the corroded pipe, and  $t_{\text{ref}}$  the wall thickness of the uncorroded pipe corresponding to the reference case studied in Section 5.7.4. The influence of a reduction in wall thickness on the pipes' failure response is illustrated in Figure 5.38. Figure 5.38a clearly shows that a decrease in wall thickness leads to a decrease in the ultimate failure load and effective stiffness of the pipe, and further results in an increase of the deformation at which the ultimate failure load is reached. From Figure 5.38b it is observed that a wall thickness decrease by 20% ( $t/t_{\text{ref}} = 0.8$ ) already induces a reduction in the ultimate failure load  $F_{v,\text{max}}$  by almost 40%, while a wall thickness decrease of 50% ( $t/t_{\text{ref}} = 0.5$ ) reduces  $F_{v,\text{max}}$  by somewhat more than 75%. This result emphasizes the importance of accurately monitoring the degradation of the inner surface of sewer pipes during their lifetime for the estimation of the load bearing capacity.

### 5.7.7.3 Tensile strength, mode I toughness and Young's modulus

The effect on the sewer pipes' failure response by the tensile strength  $t'_u$ , mode I toughness  $G_{I,c}$  and Young's modulus  $E_c$  of the concrete is shown in Figures 5.39–5.41, respectively.

The material properties have been normalized by a division of the value representative of the reference case discussed in Section 5.7.4. It can be observed that a decrease of each of these material parameters may considerably reduce the load bearing capacity of the pipe. Figures 5.39a and 5.40a show that a decrease of the tensile strength  $t'_u$  and mode I toughness  $G_{I,c}$  lead to a decrease of the vertical displacement at which the ultimate failure load  $F_{v,\text{max}}$  is reached. In contrast, Figure 5.41a illustrates that a decrease of the Young's modulus  $E_c$  enlarges the displacement associated with the ultimate failure load. In specific, when the relative Young's modulus approaches to zero,  $E_c/E_{c,\text{ref}} \rightarrow 0$ , the displacement associated with the ultimate failure load grows unboundedly towards infinity. Note that the minimal load bearing capacity  $F_{v,\text{max}} \approx 90$  kN computed near the limit of a zero Young's modulus is comparable to the minimal load bearing capacity calculated for a zero mode I toughness,

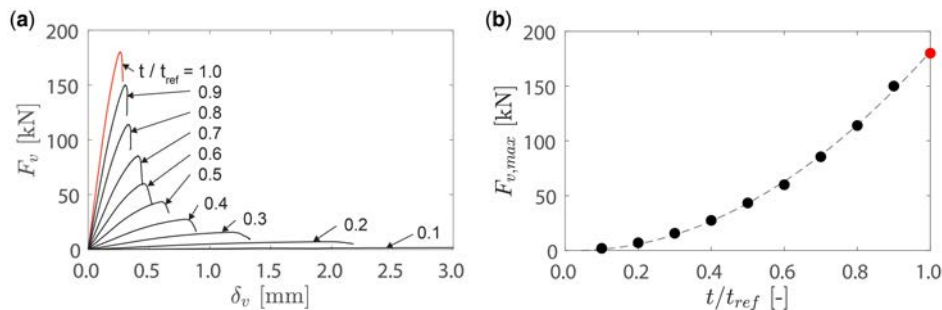


**Figure 5.38** Influence of the relative wall thickness  $t/t_{\text{ref}}$  on the failure response of a round R400 sewer pipe. The results for the reference case shown in Figure 5.27 are depicted in red. The dashed line in the figure for  $F_{v,\text{max}}$  indicates the best fit to the FEM results. The figure has been reprinted from Schepërboer *et al.* (2021).

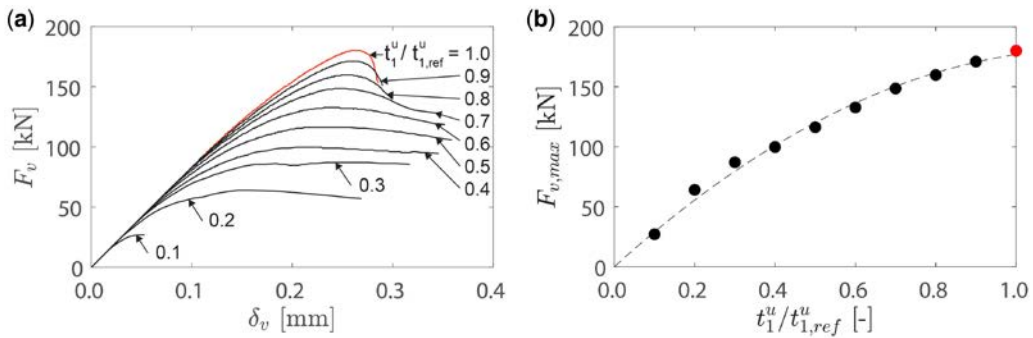


**Figure 5.39** Influence of the relative tensile strength  $t_1^u/t_{1,ref}^u$  on the failure response of a round R400 sewer pipe. The results for the reference case shown in Figure 5.27 are depicted in red. The dashed line in the figure for  $F_{v,max}$  indicates the best fit to the FEM results. The figure has been reprinted from Schepërboer *et al.* (2021).

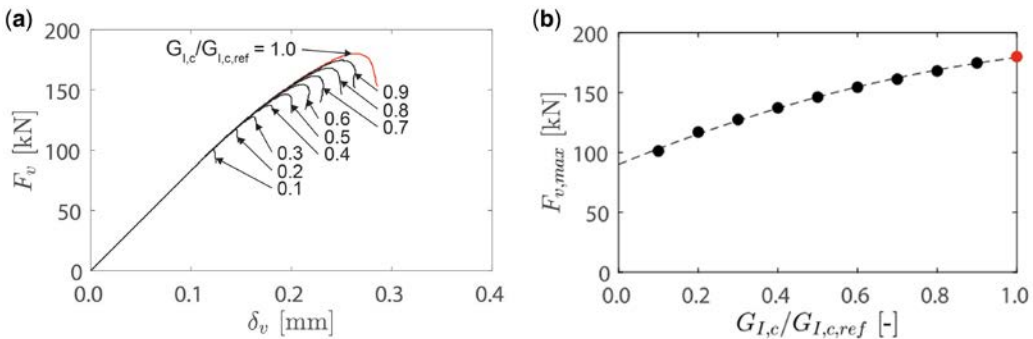


**Figure 5.40** Influence of the relative mode I toughness  $G_{1,c}/G_{1,c,ref}$  on the failure response of a round R400 sewer pipe. The results for the reference case shown in Figure 5.27 are depicted in red. The dashed line in the figure for  $F_{v,max}$  indicates the best fit to the FEM results. The figure has been reprinted from Schepërboer *et al.* (2021).

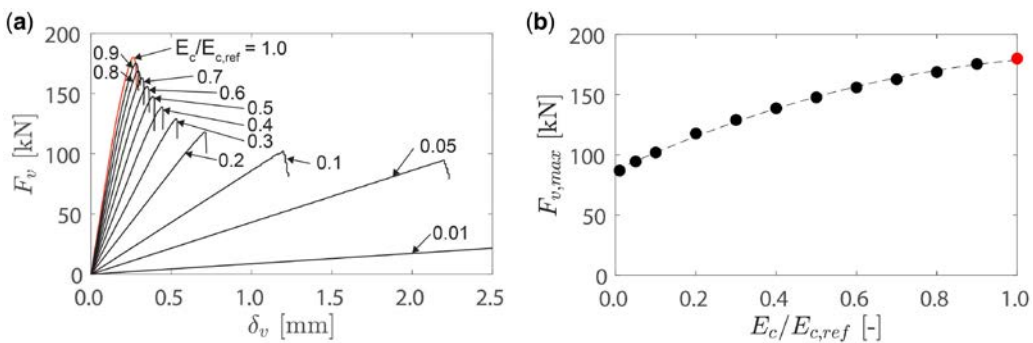


**Figure 5.41** Influence of the relative Young's modulus  $E_c/E_{c,ref}$  on the failure response of a round R400 sewer pipe. The results for the reference case shown in Figure 5.27 are depicted in red. The dashed line in the figure for  $F_{v,max}$  indicates the best fit to the FEM results. The figure has been reprinted from Schepërboer *et al.* (2021).

$G_{1,c}/G_{1,c,ref} \rightarrow 0$ , see [Figures 5.41b](#) and [5.5.40b](#), respectively. The above results clearly illustrate how the bearing strength of concrete sewer pipes depends on various factors (load contact area, load ratio, wall thickness, tensile strength, toughness, Young's modulus) that can be associated with degradation processes, such as soil erosion, changes in lateral earth pressure, biochemical degradation and ageing. Additional experimental and modelling research is needed to establish accurate relations between these factors and the corresponding degradation process(es), which will allow to directly connect the reduction in bearing strength following from the present computational results to the specific characteristics of a degradation process.

In [Luimes \*et al.\* \(2022\)](#) additional research results can be found on the structural response and failure mechanisms of 35 *used* concrete sewer pipes, as studied by means of a combined experimental–numerical approach, whereby specific attention focuses on determining the effect by biochemical attack. The degree of degradation of the inner and outer surfaces of the pipes is carefully analyzed by visual inspection, and subsequently categorized into six different surface condition classes. The type and degree of biochemical attack are determined by respectively performing X-ray diffraction analyses and phenolphthalein tests. The sewer pipes, which vary in age, size and geometry, are subjected to biaxial loading conditions in a full-scale test set-up. The experiments show that the material degradation of relatively old sewer pipes can be considerable, and for a large part may be attributed to the process of biogenic sulphide corrosion. This process typically induces a weak, corroded layer at the inside of the pipe, which is characterized by the appearance of exposed granulates and porous mortar between the granulates. The experimental failure responses of the used sewer pipes are compared against numerical results obtained from detailed FEM simulations. It is demonstrated that the failure response of each sewer pipe type is well predicted by the FEM model if the negligible mechanical properties of the biogenic sulphide corrosion layer at the inside of the pipe are accounted for in the simulations. The relatively low concrete tensile strength of old sewer pipes and the reduced effective wall thickness due to biogenic sulphide corrosion cause that the ultimate bearing strength and structural stiffness of these pipes may be more than a factor of two lower than those of completely new sewer pipes. The results of the work in [Luimes \*et al.\* \(2022\)](#) provide a scientific basis for the decision-making process on sewer rehabilitation and replacement, in particular by revealing and quantifying the influence on the structural bearing strength by biogenic sulphide corrosion.

## 5.8 LOSS OF HYDRAULIC CAPACITY

### 5.8.1 Introduction

The hydraulic capacity of (classical) UD systems is determined in the design phase and depends on local climate conditions and is subject to various (local) design rules. In general, the hydraulic capacity is designed to:

- limit the risk and extend of urban flooding to some acceptable limit (basically a political choice), and
- limit the discharge of various degrees of polluted water (either wastewater, stormwater runoff or discharges from combined sewer systems) into either open water courses or groundwater bodies.

The former demand results in selecting dimensions for water conveyance elements in the system (e.g., pipes, weirs, valves and so on) while the latter demand also puts the onus on the available storage capacity in the system. Both the discharge capacities and the storage capacities are subject to processes that decrease them.

### 5.8.2 Storage capacity

Loss of storage capacity can result from various processes, the most important being subsidence and sedimentation. Subsidence, or more precisely, non-uniform subsidence with subsidence differences over a relatively short distance (i.e., in the order of magnitude of say 100 m) may be the cause of *lost*



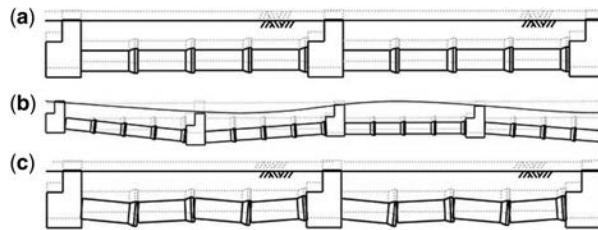


**Figure 5.42** Lost storage due to local subsidence Dirksen (2013) (image 3.1 p38).

*storage*'. The concept of lost storage is depicted in Figure 5.42. While, as part of the original design and construction it had typically been ensured that no local minima in terms of the invert elevation of the pipes were present, however, due to subsidence of the surrounding soil (e.g., clay or peat) such local minima may have evolved over the course of the lifetime of the system.

These 'sags' form pockets from which water cannot be drained to either an outlet or a pumping station. Especially in sanitary or combined sewer systems the occurrence of such sags is a trigger for a range of processes that, in general, cause deterioration of the functionality of the system. In the first place, not all storage capacity in the sags will be available for storage of water during storm events triggering more frequent occurrence of spills of (diluted) wastewater to receiving water bodies if no corrective action is taken. A second process is the accumulation of sediments in these sags; locally, the transport capacity of solids is substantially reduced, allowing sediments to settle, up to the point at which a new morphological equilibrium is established. During heavy storm events, however, the presence of such accumulated pockets of sediments may result in the 'sudden' release of substantial amounts of pollutants that are flushed out, adding to the environmental impacts of CSO events.

A further contribution to the functional deterioration from subsidence is the fact that in the sags the accumulated sediments, of which a substantial part may consist of biodegradable materials (see e.g., Ashley *et al.*, 2004), act as a reservoir worsening the formation of corrosive substances (e.g., sulphuric attack, see Section 5.5). This process may, in turn, negatively affect the geometry of the pipe (due to concrete corrosion) as well as the hydraulic roughness of the pipe wall. Also, at a catchment scale, subsidence may negatively affect the functioning of the system as whole. Dirksen *et al.* (2012) and Dirksen (2013) reported a clear relation between the subsidence of the sanitary sewer pipes and the occurrence of blockages. The latter may occur when the subsidence reaches a level at which no free water surface is present, see Figure 5.43. In such a case, floating material starts to slowly accumulate at the top of the conduit, until blockage occurs. Even modest settling rates of a few mm/year may trigger substantial problems with sedimentation and/or the accumulation of floating solids (e.g., FOG). Both processes result in a significant reduction of both the storage and the hydraulic conveyance capacity of the system over time. In some extreme cases this may become manifest on time scales of a few months to a few years.

In some cases, siphons are subject to conveyance capacity loss due to the occurrence of three-phase flow phenomena. For example, Figure 5.43 presents several profiles of FOG deposits as measured in siphons in a combined sewer system in the City of Amsterdam, The Netherlands. The brown areas represent the FOG. Although not explicitly observed, a hypothesis of the chain of events responsible for the conditions observed is as follows:

- At the point where the siphon becomes pressurised, floating FOG sticks to the wall of the pipe; these locations vary over time due to the varying dry weather flow discharge.
- In the process, the cross-sectional area decreases resulting in a local increase of the flow velocity.
- This, in turn, increases the amount of air that can be transported into the falling leg of the siphon, allowing for FOG to be deposited deeper into the siphon.

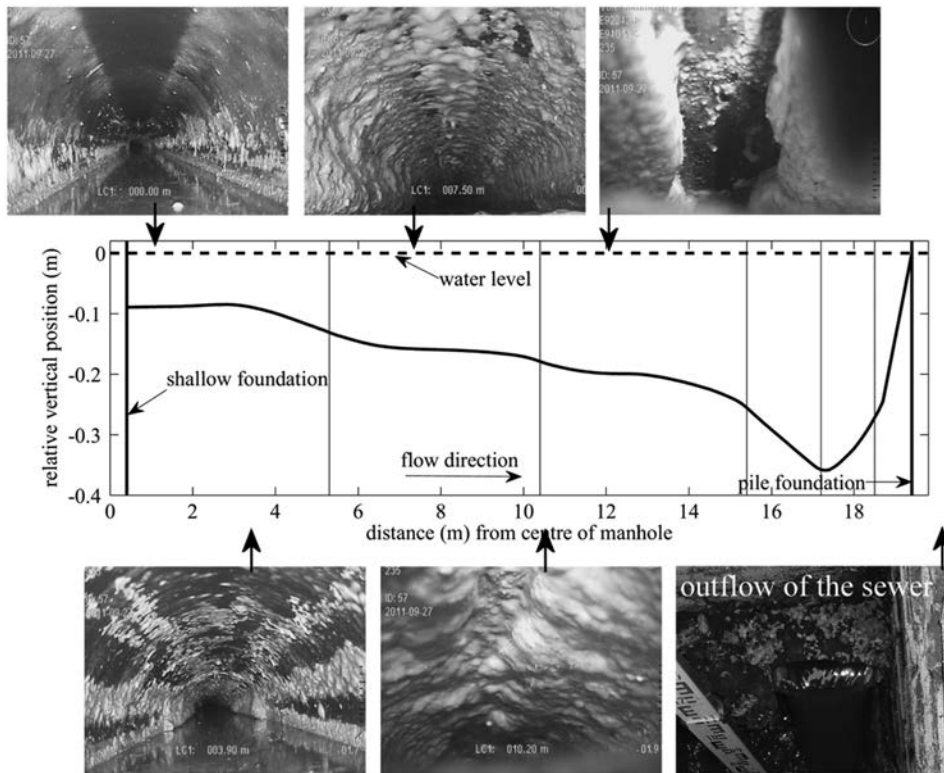


**Figure 5.43** Inspection result of a sewer with a filling degree of 100%. The graph represents the vertical cross section of the sewer. (Dirksen *et al.*, 2013b).

- During storm events, air can be transported along the entire length of the siphon causing FOG deposits along its entire length. In one case (i.e., the Entrepotdok siphon in Figure 5.44) this resulted in the creation of an air pocket in the middle of the siphon causing it to move upwards.
- Due to the reduction of the cross-sectional area along a substantial length of the siphons, in addition to the storage capacity, the hydraulic conveyance capacity is significantly reduced as well.

A typical time scale for these processes to develop is about 1 year. Therefore, regular inspection and cleaning of siphons is warranted, especially at locations that are notorious in suffering from FOG (e.g., in the presence of high concentrations of restaurants).

### 5.8.3 Discharge capacity

#### 5.8.3.1 Introduction

The discharge capacity of a pipe is a function of its length, shape and dimensions of its cross-sectional area as well as the roughness of the pipe wall. Except for the length, all other parameters are subject to change over time. In many design manuals the roughness (or Manning's coefficient) only reflects the type of material of a pipe (e.g., concrete has a rougher texture than for instance PVC or steel) hinting at a difference in hydraulic resistance. Although this may be true for new pipes and/or pipes that are used to transport clean fluids, it is certainly **not** true when a pipe ages and/or when either sediments or gases are present in the transported medium. Given that UD systems typically are expected to accommodate wastewater and/or urban stormwater runoff, it is highly likely that solids and gases **will** be present.

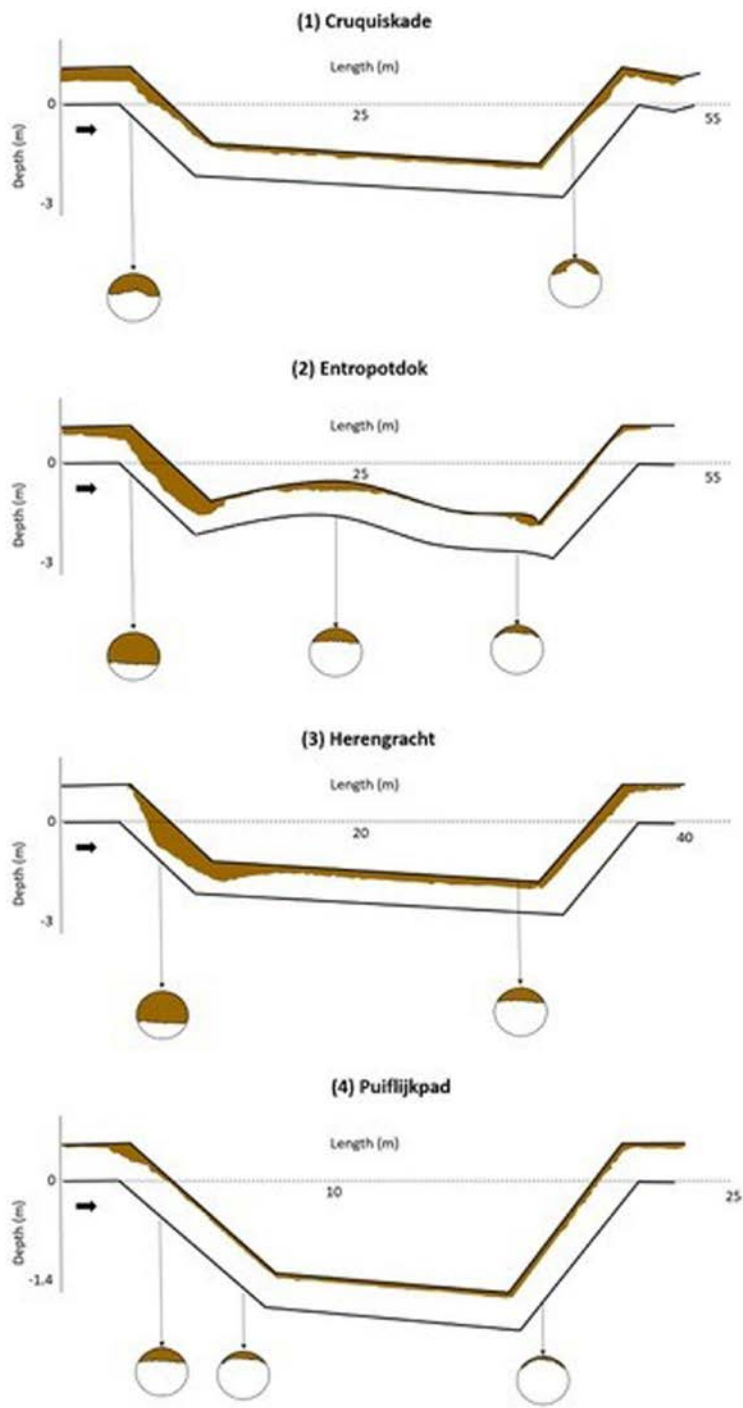


Figure 5.44 FOG deposits in siphons, as measured in Amsterdam, The Netherlands (after de Groot, 2015).

Further, the presence of obstacles (e.g., protruding inlets, root intrusion, debris dumped in the system or remnants from construction activities) may cause significant capacity reductions as does the ingress of soil through cracks or defective joints. Also, a change of the slope, for example, caused by subsidence discussed in the previous section, can result in sedimentation and, in turn, in a reduction of the conveyance capacity.

For pressurized systems, the accumulation of air/gases is a well-known cause of capacity losses that, when the system is pumped, also result in an increased energy consumption. In addition, in such systems the deterioration of the pump is a factor to be reckoned with as well.

### 5.8.3.2 Obstacles

Van Bijnen (2018) and van Bijnen *et al.* (2016) describe a case study in the Netherlands in which a hydrodynamic model of a small catchment (see Figure 5.45) had been calibrated using several storm events in 2010 and 2015, respectively. For the 2010 scenario, known defects were present in the system (i.e., sediment deposits and root intrusions). These obstacles had been removed in 2012 and the model was calibrated again with additional storm events in 2015. In both cases the system as modelled was supposed to be clean (as is usually done when using a hydrodynamic model). For the perfect case, the residuals (i.e., the differences between measured and modelled water levels) show a Gaussian distribution similar to the uncertainty in the measured values. When the residuals do not present a similar distribution, it indicates the presence of some kind of systematic deviation between the model and the ‘real’ world, for example, some dimensions are incorrect or wrong invert levels have been used. Such deviations can be eliminated by a careful check of the data describing the structure and geometry of the system in question.

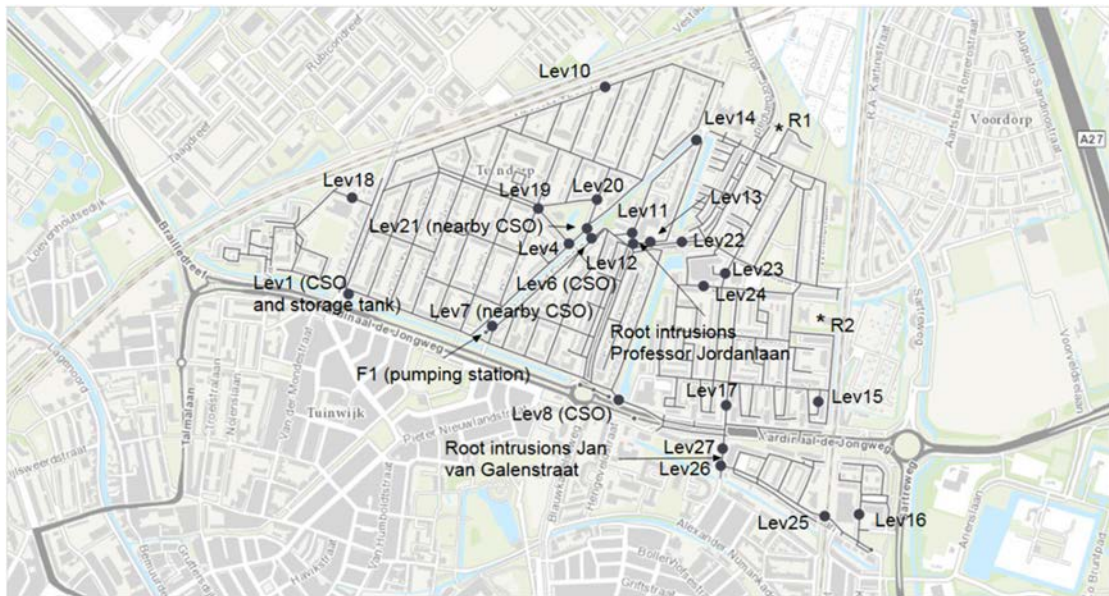


**Figure 5.45** Monitoring network ‘Tuindorp’ catchment. Flows (F1), water levels (Lev1, Lev2, ..., Lev27) and rainfall (R1 and R2) were monitored at several locations in the catchment area. The monitoring network design was based on a combination of hydraulic simulations, reported incidents and observed in-sewer defects. For example, several water level sensors (Lev12 and Lev13 Professor Jordanlaan, Lev23 and Lev24 Troosterlaan, Lev26 and Lev27 Jan van Galenstraat) are installed in the manholes just upstream and downstream of an observed defect. Two tipping-bucket rain gauges (R1 and R2) were used to measure rainfall in ‘Tuindorp’. (Source: van Bijnen, 2018).



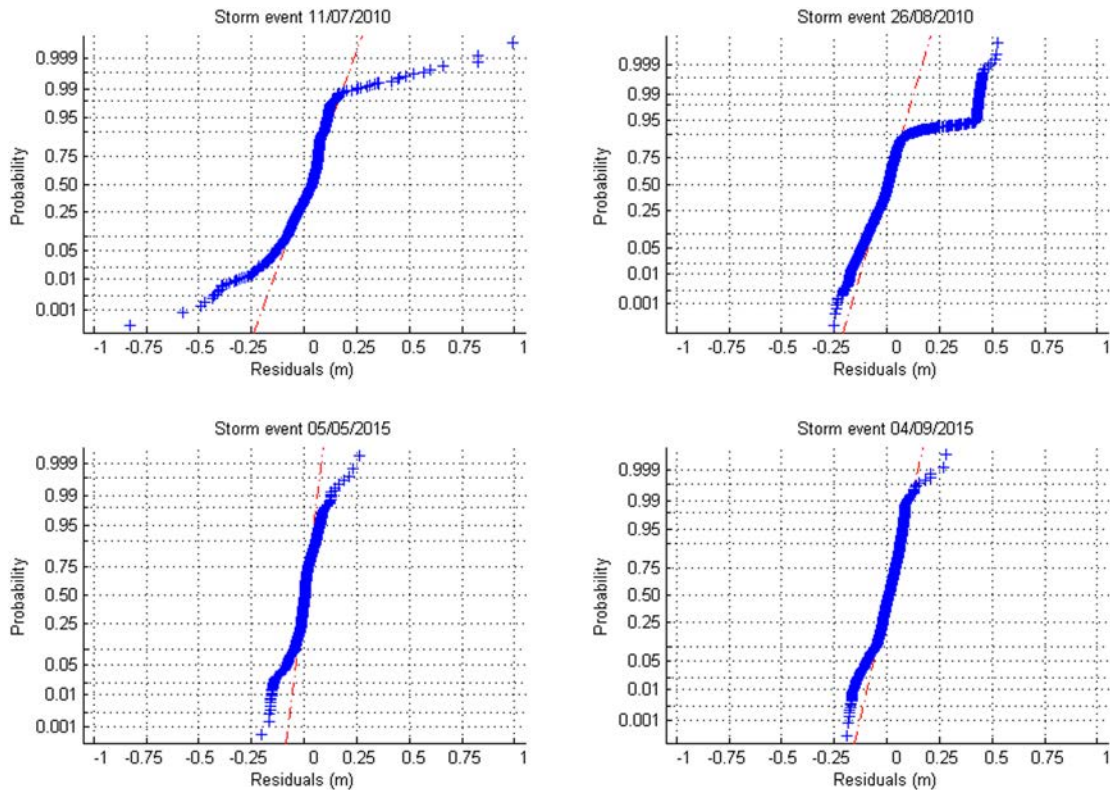


**Figure 5.46** Normal probability plots of residuals after calibration of the 'clean' system (storm events 05/05/2015 and 04/09/2015) and the system including defects (storm events 11/07/2010 and 26/08/2010). Residuals of all measuring locations. (Source: van Bijnen, 2018).

An analysis of the residuals suggests that for the 2010 scenario the residuals do display a Gaussian distribution with large variations ( $>0.75$  m), see Figure 5.46. Indeed, when analysing the residuals for the (clean) 2015 scenario, they much better resemble a Gaussian distribution with the maximum deviation limited to circa 0.25 m. This example illustrates how the presence of sediment and obstacles in a sewer system can show up when doing a regular check on the hydraulic performance using a well calibrated model as a reference (i.e., hydraulic fingerprinting). Based on further analysis van Bijnen *et al.* (2018) concluded that the risk of citizens being infected due to the increased occurrence of urban flooding (i.e., at more locations, covering a larger area, and with longer time windows) increased with a factor of about 1.5, stressing the importance of a regular evaluation of the performance of a systems as a whole.

Inspections confirmed that a substantial root intrusion was indeed present in the direct vicinity of this monitoring location (Figure 5.47). The geometry of this intrusion, however, was only apparent when the water level exceeded a certain threshold.

### 5.8.3.3 Air/gas inclusions (pressurized pipes only)

In most designs of hydraulic structures in UD systems as well as during their operation, relatively straight forward one phase flow is implicitly assumed. In practice however, in many cases this is an



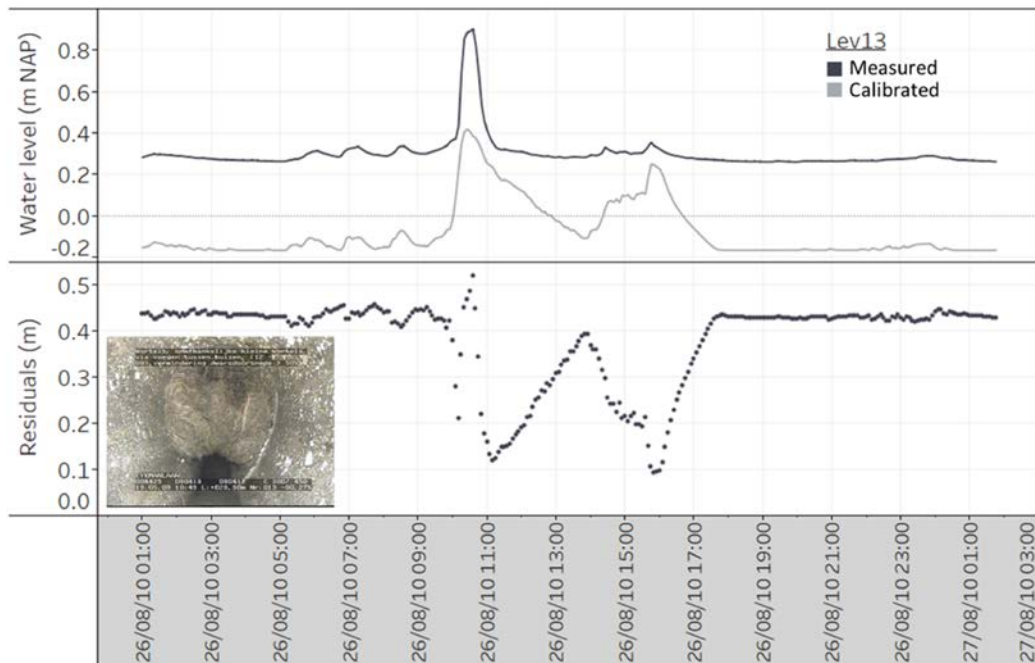


**Figure 5.47** Measured and modelled (calibrated) water levels upstream (Lev13) of a root intrusion at the Professor Jordanlaan for the event of 26 August 2010. NAP is reference level. Negative measured and calibrated values represent water levels below this reference. (Source: van Bijnen, 2018).

oversimplification, especially when faced with pressurized systems transporting either wastewater or a wastewater/stormwater mixture (as occurs in combined sewer systems) or when siphons are implemented to cross water courses such as canals. The occurrence of gas/air pockets is known to have significant adverse effects on the functionality of such systems (Lubbers, 2007; Pothof, 2011). The formation of air/gas pockets is due to air entrainment in pumping stations, malfunctioning of venting systems or the production of biogas that accumulates at high points in the system (e.g., at the upstream end of siphons). The presence of such gas pockets may give rise to local corrosion in pressure mains, and results in significant loss of hydraulic capacity and energy efficiency. In some cases, even air lock may occur reducing the hydraulic capacity to virtually zero. Kooij *et al.* (2015) present a case study on monitoring the evolution of capacity loss due to air/gas pockets in an extensive system of pumping stations and pressure mains. As discussed in Section 5.7.2 the dynamics of the gas/water/floating material interface may result in substantial FOG deposits in siphons, reducing the hydraulic capacity as well.

The underlying processes and methods to remedy capacity loss due to air/gas pockets are well understood and can be relatively easily quantified using hydrodynamic models. A comprehensive book on the subject is available at IWA Publishing (Tukker *et al.*, 2016), in addition to German guidelines (DWA-A 113; DWA-M 149-9). While the effects of air/gas pockets on the hydraulic capacity as well as the rate of transporting gas/air can well be quantified, the rate at which air/gas accumulates, however is less straight forward to be quantified.

In case of air entrainment in pumping stations, the pump operation and the geometry of the pump sump play a major role. When the formation of biogas is the main contributing factor, the composition

of the (waste)water and environmental conditions (i.e., mainly temperature) and how they vary with time play a major role. In practice, the formation of air gas pockets can be avoided by:

- a proper initial design of the system,
- regular checks (e.g., every 6 months) pertaining to the proper functioning of venting valves, and
- monitoring of the discharge, pressure head and energy consumption of the system (Kooij *et al.*, 2015).

The time scales at which changes in hydraulic losses due to the presence of air/gas pockets can be measured range from weeks to years as a function of the contributing processes and the day-to-day operation and management of the system.

#### 5.8.3.4 Sedimentation

Sedimentation is a process that may occur in any UD system and is a key process in the loss of functionality. Accumulation of sediments in pipes reduces the hydraulic capacity (including infiltration for NBS), the volume available for storage and may even lead to complete blockage of elements. Sedimentation has already been discussed in the present chapter in the clogging [Section \(5.3\)](#) and the storage capacity [Section \(5.8.2\)](#). Moreover, a very comprehensive text on sedimentation is provided by [Ashley \*et al.\* \(2004\)](#). Therefore we will not provide a detailed text here but we will restrict this to some recent work relating sedimentation to functionality.

[Van Bijnen \*et al.\* \(2012\)](#) concluded, based on a large amount of field data on sediment deposits and subsequent hydrodynamic modelling that the presence of sediments may result in a very substantial loss of hydraulic capacity. Sediment deposits may occur at a wide range of timescales (typical weeks to years) depending on the activities in the catchment, soil conditions, quality of the construction of the system, industry discharges and so on.

#### 5.8.3.5 Ageing of pumps

In many UD systems mechanical sub-systems (e.g., pumping stations, moveable weirs, etc.) are present. These sub-systems have the 'advantage' that malfunctioning becomes more rapidly apparent and pronounced compared to, for instance, a partial loss of the hydraulic capacity of a gravity sewer, or the gradual reduction of the infiltration capacity of NBS. This loss of functionality can be caused by damage of the impeller, which can be the result of wrong pump operations or a poor, initial pump design (e.g., occurrence of cavitation). However, it can also be caused by sustained abrasion due to the presence of for example, sand in wastewater. Such normal ageing becomes manifest in increased energy consumption, vibrations and a decreased discharge. Typically, impellers and bearings are replaced every ten to fifteen years depending on the operational conditions. In extreme cases replacement may be needed every few months; this typically suggests that a pump is being operated beyond its original design intent.

Apart from this 'normal' wear of the impeller which may occur over several years, clogging because of rags or plastic being sucked into the pump may cause sudden failure of the pump ([Figure 5.48](#)).

Little literature exists describing deterministic modelling of wastewater pumps ([Jensen, 2018](#)) with a few contributions pertaining to statistical models ([Korving, 2004](#); [Korving & Ottenhoff, 2008](#); [Korving \*et al.\*, 2006a](#)). As a result of the statistical analysis of data from pump failures in combined sewer systems, [Korving and Ottenhoff \(2008\)](#) present a positive correlation between pump age and failure rate illustrated by means of a typical 'bathtub' or U-shape. Directly after installation a high failure rate tends to be observed reflecting construction defects and 'start-up' problems. After overcoming this initial phase (which typically lasts about one to two years) a period of about ten years with relatively consistent failure rates can be observed. After this ten-year period the failure rate gradually increases due to material ageing, damage to bearings, impellers and so on. An important factor contributing to the failure rate of pumps, in combined and/or wastewater systems, is the presence of sediments, solids materials and gross solids in the wastewater. [Korving and Ottenhoff, \(2008\)](#) report, based on verbal



**Figure 5.48** Clogged pump. (Source: Deltares).

information provided by maintenance personnel, that 95% of reported pump failures are (at least partially) related to clogging. In addition to the direct costs of repairs/replacement, malfunctioning of pumps reportedly contributes to substantial (and largely avoidable) spills of sewage via CSOs into receiving waterbodies, with adverse effects on their habitat and human health (Korving *et al.*, 2006b; Giakoumis & Voulvoulis, 2023). A recent article by Hallaj *et al.* (2022) provides a state-of-the-art overview on preventive maintenance of pumps used in civil engineering infrastructure.

#### 5.8.3.6 Scum layers

Formation of layers of floating material in (wastewater) pump sumps may cause pump failure (Duinmeijer, 2020; Korving, 2004). Cleaning out such layers, consisting of FOG (Fat, Oil and Grease) intermixed with floating materials like rags, plastic bottles, and so on., (Figure 5.49) is a costly and unpleasant job

Nieuwenhuis *et al.* (2018) conclude, based on an evaluation of 126 pumping stations in combined sewer systems, that there are three main factors influencing the occurrence of problematic scum layers:

- the average income of the inhabitants within the catchment is negatively correlated to the presence of scum layers,
- the density of restaurants or catering industry within the catchment is positively correlated with the occurrence of scum layers, and
- the intensity of ‘mixing’, or turbulence in the pump sump is negatively correlated with the occurrence of scum layers.

Apart from being a cause of pump clogging, the presence of scum/FOG layers in pump sumps may block degassing of the wastewater, in the process disabling monitoring systems for the occurrence of potentially hazardous gas mixtures (e.g.,  $H_2S/O_2$ ). When disturbing such a layer unexpected gas may be emitted with potential disastrous health threats for personnel.



Figure 5.49 FOG in pump well. (Source: Duijnmeijer, 2020).

Only recently, a method was developed to monitor the dynamics of the formation of scum layers (Moreno-Rodenas *et al.*, 2021). So far, the following conclusions have been drawn:

- Choices as to pump management influence the dynamics of the scum layers.
- Changes are seen at small timescales, (i.e., in the order of hours to days) indicating that more regular inspection/cleaning activities are called for than is normally done (one to two times per year).
- There is a clear influence of the occurrence of storm events (in combined sewer systems).

To date, to the authors' knowledge, no attempts to model the dynamics of FOG layers have been reported, likely due to lacking knowledge as to the underlying processes.

## 5.9 SEPARATION OF FLOWS

### 5.9.1 Introduction

Water discharged from urban areas comes in varying qualities, starting with wastewater (discharged from households and industry) that needs to be treated prior to being discharged into the environment. In addition, there is stormwater runoff that may be polluted to varying degrees, depending on the nature of the tributary catchment and the characteristics of the storm events (i.e., reflecting the variability in rain intensity and duration). This stormwater runoff (e.g., when from areas with a heavy traffic load) should get some basic or more sophisticated form of treatment prior to discharge. Further, one should avoid having wastewater leak into groundwater bodies, or vice versa, have groundwater infiltrate either system carrying wastewater or stormwater. The former situation may result in contamination of groundwater, and, by extension, of wells used for producing drinking water. In the latter case, the infiltrating groundwater may consume discharge capacity, dilute the wastewater and may even trigger local scouring of the soil or backfill surrounding the pipes potentially leading to the occurrence of sinkholes and loss of structural stability (see paragraph 5.6). Similarly, one should also avoid directing downspouts from buildings to sanitary sewer systems as this may severely overload the capacity of the system, possibly leading to backwater conditions and flooding of buildings with diluted wastewater.

All combined, keeping flows of different quality separated and avoiding untreated discharge into either surface waters or groundwater bodies necessitates the absence of:

- cross-connections or inadvertent connections from downspouts, and
- the uncontrolled exchange of water between UD systems and surface or groundwater bodies.



### 5.9.2 Infiltration and exfiltration

Many NBS rely on infiltrating runoff into groundwater bodies. As discussed in Sections 5.2 and 5.3, the clogging process can be characterized by the interception of fine sediments and associated pollutants in the top layers of the infiltration system, which needs to be removed on a regular basis. A further precaution is to ensure no inadvertent cross-connections occur, that is, the discharge of wastewater into NBS should be avoided.

In the case of 'classical' UD systems (i.e., sanitary sewers, storm sewers or combined sewer systems) infiltration and exfiltration can cause a significant loss of functionality.

Causes of infiltration and exfiltration are related to the occurrence of cracks, or faulty joints (e.g., figure 5.50) caused by structural overloading and or subsidence. Generally speaking, infiltration is easier to detect and quantify compared to exfiltration. The reader is referred to Chapter 4 for methods to detect and quantify infiltration and exfiltration.

### 5.9.3 Leakage (exfiltration) of pressurised systems

#### 5.9.3.1 Introduction

Pressure mains can be used to transport collected wastewater to Wastewater Treatment Plants. Due to subsidence, traffic loads or corrosion, leakage from these systems may occur. In many cases, the leakage or exfiltration is only manifested when massive soil erosion and damage at the surface become visible (Figure 5.51). Fortunately, the situation illustrated by Figure 5.51 is relatively rare, but it provides a good impression of the risks to the public when sewer pipes are in a poor condition. Often, it has been suspected that such catastrophic event was precipitated by a small leakage due to for example, corrosion. When inspecting pressure mains, the determination of potential 'weak spots' can be facilitated by knowledge of:

- The soil types and indication of uneven subsidence or subsidence rates (e.g., when the soil type changes from peat to sand or clay).
- The location where pressure mains cross main roads (i.e., traffic load) or street car/railway tracks.
- The location where air or gas pockets and associated corrosive conditions (e.g., due to  $H_2S$ ) may be expected (see Section 5.8.3.3).
- The location where materials were changed used during construction, for example, connections between cast iron and HPDE sections.



Figure 5.50 Infiltration of groundwater due to a defective joint (Deltares).





**Figure 5.51** Car is completely 'swallowed' in a sink hole that occurred due to a collapse sewer pressure main. (Photo by C. de Haan).

The time scale of the involved processes varies: subsidence may take years to result in leakage, whereas corrosion can cause serious damage in a matter of months when conditions are unfavourable.

In general leakage can be detected at an early stage using a range of methods:

- Field visits/regular inspection of leak detection devices; also possible by application of drones and so on especially looking for wet areas.
- Low and high pressure testing (either with air or with water) of complete pipeline systems allowing for a rough quantification. This method is used in a lot of countries and described in national guidelines when testing a new pipe and is also very relevant for older pipes-can be applied the same. This method can also be derived in daily operation by use of pressure sensors.
- Focussed electrode leak detection
- Testing of (suspicious) individual joints (both from inside and outside)
- The use of tracer experiments, both gas and fluids. These methods facilitate, to a certain extent, the quantification of the amount of leakage and pinpointing its location, albeit at a relatively low resolution determined by the accessibility of the system.
- External Acoustic methods facilitating the identification of the location; however, very small leaks are still hard to pinpoint. See [Almeida \*et al.\* \(2014\)](#) and [Brennan \*et al.\* \(2017\)](#) for leak noise correlations.
- Infrared inspections
- FBG-time domain reflectometry (TDR) ([Fatemi Aghda \*et al.\*, 2018](#)).
- Distributed temperature sensing (DTS), see also Chapter 4.
- Distributed strain sensing (DSS) (see e.g. [Zhang \*et al.\*, 2019](#)).
- Distributed acoustic sensing (DAS) (see e.g. [Stajanca \*et al.\*, 2019](#)).
- Acoustic based methods (e.g., smartball).
- Pigging/other internal inspection in in dry and wet situation; by use of different methods (CCTV, radar, infared, acoustic and conductivity).

It is important to keep in mind is that leakage can also be prevented by searching for local surface or pipe settlement, and deterioration of pipe material and joints and vice versa; leakage is only one aspect and cannot be seen apart from other aspects.

A disadvantage of the TDR, DTS, DAS and DSS methods is that wires need to be installed, preferably during the initial construction. Doing so for existing installations is mostly not an option. Therefore, UD owners are well advised to consider doing so for newly built installations, as these methods allow for a relatively easy and almost continuous monitoring of leakages. Alternatively application of a towed acoustic sensor, like the smartball system, does not require the installation of wires, an additional advantage of such a method is that the presence of air/gas pockets can be detected as well.

In [Section 5.9.3.2](#), a case study is presented that illustrates (combinations of) the processes leading to either leakage, surface damage or collapse. In addition to physical/chemical processes, the following factors contribute as well to incidents concerning pressure mains:

- Incorrect or not up-to date information in the AM systems.
- Damage incurred during construction (see also [Section 5.4](#)).
- Damage incurred due to construction activities in the direct vicinity of the pressure main (so-called ‘Third party intrusions’)

### 5.9.3.2 A case study on pressurized systems

#### 5.9.3.2.1 General

In the city of Rotterdam, The Netherlands, an extensive system of pressure mains is used to transport wastewater from mainly combined sewer systems to WWPTs. [Figure 5.52](#) shows part of the tracing of one of these pressure mains with some lengths of pipe supported by a pile foundation as a function of the bearing capacity of the soil. The pipeline crosses above the tunnel of the metro and also contains a siphon to pass under a canal. The pressure main contains two high points at which manholes, aerators and vents are present. The system contains aerators and vents at various locations: when the pressure main is not operated, they allow air into the system. In the case of failure, they can cause siphoning of the pipe, through which water may enter from the adjacent river during high river and sea levels. The system was built in 1940 and prior incidents had been reported: a civilian noticed ‘water coming out of the street’ which was reported to the municipality. It was decided to excavate the pipe, but no problem was identified at the time of the visual inspection. Since the reported water had disappeared, it was decided to rebury the pipe. A few weeks later a similar call came in; this time it was noticed that the street had subsided by a few centimetres, sand has flushed out of the construction.

#### 5.9.3.2.2 Environmental aspects

The pipeline runs through an urban area with a lot of infrastructure and a variety of street level changes: an intersection with a waterway where the pipeline is near a bridgehead and a passage of three dykes, one of which is a primary flood defence. In addition, the pipeline crosses a metro tunnel and many cables and other underground infrastructure (e.g., water supply and gas supply). Taken all these conditions and circumstances into consideration, the system is to be regarded as a hotspot in terms of consequences of failure and should therefore be scrutinized.

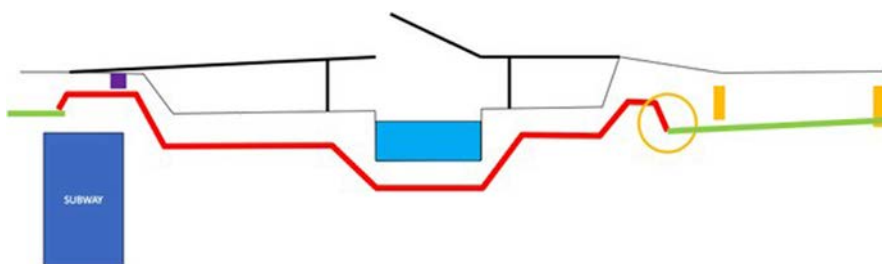


**Figure 5.52** Schematic impression of the vertical tracing of a pressure main, red = pile foundation, green = no pile foundation and dark blue = subway, orange = manhole, the circle indicates the location of the incident.

### 5.9.3.2.3 Emergency plan

The municipality has a process plan in which roles and responsibilities are laid out; however, it is recognized that improvement may be needed, see the discussion of a recent event below under 'Failure history'. Important points for attention are the moment of signalling the field operations staff and the availability of a file with information about the environment (i.e., the pipes and foundation method).

### 5.9.3.2.4 Failure history

Due to uneven settlement, the joint at the transition from the not supported to the supported pressure main had failed (see Figures 5.52–5.54). This is an example (occurred in 2013) of failure occurring at the transition from cast iron elements. Similar incidents with this type of pipes had occurred in the past. In almost all cases, (uneven) settlement was suspected to be the primary cause. In a few cases, it decreased the quality of the joint; the rope used in the seal between pipe sections had dried out. The cast iron pipe itself, however, had not failed (i.e., no cracks or holes due to corrosion were observed).

Over the course of time uneven subsidence of the soil in the direct vicinity of the pressure main had occurred (as illustrated in Figure 5.55).

This case illustrates the added value of monitoring the evolution of known, or suspected, failure mechanisms for critical infrastructure. The city of Rotterdam monitors the performance of its pressure mains in considerable detail as it pertains to hydraulic performance (see e.g., Korving, 2004 or Duinmeijer, 2020). Monitoring of the (rate of) subsidence may add to the early detection of potential critical situations and allow for preventive action. A further important lesson is that citizen calls that may somehow be related to critical infrastructure ask for more than normal attention, as the initial call related to 'water on the street' was, in retrospect, an early warning of a joint giving way, which had not been noticed initially. Monitoring such events can provide valuable information for future cases and may help shape protocols for tracking down locations where deterioration processes are occurring.

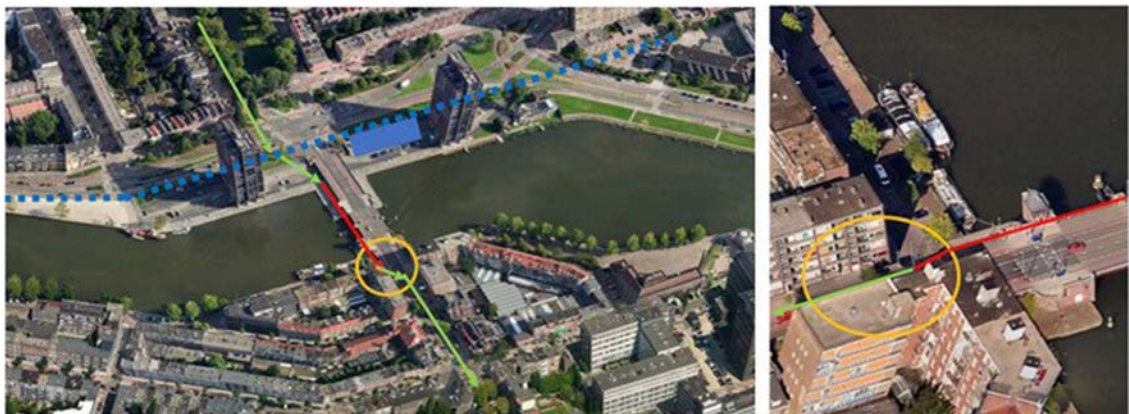


**Figure 5.53** Aerial photo of the situation, the red and green line indicates the alignment of the pressure main, the blue line indicates the alignment of the underground metro, the circle indicates the location of the incident. (Courtesy by C. de Haan).



**Figure 5.54** Example of a joint that has given way. The pipes were pushed about 13 cm apart leading to a leaking joint. (Photos by C. de Haan).





**Figure 5.55** Observed subsidence of the soil, the blue line indicates the location of the pressure main, the red area indicates the location of the incident, the coloured dots indicate the observed subsidence rate of the soil (red = between  $-46$  and  $-10$  mm/year, the green dots between  $-3$  and  $+4$  mm/year the blue dots between  $+11$  and  $+20$  mm/year) As can be seen the differences in subsidence rate in the indicated area are quite high: up to 50 mm/year).

### 5.9.4 Wrong connections

Misconnections, or wrong connections, cross-connections, or illicit connections are terms indicating the occurrence of premises or locations where wastewater is (unintentionally) discharged wastewater into the public stormwater system, or vice versa, where stormwater runoff is discharged into the sanitary sewer system. In both cases the functionality of the systems is corrupted.

In many cases stormwater runoff is either directly, or after a simple or more sophisticated purification step, discharged into open water courses, is infiltrated to replenish aquifers, or is used as (usually non-potable) water source. As discussed in Section 6.4 many stormwater systems display a significant wastewater signature. Needless to say, the discharge of wastewater or polluted runoff into such systems directly affects its water quality and may give rise to odour complaints from residents as stormwater systems are normally not equipped with odour control measures. In addition, it may negatively impact public health where this stormwater is used for other purposes, see Section 6.2. The case of discharging stormwater runoff into a sanitary sewer system has negative repercussions as well, albeit primarily affecting flood risks and increasing the operational costs of transport and treatment. To a certain extent, allowing some stormwater runoff into a sanitary system at its most upstream terminals to ensure frequent flushing velocities may be good practice; however, when the contributing area increases above a certain threshold, regular flooding of the sanitary system may occur. This is obviously not in compliance with one of the main premises of sanitary system practice, that is, preventing people from getting in direct contact with wastewater. The occurrence of



wrong connections is in most cases due to human errors or negligence. During construction of new developments or reconstruction activities mistakes are made in connecting downspouts and storm service connections to sanitary pipes and vice versa. Despite efforts to track down wrong connections after construction, estimates of percentages of wrong connections vary enormously between case studies with values from 1% up to 25% reported (Ellis & Butler, 2015). Without regular preventative actions this percentage is likely to increase over time due to reconstruction activities within homes and apartment buildings. These reconstruction activities are in many cases DIY projects; hence, the application/enforcement of professional standards and quality checks may be largely lacking. To the authors' knowledge no data have been published on the rate at which wrong connections increase, but it is likely to be an unpredictable process as reconstruction activities and people's mobility (linked to reconstruction) depend on a wide range of (economical) factors. A plethora of methods has been developed and is being applied to detect and localise misconnections:

- DTS (Hoes *et al.*, 2009) for wastewater discharged into storm water sewers.
- Smoke methods (for stormwater into wastewater systems, Gokhale & Graham, 2004).
- Acoustic methods (for stormwater into wastewater systems, SAHARA system, Rizzo, 2010).
- Conductivity (Deffontis *et al.*, 2013).
- Chemical analysis (Panasiuk *et al.*, 2015).
- Tracers (Lepot *et al.*, 2016).
- Infrared camera system (Lepot *et al.*, 2017).

More recently, the application of a network of simple low-cost sensors was reported as a means for detecting illicit connections using temperature and conductivity sensors (Shi *et al.*, 2022).

## 5.10 STATISTICAL MODELLING OF AGEING PROCESSES

### 5.10.1 Introduction

Since the 1980s many organizations managing UD systems have created large scale inventories of the technical status of their assets using visual inspection (mainly through CCTV techniques). As discussed in Chapter 4, guidelines and norms exist to apply standardized methods to classify observed defects using video footage. Over the last few decades some organizations have managed to build a comprehensive database of those elements in their UD systems that have been inspected multiple times over the course of time, potentially allowing them to identify the speed of the deterioration processes.

It is implicitly assumed that the conditions between inspections were identical and that all processes happened at a constant process speed over time. In addition, note that defect classification, as for example, defined in the EN 13508-2 (2011) has no quantifiable relation to loss of functionality.

A rather abundant literature has been dedicated to sewer deterioration modelling since the end of the 1990s. Sound reviews of these research works may be found in Ana and Bauwens (2010) and El-Housni *et al.* (2018). Two broad categories of modelling approaches can be distinguished: physical and probabilistic-statistical models.

### 5.10.2 Physical deterioration models

Physical deterioration models mainly focus, at the pipe element scale, on the physico-chemical processes of deterioration, involving varying combinations of load stresses and pipe material corrosion. Physical deterioration models can be either fully deterministic or include a probabilistic aspect as in the limit state concept. The real-world application of physical models is however limited by the impossibility to get precise measurements of the physico-chemical conditions within the entire sewer network and, consequently, by our ignorance of the deterioration factor values needed for the calculations. Research activities in the field of physical deterioration models are nevertheless far from being useless since they can provide guidance as to the choice and design of explanatory factors in the creation of

the probabilistic-statistical models. Previous studies emphasized cross-relationships effects involving the pipeline geometry (e.g., the length, height and width of elements) and environmental factors such as the location (e.g., under roadway versus under a sidewalk or green space), the pipe depth and the traffic intensity.

### 5.10.3 Probabilistic-statistical deterioration models

Probabilistic-statistical deterioration models seek to explain, and then to predict, the probability that a given sewer element with given characteristics (i.e., their age, material, size, depth, slope, effluent type and so on) belongs to a condition class. These models formally depend on parameters that should be, for operational applications, statistically estimated from sewerage utility data.

Probabilistic-statistical deterioration models can, in turn, be divided into two main types, reflecting the particular role assigned to time, and more precisely the age of the sewer pipes, allowing one to distinguish:

- classification models, for which the sewer age is a deterioration factor like any other, and
- stochastic processes that structurally depend on the sewer age by considering the deterioration speed.

These two approaches are illustrated in the remainder of this section with the help of typical examples composed of multinomial logistic regression (MLR) models and Markov chains (MC), respectively.

### 5.10.4 Multinomial logistic regression models

Multinomial logistic regression (MLR), as presented in the reference book 'Generalized Linear Models' (McCullagh & Nelder, 1989), provides the canonical framework for studying phenomena formalized by a random variable (RV), the distribution of which is multinomial. The condition class assigned to a given sewer pipe following its inspection is considered as a random variable denoted  $Y$ , which takes its possible values as per a discrete set of integers  $J = \{1, 2, \dots, C\}$ , which represent the various condition classes, ordered from best (e.g., 1 = 'as good as new' to worst (e.g.,  $C$  = 'rehabilitation urgently needed'). The condition class probabilities  $p_j(\mathbf{Z}) = \Pr[Y = j | \mathbf{Z}]$ ,  $j \in J$  are assumed to depend on pipe characteristics (or functions of them), gathered within the 'covariate' vector  $\mathbf{Z}$ , which are then considered as 'deterioration factors'.

Since the condition classes are ordered it is preferable, according to McCullagh and Nelder (1989), to consider the cumulative probabilities  $\pi_j(\mathbf{Z}) = \Pr[Y \leq j | \mathbf{Z}]$ ,  $j \in J$ , with  $\pi_C(\mathbf{Z}) = 1$ . The condition class probabilities are then calculated by their difference:  $p_j(\mathbf{Z}) = \pi_j(\mathbf{Z}) - \pi_{j-1}(\mathbf{Z})$ , which ensures  $\sum_{j \in J} p_j(\mathbf{Z}) = 1$ .

The key feature of MLR consists of mapping  $\pi_j(\mathbf{Z}) \in ]0, 1[$  onto  $g(\pi_j(\mathbf{Z})) \in ]-\infty, +\infty[$ , by using the so-called 'logit' transform  $g(\pi) = \ln(\pi/(1 - \pi))$ , which allows one to adopt the linearity hypothesis:  $g(\pi_j(\mathbf{Z})) = \alpha_j + \mathbf{Z}^T \beta$ , where  $j \in \{1, 2, \dots, C - 1\}$ . The vectors  $\alpha = (\alpha_j)_{j \in J}$  and  $\beta$  are regression parameters to be estimated from observed data; the  $\alpha_j$ 's estimates must satisfy the inequality constraints  $\alpha_1 < \alpha_2 < \dots < \alpha_{C-1}$  to ensure  $p_j(\mathbf{Z}) \in ]0, 1[$ , by preventing the graphs of the  $\pi_j(\mathbf{Z})$ 's from intersecting. This theoretical construct is typical of generalized linear models in that:

- unlike simple linear models, it is not the response RV value itself that is modelled but the probability of this value; this has the crucial consequence that parameter estimation cannot proceed by minimizing a sum of squared deviations between observed and predicted response values; and
- the linear effect of covariates on the response RV is ensured via an adequate transformation.

Additionally, the analytical form  $g(\pi_j(\mathbf{Z})) = \alpha_j + \mathbf{Z}^T \beta$  makes the covariate effects independent of the condition class while the regression intercepts are assumed to solely depend on it (i.e., 'parallel regression' hypothesis).

As discussed earlier, estimating the model parameters  $\theta = (\alpha, \beta)$  cannot be conducted using a least squares minimization method. A more general estimation method is needed, based on the ‘maximum likelihood’ concept. This involves defining a likelihood function  $L(\theta|E)$  that quantifies how likely a parameter value  $\theta$  is, given a set of  $n$  observations (i.e.,  $n$  sewer segment inspections)  $E = \{(y_i, \mathbf{Z}_i); i = 1, \dots, n\}$ , where  $y_i$  stands for the  $Y$  value at observation  $i$ . ‘Maximum Likelihood Estimation’ consists of numerically determining the ‘optimal’ value  $\theta_{\text{opt}}$  that maximizes  $L(\theta|E)$ . The adequate MLR likelihood function is simply defined as the product of probabilities  $L(\theta|E) = \prod_{i=1, \dots, n} \Pr[Y = y_i | \mathbf{Z}_i]$ . In practice, rather the natural logarithm  $\ln L(\theta|E)$  is considered since it involves a summation which is numerically more tractable than a product. According to the authors’ experience, the so-called ‘Nelder-Mead simplex’ method, proposed by [Nelder and Mead \(1965\)](#) can be used to maximize the MLR log-likelihood, although a wide spectrum of optimisation algorithms is presently available, see for example, [Bazaraa et al. \(2013\)](#).

The definition of  $L(\theta|E)$  above assumes, however, that the  $n$  observations are mutually independent of each other. In the case where the data set  $E$  concerns pipes inspected repeatedly, this independence assumption is no longer valid, and the model can be refined by adding a pipe-specific random effect to the linear combination  $\mathbf{Z}^T \beta$ ; the MLR model is then turned into a ‘mixed’ MLR (i.e., considering a mixture of fixed and random effects), which requires an adapted likelihood maximization method such as the so-called ‘Expectation-Maximization’ method, proposed by [Dempster et al. \(1977\)](#).

Classification tools such as the MLR presented above are generally considered efficient for predicting which sewer pipelines are likely to be the most deteriorated within the short term (i.e., within the next year or next two years) that can then be used in scheduling inspection activities. These models are however not designed to explicitly account for the increase in deterioration as a function of the ageing of the assets. They can therefore not be used in performing mid- to long-range simulations of the evolution of the condition of a set of sewer segments that compose a sewerage network, given that they are subject to various imposed constraints such as a pipe renewal budget and the interaction with the rehabilitation strategy of other, third-party infrastructure (particularly roadways). Markov chains were developed to fill this gap; they are discussed in the next section.

### 5.10.5 Markov chains

Following previous research works dedicated to deterioration modelling of engineering structures such as bridges and roadways, the mathematical theory of probabilistic Markov chains was recognized from the beginning as a relevant approach ([Madanat et al., 1995](#)).

In the context of sewer deterioration, the theoretical development of Markov chains can be seen as an adaptation of the MLR model with the aim of endowing it with appropriate properties expected of ageing models.

A Markov chain is a stochastic process formalized by a random variable (RV)  $Y(t)$  that structurally depends on time  $t$ , namely the age of the sewer main. It should however be emphasized that, for a fixed age, the variable has the same multinomial distribution as that presented in the case of the classification models: the RV  $Y(t)$  takes its values on a discrete state space, the elements of which are usually formalized by a set of integers, such as  $J = \{1, 2, \dots, C\}$  ( $C$  is in usual applications a small finite integer, such as 4 or 5, but it could also be theoretically considered as infinite). Markov chains have the characteristic property of being memoryless, which means that the state reached at the next time step depends only on the current state (i.e., having a ‘Markovian’ property).

The time dimension can either be discrete, that is,  $t \in \mathbb{N}$ , in which case the MC is said to be a ‘Discrete Time Markov Chain’ (DTMC), or continuous, that is,  $t \in \mathbb{R}_+$ , and the MC is then called a ‘Continuous Time Markov Chain’ (CTMC). These two classes of Markov chains will be presented successively, with for each an example of construction usable in practice. At the practical level, for both MC classes, the parameter calibration is confronted with the scarcity of sewer inspection data, leading to the

impossibility of precisely dating the transitions between condition states. It is then pertinent to design a calibration procedure rather based on the state probabilities and build a likelihood function such as that used in MLR.

5.10.6 DTMC

The state of a DTMC is formalized at any age  $t$  by the state probability vector:  $\mathbf{p}(t) = (\Pr[Y(t) = j])_{j \in J}$ , and its evolution over time, that is, when the system ages, it is governed in the most general case by a time-dependent square  $C \times C$  matrix of transition probabilities  $\mathbf{Q}(t) = (q_{ij}(t))$ , with  $q_{ij}(t) = \Pr[Y(t) = j | Y(t-1) = i]$  which only depends on the current state  $Y(t)$ , and not on the MC process trajectory  $Y(s)$ ,  $s \in \{0, 1, \dots, t-1\}$ . If the transition probabilities do not depend on time, the MC is said to be ‘homogeneous’ (HDTMC), and ‘non-homogeneous’ (NHDTMC) otherwise.

In the rather general case of a NHDTMC, the development of condition state probabilities is governed by the relationship:  $\mathbf{p}^T(t+s) = \mathbf{p}^T(t) \prod_{k=1, \dots, s} \mathbf{Q}(t+k)$ ,  $\forall t \in \mathbb{N}, \forall s \in \mathbb{N}^*$ . In the HDTMC case, this relationship simplifies to  $\mathbf{p}^T(t+s) = \mathbf{p}^T(t) \mathbf{Q}^s$ .

A practical DTMC construct can empirically start from the observation that the graph of the cumulative probability  $\pi_j(t; \mathbf{Z}) = \Pr[Y(t) \leq j | \mathbf{Z}]$  vs age  $t$  has most often a decreasing sigmoid shape. A simple transition matrix  $\mathbf{Q}(t)$  can be designed by assuming that, in a unit time step  $\Delta t = 1$ , a sewer pipe can only either stay in the same condition state  $j$ , with probability  $q_j(t+1)$ , or jump into the adjacent more deteriorated state  $j+1$ , with complementary probability  $1-q_j(t+1)$ , which is calculated as  $[\pi_j(t)-\pi_j(t+1)]/p_j(t)$ . This simple DTMC is illustrated by Figure 5.40. Usual sigmoid functions lead to an age-dependent transition matrix (NHDTMC). An example of such a construct is the GompitZ model presented by Le Gat (2008); the analytical form is  $\pi_j(t; \mathbf{Z}, u) = \exp[-\exp(\alpha_j + t \exp(\mathbf{Z}^T \beta + u))]$ , designed to prevent the cumulative probability curves from intersecting, and the condition state from improving with age. It also accounts for the pipe-specific frailty via the random effect coefficient  $u$ ; this model can also be viewed as a generalized linear mixed model.

5.10.7 CTMC

In the case of a CTMC the transition probabilities are replaced by transition rates, which are either time-dependent  $\tau_{ij}(t) = E[dY(t) = j-i | Y(t) = i]$ , in the case of a ‘non-homogeneous’ CTMC (NHCTMC, see Figure 5.56), or independent of time  $\tau_{ij}$ , in the case of a ‘homogeneous’ CTMC (HCTMC).

A construction like that of the GompitZ model is possible in continuous time, and is the subject of ongoing research work, which is briefly discussed here. It is more practical in continuous time to consider transition rates independent of pipe age, and then to build a HCTMC, as illustrated by Figure 5.57. In this kind of construct, the deterioration rates can be designed in a ‘proportional hazard’ manner, as  $\eta_j = \exp(\alpha_j + \mathbf{Z}^T \beta)$ . It is easy to account for pipe decommissioning by adding an absorbing ‘decommissioned’ state, fed by decommission rates  $\rho_j$ , which are the product of inspection rates and conditional probabilities of decommissioning given the pipe was observed in this or that condition state. Considering such an absorbing ‘decommissioned’ state allows for accounting in a ‘natural’ manner for the right censoring of the deterioration process due to pipe decommissioning, which rarefies the observation of the most deteriorated state. As the decommissioned state is unobserved at the pipe inspection, the condition probabilities to be considered when building the likelihood function

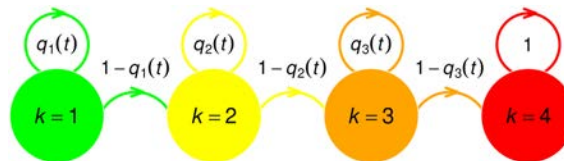
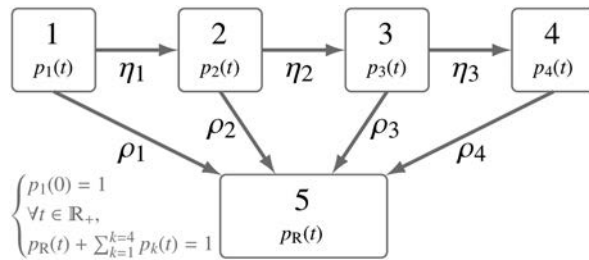


Figure 5.56 Illustration of a simple NHDTMC with C = 4 possible condition states, the 4th being absorbing.



**Figure 5.57** Illustration of a simple HCTMC with  $C = 4$  possible condition states, and a 5th state that stands for decommissioned pipes and is absorbing.

are  $p_j^*(t; \mathbf{Z}) = p_j(t; \mathbf{Z}) / \sum_{k=1, C} p_k(t; \mathbf{Z})$ , which allows one to account for the selective survival phenomenon. These questions of informative censoring of pipe inspections, and pipe cohort truncation due to the selective survival phenomenon, are discussed in more detail in Chapter 8 of this book.

## 5.11 APPLICATION OF MACHINE LEARNING BASED MODEL

Artificial intelligence-based models, such as machine learning models, for sewer deterioration modelling differ from statistical models as they do not require any assumptions on the model structure (Tscheikner-Gratl *et al.*, 2019). These models are known to be data-driven, as the mathematical relationship between the factors affecting the deterioration and condition class of the sewer pipe are constructed by ‘learning’ the deterioration process from data obtained during sewer inspection (Hawari *et al.*, 2020). The strength of machine learning models over statistical models is their capability to handle complex relationships between variables that are difficult to describe using statistical models (Ana & Bauwens, 2010). On the other hand, machine learning-based models have the disadvantage of being ‘black boxes’, meaning that the internal processes are somewhat unknown (Tu, 1996). Additionally, machine learning-based models requires a substantial amount of computational power and have a high demand of data to be trained on. The latter has an impact on utilities who lack condition data of their sewer systems, typically smaller utilities (e.g. Chen *et al.*, 2022; Jenkins *et al.*, 2015; Kabir *et al.*, 2020).

As one of the goals of a sewer deterioration models is to predict the condition of sewer pipes that have not yet been inspected by using inspection data from other pipes (Harvey and McBean, 2014b), the machine learning algorithms need to be able to learn from a set of input with a given output. Within the machine learning field of supervised learning, this is known as classification (Géron, 2019). In sewer deterioration modelling, the input will be the desired physical, environmental or operational factors that could describe the deterioration process (Hawari *et al.*, 2017), and the output would be the corresponding condition class, based on the inspected data used in the model.

Several algorithms for doing classification problems exist the most common are described in some detail by Géron (2019). Regarding sewer deterioration modelling, many of these algorithms have been applied in various studies, from the simple structures as decision trees (e.g. Harvey and McBean, 2014a) and random forest (e.g. Rokstad and Ugarelli, 2015), to the more complex structures of artificial neural networks (Atambo *et al.*, 2022). Before looking deeper into the use of the different algorithms for sewer deterioration modelling, the most commonly utilized algorithms will be briefly introduced by their strengths and weaknesses.

Géron (2019) gives a detailed description of decision trees, and their main strength is that they are powerful and capable of fitting complex datasets, and they are able to perform both classification and regression tasks. The most common way of implementing decision trees is by the algorithm CART, which is an abbreviation for classification and regression tree and is developed by Breiman



*et al.* (1984). Additionally, to being powerful, decision trees are also easy to understand and to use. However, the main issues when using decision trees is that they are very sensitive to small changes in the dataset used for training (Pedregosa *et al.*, 2011), and they are known to be easily overfitted to the data (Kotsiantis, 2013).

The random forest algorithm is developed by Breiman (2001), and is based on grouping a number of decision trees in an ensemble which reduces the chance of overfitting due to the law of large numbers. The algorithm grows multiple decision trees, known as a forest, where the class that gets the most votes at the end is the resulting prediction. By using these votes, it is possible to calculate the probability of belonging to a given class (Rokstad and Ugarelli, 2015). The random feature of the algorithm is implemented by using so-called bagging or bootstrap aggregating (Breiman, 1996, 2001). This is done by training each decision tree of the forest on a randomly selected subset of the training data, and a random selection of input variables are used at each node of the tree.

Another commonly used algorithm is support vector machine (SVM), based on the work of Cortes and Vapnik (1995). The concept of the algorithm is to map the input variables onto a high dimensional feature space, where a linear decision surface is constructed. To do this mapping, so-called kernel functions are used (Shawe-Taylor & Cristianini, 2004). Typical available kernel functions are linear, polynomial and radial basis function. The goal of SVM is to find the optimal hyperplane that maximizes the separation between the classes, but also generalize well, that is reduce overfitting (Cortes & Vapnik, 1995). SVM are very well suited for classification on complex, but small- or medium-sized datasets, but they are very sensitive to adjustments of the hyperparameters (Géron, 2019).

Artificial Neural Network (ANN) is a type of algorithm that tries to mimic the performance of the human nervous system (Al-Barqawi & Zayed, 2008). The composition of ANNs is consisting of artificial neurons that are connected to each other in different layers, with the aim of mimicking the ability of the human brain to recognize patters and using these to predict outcomes based on its observations. The neurons are linked together with connections having a certain weight (Fausett, 1994). For a given input, the associated weights are summed up and the neurons send a signal to identify the activation function, when the sum of weights reaches a certain threshold value. The most common neural network used for deterioration modelling is the back-propagation neural network (BPNN) (Hawari *et al.*, 2020; Tran *et al.*, 2007; Zeng *et al.*, 2023). Figure 5.58 shows the layout of a BPNN used for sewer deterioration modelling, where each circle represents a neuron, the lines indicate where the connection weights are located. The goal of the BPNN is to tune the connection weights so that the error between predicted condition class and actual condition class is minimized.

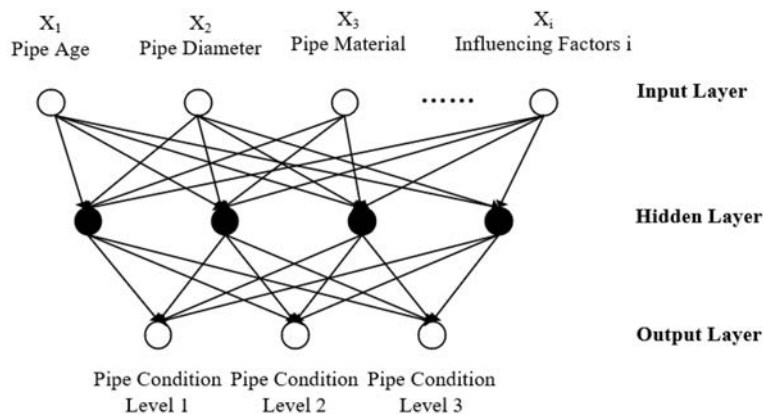


**Figure 5.58** Schematic presentation of a BPNN for sewer deterioration modelling. (After Zeng *et al.* (2023).

The strength of ANNs is that they are very powerful and scalable, making them suitable for large and complex machine learning tasks (Géron, 2019). Still, they have their limitation as the underlying processes are hidden, making it difficult to really understand how the model works (Tran *et al.*, 2007).

To address the predictive power of a machine learning classifier, several metrics exist (Géron, 2019). A visual representation is often provided by presenting the predicted condition versus the actual condition in a confusion matrix. This gives an overview of the amounts of correct and incorrect predictions. The goal of a classifier is to predict good pipes as good and bad pipes as bad, meaning that the number of incorrect predictions should be as close to zero as possible (Harvey & McBean, 2014b). Accuracy is commonly used as a performance metric, which is defined as the number of correct predictions divided by the total number of predictions. Still, using accuracy solely to measure the performance is unsuitable for imbalanced datasets, where a high accuracy does not necessarily mean that the model is good at predicting (Géron, 2019; Harvey & McBean, 2014b). As this often is the case for sewers, where the number of pipes in good condition is higher than the number of pipes in bad condition, other measures should be used. A commonly used method is to plot the True Positive Rate (TPR) as a function of the False Positive Rate (FPR) by using different probability cut-offs (Géron, 2019). TPR is calculated as the number of correctly predicted good pipes over the total number of good pipes, while FPR is the number of bad pipes predicted as good over the total number of bad pipes. The resulting plot is known as the receiver operating characteristic (ROC) curve and is shown in Figure 5.59. A measure that can be extracted from the ROC curve is the area under the curve, known as AUC, where a score equal to 1 is a perfect model and a score equal to 0.5 is a random model. An AUC score above 0.7 is by Hosmer and Lemeshow (2000) considered a good model.

All the mentioned machine learning models have been applied for sewer deterioration modelling in several studies over the years. Harvey and McBean (2014a) compared two deterioration models in their study, one Decision Tree model and one SVM model, using data from the municipality of Guelph in Ontario, Canada. The decision tree model had an accuracy of 76%, and an AUC score of 0.78, which was a significantly higher accuracy than the one of the SVM model (58%), while the AUC score was more similar between the two models. Syachrani *et al.* (2013) also used a Decision Tree model, which they compared with a regression model and an artificial neural network on data from Johnson County Wastewater in Kansas, USA. The findings of the study were that the decision tree model consistently outperformed the other models.

As earlier mentioned, decision trees are models who are easily overfitted, and the use of random forest has been more usual. Harvey and McBean (2014b) used a random forest model with different

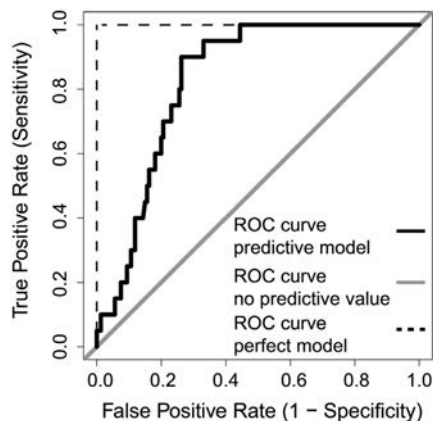


Figure 5.59 Example of ROC curve. (After Harvey & McBean, 2014b).

probability cut-offs (i.e., threshold for when a pipe is classified as bad or good), on the dataset from Guelph, achieving accuracies of 72%, 74% and 89%. All models gave the same AUC score, but the latter model favoured classifying pipes as good, failing to find the bad pipes. By intuition, having a deterioration model that can find the bad pipes is more useful than one who fails to find them. This states the fact that using a single performance measure when evaluating a model is unfavourable. [Rokstad and Ugarelli \(2015\)](#) compared a random forest model with the statistical GompitZ model ([Le Gat, 2008](#)) on sewer data from Oslo, Norway, where the random forest model gave the best predictive accuracy on the network level. [Caradot et al. \(2018\)](#) also compared the same two models on sewer data from Berlin, Germany. Their study showed that random forest performed better in terms of measures such as False Negative Rate, FPR, and their own defined measures  $K_{\text{Network}}$  and  $K_{\text{Pipe}}$ . [Laakso et al. \(2018\)](#) used a logistic regression model and a random forest model on data from the southern Finland, with the former model giving an accuracy of 56% and the latter an accuracy of 62%. [Nguyen et al. \(2022\)](#) compared 17 different algorithms on sewer data from the city of Ålesund in Norway, where the random forest model was ranked the best based on the TOPSIS ranking method. The random forest also yielded the highest accuracy of around 78%, and the highest AUC score (0.776).

[Mashford et al. \(2011\)](#) used SVM models with varying input variables on sewer data from Adelaide, South Australia. In general, the models gave high accuracy, up to 91% at most. [Sousa et al. \(2014\)](#) used SVM in comparison with a logistic regression model and an ANN on sewer data from Lisbon, Portugal. The ANN model gave the best accuracy of 78.5%, with the SVM model having an accuracy of 71.1%. Both models still performed better than the logistic regression model, which had an accuracy of 65.9%. The study of [Hernández et al. \(2021\)](#) looked into optimizing SVM models in the cities of Bogota and Medellin in Colombia. Models for both cities yielded fairly accurate results, giving the best results when optimized for the  $K_{\text{pipe}}$  measure described in [Caradot et al. \(2018\)](#).

The use of ANNs has also been tested in various other studies. In the early twenty-first century, [Najafi and Kulandaivel \(2005\)](#) created an ANN-based sewer deterioration model on data from the city of Atlanta, United States. The model gave a high accuracy score, but it was trained on a relatively small dataset. More recently, [Atambo et al. \(2022\)](#) compared a multinomial logistic regression model against an ANN model on data from the city of Dallas, United States. The ANN model outcompeted the regression model in terms of accuracy, with a score of 85% over 75%. [Nguyen et al. \(2022\)](#) tested three different ANN-based models of the 17 in total they used on the sewer data from Ålesund, Norway. The three ANN models had one, two and three hidden layers respectively, and used different activation functions. Still, they did not rank high on the TOPSIS ranking, with accuracy ranging between approximately 67% and 72%, and AUC scores between  $\sim 0.65$ – $0.69$ .

Even though several algorithms have been tested in various studies, sig datasets of different size and geographical location, no algorithm came out as better than the other in general, analogously described by the ‘No free lunch’ theorem ([Wolpert & Macready, 1997](#)). The ranges of accuracy, AUC score or other performance measures varies both between the algorithms, and also within each algorithm.

## 5.12 CONCLUSIONS AND OUTLOOK

As illustrated in the previous sections, a huge amount of physical and (bio)chemical processes lay at the heart of the loss of functionality of UD systems. In most cases, the loss of functionality occurs gradually and slowly develops over time; however, sudden and catastrophic collapse may occur occasionally. In most cases this is the result of a combination of processes undermining the stability of a core element: an unexpected (traffic) mechanical load may trigger a sudden collapse. A similar thing may be said with respect to the occurrence of sinkholes (which sometimes can be linked to the collapse of pipes or severe leaking of underground pipes). Although the processes tend to be well understood and described at some length and detail in the (scientific) literature, this does not imply that deterioration can be predicted or modelled to the extent of producing reliable forecasts on for

example, the timing of a collapse or the rate at which the hydraulic capacity of a given conduit will decay. The main reasons for this are:

- Many (deterministic) models need a lot of process parameters that should be determined separately for each case, which in most cases is a non-viable option, also given the substantial heterogeneity of for example, material and soil parameters.
- The initial conditions are often not known to the detail needed for reliable modelling.
- The boundary conditions and their development over time are largely unknown and sometimes inherently unknowable, unless monitored over the life span of an element (e.g., stormwater runoff loadings, the composition of wastewater, traffic loads, changes in the daily management of the system and so on).

For long-term assessments on relatively large cohorts of elements (i.e., at the scale of an entire catchment or urban area) statistical/data driven models based on condition class data seem to present a useable tool, at least at a large spatial scale and mid- to long-term planning (i.e., >five years). These models, however, lose their predictive power when applied at the scale of a single element or for a small number of elements and short-term ‘prediction’ horizons. This implies in practical situations, when a decision must be made to replace or rehabilitate a given element, no tools are available to reliably estimate a ‘deadline’ for action. In such a case, a sound understanding of the processes and their characteristic timescales responsible for the given situation comes at hand. The latter highlights the real value of detailed models of the processes responsible for deterioration: appreciating the concept ‘model’ as a means to understand the processes and as tool to get a ‘feeling’ for the process characteristics instead of expecting exact ‘predictions’. These models can be of value in decision making, while the understanding of the processes involved is crucial in deciding what and how to monitor to keep track of a developing situation and/or formulate actions to remove or mitigate the cause of the process or slow the deterioration process down. For example, forced degassing combined with forced ventilation and a proper material selection are measures taken during design and operation to reduce/avoid bio sulphuric corrosion.

Regular monitoring of the hydraulic performance of UD systems using high-quality hydrodynamic models as a reference has shown to be able to identify capacity loss due to, for example, sedimentation or the occurrence of obstacles. Further, process knowledge and estimates of the temporal and spatial scales at which these occur can be instrumental to identify locations in systems that are sensitive to certain deterioration processes. This, in turn, can be used as a guide for monitoring. Generally speaking, organizations responsible for UDAM are encouraged to incorporate monitoring options when building new systems, like, for example, wiring pressure mains to allow for regular leakage testing using distributed sensing technologies.

## REFERENCES

- Alabtah F. G., Mahdi E. and Eliyan F. F. (2021). The use of fiber reinforced polymeric composites in pipelines: A review. *Composite Structures*, **276**, 114595, <https://doi.org/10.1016/j.compstruct.2021.114595>
- Alakayleh Z., Fang X. and Clement T. P. (2019). A comprehensive performance assessment of the modified Philip–Dunne infiltrometer. *Water*, **11**, 1881, <https://doi.org/10.3390/w11091881>
- Al-Barqawi H. and Zayed T. (2008). Infrastructure management: integrated AHP/ANN model to evaluate municipal water mains’ performance. *Journal of Infrastructure Systems*, **14**(4), 305–318. Scopus, [https://doi.org/10.1061/\(ASCE\)1076-0342\(2008\)14:4\(305\)](https://doi.org/10.1061/(ASCE)1076-0342(2008)14:4(305))
- Allahverdi A. and Skvara F. (2000). Acidic corrosion of hydrated cement based materials. *Ceramics-Silik’ aty*, **44**(2000), 114–120.
- Allaire S. E., Roulier S. and Cessna A. J. (2009). Quantifying preferential flow in soils: a review of different techniques. *Journal of Hydrology*, **378**, 179–204, <https://doi.org/10.1016/j.jhydrol.2009.08.013>
- Allroggen N. and Tronicke J. (2015). Attribute-based analysis of time-lapse ground-penetrating radar data. *Geophysics*, **81**, H1–H8, <https://doi.org/10.1190/geo2015-0171.1>

- Almeida F., Brennan M., Joseph P., Whitfield S., Dray S. and Paschoalini A. (2014). On the acoustic filtering of the pipe and sensor in a buried plastic water pipe and its effects on leak detection: An experimental investigation. *Sensors*, 2014, 14(3), 5595–5610, <https://doi.org/10.3390/s10305595>
- Al-Rubaei A. M., Viklander M. and Blecken G. T. (2015). Long-term hydraulic performance of stormwater infiltration systems. *Urban Water Journal*, 12(8), 660–671, <https://doi.org/10.1080/1573062X.2014.949796>
- Ana E. V. and Bauwens W. (2010). Modelling the structural deterioration of urban drainage pipes: the state-of-the-art in statistical methods. *Urban Water Journal*, 7(1), 47–59, <https://doi.org/10.1080/15730620903447597>
- Anderson A. E., Weiler M., Alila Y. and Hudson R. O. (2009a). Dye staining and excavation of a lateral preferential flow network. *Hydrology and Earth System Sciences*, 13, 935–944, <https://doi.org/10.5194/hess-13-935-2009>
- Anderson A. E., Weiler M., Alila Y. and Hudson R. O. (2009b). Subsurface flow velocities in a hillslope with lateral preferential flow. *Water Resources Research*, 45, <https://doi.org/10.1029/2008WR007121>
- Angulo-Jaramillo R., Bagarello V., Iovino M. and Lassabatere L. (2016). Infiltration Measurements for Soil Hydraulic Characterization. Springer International Publishing, Switzerland (eBook), <https://doi.org/10.1007/978-3-319-31788-5>
- Angulo-Jaramillo R., Bagarello V., Di Prima S., Gosset A., Iovino M. and Lassabatere L. (2019). Beerkan estimation of soil transfer parameters (BEST) across soils and scales. *Journal of Hydrology*, 576, 239–261, <https://doi.org/10.1016/j.jhydrol.2019.06.007>
- Ankeny M., Kaspar T. and Horton R. (1988). Design for an automated tension infiltrometer. *Soil Science Society of America Journal*, 52(3), 893–895. <http://dx.doi.org/10.2136/sssaj1988.03615995005200030054x>
- Anton-Prinet C., Mur G., Gay M., Audouin L. and Verdu J. (1999). Change of mechanical properties of rigid poly (vinylchloride) during photochemical ageing. *Journal of Materials Science*, 34, 379–384, <https://doi.org/10.1023/A:1004482328203>
- Archer N. A. L., Quinton J. N. and Hess T. M. (2002). Below-ground relationships of soil texture, roots and hydraulic conductivity in two-phase mosaic vegetation in South-east Spain. *Journal of Arid Environments*, 52(4), 535–553, <https://doi.org/10.1006/jare.2002.1011>
- Arnold J. C. (2003). 6.06 Environmental effects on crack growth in polymers. *Comprehensive Structural Integrity*, 6, 281–319, <https://doi.org/10.1016/B0-08-043749-4/06123-1>
- Ashely R. M., Bertrand-Krajewski J.-L., Hvitved-Jacobsen T. and Verbanck, M. (eds) (2004). Solids in Sewers. Characteristics, Effects and Control of Sewer Solids and Associated Pollutants. Scientific and Technical report No. 14. IWA Publishing, London, ISBN 1 900222914.
- Atambo D. O., Najafi M. and Kaushal V. (2022). Development and comparison of prediction models for sanitary sewer pipes condition assessment using multinomial logistic regression and artificial neural network. *Sustainability (Switzerland)*, 14(9), 5549. Scopus, <https://doi.org/10.3390/su14095549>
- Attiogbe E. K. and Rizkalla S. H. (1988). Response of concrete to sulfuric acid attack. *ACI Materials Journal*, 85, 481–488.
- Azzout Y., Barraud S., Cres F.-N. and Alfakih E. (1994). Techniques alternatives en assainissement pluvial: choix, conception, réalisation et entretien, Technique & Documentation, Lavoisier.
- Balades J.-D., Legret M. and Madiec H. (1995). Permeable pavements: pollution management tools. *Water Science & Technology*, 32(1), 49–56, <https://doi.org/10.2166/wst.1995.0012>
- Barraud S., Gonzalez-Merchan C., Nascimento N., Moura P. and Silva A. (2014). A method for evaluating the evolution of clogging: application to the Pampulha Campus infiltration system (Brazil). *Water Science & Technology*, 69(6), 1241–1248, <https://doi.org/10.2166/wst.2013.819>
- Bazaraa M. S., Sherali H. D. and Shetty C. M. (2013) Nonlinear Programming: Theory and Algorithms. John Wiley & Sons, Inc., New Jersey, USA, ISBN-13: 978-0-471-48600-8
- Bedell J.-P., Saulais M. and Delolme C. (2013). Rôle de la végétation sur l'évolution des caractéristiques physico-chimiques des sédiments déposés dans un bassin d'infiltration des eaux pluviales. *Etude Gest. Sols*, 20, 27–38.
- Bedell J.-P., Hechelski M., Saulais M. and Lassabatere L. (2021). Are acts of selective planting and maintenance drivers for vegetation change in stormwater systems? A case study of two infiltration basins. *Ecol. Eng.*, 172, 106400, <https://doi.org/10.1016/j.ecoleng.2021.106400>
- Belie N. D., Monteny J., Beeldens A., Vincke E., van Gemert D. and Verstraete W. (2004). Experimental research and prediction of the effect of chemical and biogenic sulfuric acid on different types of commercially produced concrete sewer pipes. *Cement and Concrete Research*, 34, 2223–2236, <https://doi.org/10.1016/j.cemconres.2004.02.015>
- Bell J. P. (1976). Neutron Probe Practice. Institute of Hydrology, Wallingford, UK, Rep., 19, 1–63.



- Benjamin P. (1980). The influence of the extrusion process on the quality of unplasticized polyvinyl chloride (UPVC) pressure pipe. *Journal of Vinyl and Additive Technology*, **2**, 254–258, <https://doi.org/10.1002/vnl.730020412>
- Bergman M., Hedegaard M. R., Petersen M. F., Binning P., Mark O. and Mikkelsen P. S. (2011). Evaluation of two stormwater infiltration trenches in central Copenhagen after 15 years of operation. *Water Science & Technology*, **63**(10), 2279–2286, <https://doi.org/10.2166/wst.2011.158>
- Bernatek A. (2015). The influence of piping on mid-mountain relief: a case study from the polish Bieszczady Mts. (Eastern Carpathians). *Carpathian J Earth Environ Sci*, **10**, 107–120.
- Bernatek-Jakiel A. and Poesen J. (2018). Subsurface erosion by soil piping: significance and research needs. *Earth-Science Reviews*, **185**, 1107–1128, <https://doi.org/10.1016/j.earscirev.2018.08.006>
- Bernatek-Jakiel A., Vannoppen W. and Poesen J. (2017). Assessment of grass root effects on soil piping in sandy soils using pinhole test. *Geomorphology*, **295**, 563–571, <https://doi.org/10.1016/j.geomorph.2017.08.027>
- Beryani A., Goldstein A., Al-Rubaei A. M., Viklander M., Hunt W. and Blecken G.-T. (2021). Survey of the operational status of twenty-six urban stormwater biofilter facilities in Sweden. *Journal of Environmental Management*, **297**(2021), 113375, <https://doi.org/10.1016/j.jenvman.2021.113375>
- Beven K. and Germann P. (1982). Macropores and water flow in soils. *Water Resources Research*, **18**, 1311–1325, <https://doi.org/10.1029/WR018i005p01311>
- Beven K. and Germann P. (2013). Macropores and water flow in soils revisited. *Water Resources Research*, **49**, 3071–3092, <https://doi.org/10.1002/wrcr.20156>
- Bielefeldt A., Gutierrez-Padilla M. G. D., Ovtchinnikov S., Silverstein J. and Hernandez M. (2010). Bacterial kinetics of sulfur oxidizing bacteria and their biodeterioration rates of concrete sewer pipe samples. *Journal of Environmental Engineering*, **136**, 731–738, [https://doi.org/10.1061/\(ASCE\)EE.1943-7870.0000215](https://doi.org/10.1061/(ASCE)EE.1943-7870.0000215)
- Bishop S., Isaac D. H., Hinksman P. and Morrissey P. (2000). Environmental stress cracking of poly (vinyl chloride) in alkaline solutions. *Polymer Degradation and Stability*, **70**, 477–484, [https://doi.org/10.1016/S0141-3910\(00\)00144-0](https://doi.org/10.1016/S0141-3910(00)00144-0)
- Blake G. R. and Hartge K. H. (1986). Particle density. In: *Methods of Soil Analysis*, John Wiley & Sons, Ltd, New Jersey, USA, pp. 377–382, <https://doi.org/10.2136/sssabookser5.1.2ed.c14>
- Blecken G.-T., Hunt W. F., Al-Rubaei A. M., Viklander M. and Lord W. G. (2017). Stormwater control measure (SCM) maintenance considerations to ensure designed functionality. *Urban Water Journal*, **14**(3), 278–290, <https://doi.org/10.1080/1573062X.2015.1111913>
- Blecken G., Beryani A., Al-Rubaei A., Viklander M., Goldstein A. and Hunt W. (2021). (Review evaluation of the functionality of 26 stormwater biofilters (*org. title in Swedish: Oversiktlig utvardering av funktionaliteten av 26 dagvattenbiofilter.*) <https://www.diva-portal.org/smash/get/diva2:1841857/FULLTEXT01.pdf>
- Bolderman R., van der Meulen M. and Op de Beek R. M. J. (2003). Riolen van beton, State of the art 2003. Vereniging van Producenten van Betonleidingsystemen VPB, Woerden, the Netherlands.
- Bonelli S., Jommi C. and Sterpi D. (eds) (2018). Internal erosion in Earthdams, Dikes and Levees. Proceedings of EWG-IE 26th annual meeting 2018, Milan, Italy.
- Bonneau J., Fletcher T., Costelloe J., Poelsma P., James R. and Burns M. (2018). Where does infiltrated stormwater go? Interactions with vegetation and subsurface anthropogenic features. *Journal of Hydrology*, **567**, 121–132, <https://doi.org/10.1016/j.jhydrol.2018.10.006>
- Bosch D. D. and West L. T. (1998). Hydraulic conductivity variability for Two sandy soils. *Soil Science Society of America Journal*, **62**, 90–98, <https://doi.org/10.2136/sssaj1998.03615995006200010012x>
- Bosco E., Claessens R. J. M. A. and Suiker A. S. J. (2020). Multi-scale prediction of chemo-mechanical properties of concrete materials through asymptotic homogenization. *Cement and Concrete Research*, **128**, 105929, <https://doi.org/10.1016/j.cemconres.2019.105929>
- Bouarafa S., Lassabatere L., Lipeme-Kouyi G. and Angulo-Jaramillo R. (2019). Hydrodynamic characterization of sustainable urban drainage systems (SuDS) by using beerkan infiltration experiments. *Water*, **11**, 660, <https://doi.org/10.3390/w11040660>
- Bouwer H. (2002). Artificial recharge of groundwater: hydrogeology and engineering. *Hydrogeology Journal*, **10**, 121–142, <https://doi.org/10.1007/s10040-001-0182-4>
- Brachman R. W. I., Moore I. D. and Rowe R. K. (2001). The performance of a laboratory facility for evaluating the structural response of small-diameter buried pipes. *Canadian Geotechnical Journal*, **38**, 260–275, <https://doi.org/10.1139/t00-102>
- Breen J. (1993). Environmental stress cracking of PVC and PVC-CPE. *Journal of Materials Science*, **28**, 3769–3776, <https://doi.org/10.1007/BF00353177>

- Breen J. (1994). Environmental stress cracking of PVC and PVC-CPE. *Journal of Materials Science*, **29**, 39–46, <https://doi.org/10.1007/BF00356570>
- Breen J. (1995). Environmental stress cracking of PVC and PVC-CPE. *Journal of Materials Science*, **30**, 5833–5840, <https://doi.org/10.1007/BF00356729>
- Breen J. (2006). Expected Lifetime of Existing PVC Water Systems: Summary. TNO, Eindhoven.
- Breiman L. (1996). Bagging predictors. *Machine Learning*, **24**(2), 123–140. Scopus, <https://doi.org/10.1023/A:1018054314350>
- Breiman L. (2001). Random forests. *Machine Learning*, **45**(1), 5–32, <https://doi.org/10.1023/A:1010933404324>
- Breiman L., Friedman J., Olshen R. and Stone C. J. (1984). *Classification and Regression Trees* (First), <https://doi.org/10.1201/9781315139470>
- Brennan M., Karimi M., Almeida F., Kroll de Lima F., Ayala P., Obata D., Paschoalini A. and Kessissoglou N. (2017). On the role of vibro-acoustics in leak detection for plastic water distribution pipes. *Procedia Engineering*, **199**(2017), 1350–1355, <https://doi.org/10.1016/j.proeng.2017.09.350>
- Brooks R. H. and Corey, A. T. (1964). Hydraulic properties of porous media. Hydrological papers Colorado state University. Fort Collins, Colorado (USA).
- Bruand A. and Coquet Y. (2005). Les sols et le cycle de l'eau 345.
- Buckingham E. (1907). United States. Bureau of Soils. Studies on the movement of soil moisture. Washington, Govt. Print. Off.
- Burdine N. T. (1953). Relative Permeability Calculations from Pore Size Distribution Data. *Transactions of the American Institute of Mining & Metallurgical Engineers*, **5**, 71–78, <https://doi.org/10.2118/225-g>
- Butters G. (ed.) (1982). Particulate Nature of PVC: Formation, Structure and Processing. Applied Science Publishers, London.
- Caradot N., Riechel M., Fesneau M., Hernandez N., Torres A., Sonnenberg H., Eckert E., Lengemann N., Waschnewski J. and Rouault P. (2018). Practical benchmarking of statistical and machine learning models for predicting the condition of sewer pipes in Berlin, Germany. *Journal of Hydroinformatics*, **20**(5), 1131–1147. Scopus, <https://doi.org/10.2166/hydro.2018.217>
- Caradot N., Sampaio P. R., Guilbert A. S., Sonnenberg H., Perez V. and Dimova V. (2020). Using deterioration modelling to simulate sewer rehabilitation strategy with low data availability. *Water Science & Technology*, **83**(3), 631–640, <https://doi.org/10.2166/wst.2020.604>
- Cardarelli F. (2008). Polymers and elastomers. In: *Materials Handbook: A Concise Desktop Reference*, 2nd edn, F. Cardarelli (ed.), Springer, London, pp. 691–750, [https://doi.org/10.1007/978-1-84628-669-8\\_11](https://doi.org/10.1007/978-1-84628-669-8_11)
- Cassel D. K. and Nielsen D. R. (1986). Field capacity and available water capacity. In: *Methods of Soil Analysis*, John Wiley & Sons, Ltd, New Jersey, USA, pp. 901–926, <https://doi.org/10.2136/sssabookser5.1.2ed.c36>
- Castiglione P., Shouse P. J., Mohanty B. P. and van Genuchten M. T. (2005). Analysis of temperature effects on tension infiltrometry of low permeability materials. *Vadose Zone Journal*, **4**, 481–487, <https://doi.org/10.2136/vzj2004.0134>
- Cerdà A. (1996). Seasonal variability of infiltration rates under contrasting slope conditions in southeast Spain. *Geoderma*, **69**, 217–232, [https://doi.org/10.1016/0016-7061\(95\)00062-3](https://doi.org/10.1016/0016-7061(95)00062-3)
- Cerdà A. (1997). Seasonal changes of the infiltration rates in a Mediterranean scrubland on limestone. *Journal of Hydrology*, **198**, 209–225, [https://doi.org/10.1016/S0022-1694\(96\)03295-7](https://doi.org/10.1016/S0022-1694(96)03295-7)
- Chang L. and Hanssen R. F. (2014). Detection of cavity migration and sinkhole risk using radar interferometric time series. *Remote Sensing of Environment*, **147**, 56–64, <https://doi.org/10.1016/j.rse.2014.03.002>
- Chaoui K., Chudnovsky A. and Moet A. (1987). Effect of residual stress on crack propagation in MDPE pipes. *Journal of Materials Science*, **22**, 3873–3879, <https://doi.org/10.1007/BF01133334>
- Chen T. Y.-J., Vladeanu G., Yazdekhashti S. and Daly C. M. (2022). Performance evaluation of pipe break machine learning models using datasets from multiple utilities. *Journal of Infrastructure Systems*, **28**(2). Scopus, [https://doi.org/10.1061/\(ASCE\)IS.1943-555X.0000683](https://doi.org/10.1061/(ASCE)IS.1943-555X.0000683)
- Cheng Q., Tang C.-S., Xu D., Zeng H. and Shi B. (2021). Water infiltration in a cracked soil considering effect of drying-wetting cycles. *Journal of Hydrology*, **593**, 125640, <https://doi.org/10.1016/j.jhydrol.2020.125640>
- Cherqui F., James R., Poelsma P., Burns M. J., Szota C., Fletcher T. and Bertrand-Krajewski J.-L. (2020). A platform and protocol to standardise the test and selection low-cost sensors for water level monitoring. *H2 Open Journal*, **3**(1), 437–456, <https://doi.org/10.2166/h2oj.2020.050>
- Childs J. L., Wallender W. W. and Hopmans J. W. (1993). Spatial and seasonal variation of furrow infiltration. *Journal of Irrigation and Drainage Engineering*, **119**, 74–90, [https://doi.org/10.1061/\(ASCE\)0733-9437\(1993\)119:1\(74](https://doi.org/10.1061/(ASCE)0733-9437(1993)119:1(74)

- Cho K. S. and Mori T. (1995). A newly isolated fungus participates in the corrosion of concrete sewer pipes. *Water Sci. Technol.*, **31**, 263–271.
- Choi B. H., Zhou Z., Chudnovsky A., Stivala S. S., Sehanobish K. and Bosnyak C. P. (2005). Fracture initiation associated with chemical degradation: observation and modeling. *International Journal of Solids and Structures*, **42**, 681–695, <https://doi.org/10.1016/j.ijsolstr.2004.06.028>
- Chopra M., Kakuturu S., Ballock C., Spence J. and Wanielista M. (2010). Effect of rejuvenation methods on the infiltration rates of pervious concrete pavements. *Journal of Hydrologic Engineering*, **15**(6), 426–433, [https://doi.org/10.1061/\(ASCE\)HE.1943-5584.0000117](https://doi.org/10.1061/(ASCE)HE.1943-5584.0000117)
- Chossat J.-C. (2005). La mesure de la conductivité hydraulique dans les sols. Choix des méthodes, TEC&DOC. ed. Lavoisier.
- Cid Alfaro M. V., Suiker A. S. J., de Borst R. and Remmers J. J. C. (2009). Analysis of fracture and delamination in laminates using 3D numerical modelling. *Engineering Fracture Mechanics*, **76**, 761–780, <https://doi.org/10.1016/j.engfracmech.2008.09.002>
- Cid Alfaro M. V., Suiker A. S. J. and de Borst R. (2010a). Transverse failure behavior of fiber-epoxy systems. *Journal of Composite Materials*, **44**, 1493–1516, <https://doi.org/10.1177/0021998309360941>
- Cid Alfaro M. V., Suiker A. S. J., Verhoosel C. V. and de Borst R. (2010b). Numerical homogenization of cracking processes in thin fibre-epoxy layers. *European Journal of Mechanics – A/Solids*, **29**, 119–131, <https://doi.org/10.1016/j.euromechsol.2009.09.006>
- CIRIA (2007). The SuDS manual CIRIA C697 London. UK.
- Concialdi P., Di Prima S., Bhanderi H. M., Stewart R. D., Abou Najm M. R., Lal Gaur M., Angulo-Jaramillo R. and Lassabatere L. (2020). An open-source instrumentation package for intensive soil hydraulic characterization. *Journal of Hydrology*, **582**, 124492, <https://doi.org/10.1016/j.jhydrol.2019.124492>
- Cortes C. and Vapnik V. (1995). Support-Vector networks. *Machine Learning*, **20**(3), 273–297. Scopus, <https://doi.org/10.1023/A:1022627411411>
- Cossais N., Thomas A., Cherqui F., Morison P., Bos D., Martouzet D., Sibeud E., Honegger A., Lavau S. and Fletcher T. (2017). Understanding the challenges of managing SUDS to maintain or improve their perform.
- County of San Diego (2014). Low Impact Development Handbook-Stormwater Management Strategies. [https://www.sandiegocounty.gov/content/dam/sdc/pds/docs/LID\\_Handbook\\_2014.pdf](https://www.sandiegocounty.gov/content/dam/sdc/pds/docs/LID_Handbook_2014.pdf) (accessed 07/04/2023)
- Dagenais D., Brisson J. and Fletcher T. (2018). The role of plants in bioretention systems: does the science underpin current guidance? *Ecological Engineering*, **120**, 532–545, <https://doi.org/10.1016/j.ecoleng.2018.07.007>
- Daily W., Ramirez A., LaBrecque D. and Nitao J. (1992). Electrical resistivity tomography of vadose water movement. *Water Resources Research*, **28**, 1429–1442, <https://doi.org/10.1029/91WR03087>
- Daily W., Ramirez A., Binley A. and LaBrecque D. (2005). Electrical Resistance Tomography? Theory and Practice, in: Near-Surface Geophysics, Investigations in Geophysics. Society of Exploration. Geophysicists, pp. 525–550, <https://doi.org/10.1190/1.9781560801719.ch17>
- Danielson R. E. and Sutherland P. L. (1986). Porosity. In: *Methods of Soil Analysis*, John Wiley & Sons, Ltd, New Jersey, USA, pp. 443–461, <https://doi.org/10.2136/sssabookser5.1.2ed.c18>
- Davies J. P., Clarke B. A., Whiter J. T. and Cunningham R. J. (2001). Factors influencing the structural deterioration and collapse of rigid sewer pipes. *Urban Water*, **3**, 73–89, [https://doi.org/10.1016/S1462-0758\(01\)00017-6](https://doi.org/10.1016/S1462-0758(01)00017-6)
- Davis J. L., Nica D., Shields K. and Roberts D. J. (1998). Analysis of concrete from corroded sewer pipe. *International Biodeterioration & Biodegradation*, **42**, 75–84, [https://doi.org/10.1016/S0964-8305\(98\)00049-3](https://doi.org/10.1016/S0964-8305(98)00049-3)
- Davis A., Traver R., Hunt W. and Lee R. (2012). Hydrologic performance of bioretention storm-water control measures. *Journal of Hydrologic Engineering*, **5**, 17.
- Deb S. K. and Shukla M. K. (2012). Variability of hydraulic conductivity due to multiple factors. *American Journal of Environmental Sciences*, **8**, 489–502, <https://doi.org/10.3844/ajessp.2012.489.502>
- Dechesne M., Barraud S. and Bardin J.-P. (2002). Performance of stormwater infiltration basins on the long term. Proc of the 9th ICUD. [https://doi.org/10.1061/40644\(2002\)35](https://doi.org/10.1061/40644(2002)35)
- Dechesne M., Barraud S. and Bardin J.-P. (2005). Experimental assessment of stormwater infiltration basin evolution. *Journal of Environmental Engineering*, **131**(7), 1090–1098, [https://doi.org/10.1061/\(ASCE\)0733-9372\(2005\)131:7\(1090\)](https://doi.org/10.1061/(ASCE)0733-9372(2005)131:7(1090))
- Deffontis S., Breton A., Vialle C., Montrejeaud-Vignoles M., Vignoles C. and Sablayrolles C. (2013). Impact of dry weather discharges on annual pollution from a separate storm sewer in Toulouse, France. *Science of the Total Environment*, **452–453**, 394–403, <https://doi.org/10.1016/j.scitotenv.2013.03.014>

- de Groot A. C. (2015). A study on the fouling process in inverted siphons over time. Respository TU dElt: <https://repository.tudelft.nl/islandora/object/uuid%3A6262a3e6-f408-4cd5-84e5-db388e127cd6> (visited 25 August 2023).
- Dempster A. P., Laird N. M. and Rubin D. B. (1977). Maximum likelihood from incomplete data via the EM algorithm. *Journal of the Royal Statistical Society. Series B*, **39**(1), 1–38.
- Di Prima S., Lassabatere L., Bagarello V., Iovino M. and Angulo-Jaramillo R. (2015). Testing a new automated single ring infiltrometer for Beerkan infiltration experiments. *Geoderma*, **262**, 20–34, <https://doi.org/10.1016/j.geoderma.2015.08.006>
- Di Prima S., Winiarski T., Angulo-Jaramillo R., Stewart R. D., Castellini M., Abou Najm M. R., Ventrella D., Pirastru M., Giadrossich F., Capello G., Biddoccu M. and Lassabatere L. (2020). Detecting infiltrated water and preferential flow pathways through time-lapse ground-penetrating radar surveys. *Science of The Total Environment*, **726**, 138511, <https://doi.org/10.1016/j.scitotenv.2020.138511>
- Di Prima S., Fernandes G., Marras E., Giadrossich F., Stewart R. D., Abou Najm M. R., Winiarski T., Mourier B., Angulo-Jaramillo R., Comegna A., del Campo A. and Lassabatere L. (2023). Evaluating subsurface flow connectivity in a pine-covered hillslope with stemflow infiltration and ground-penetrating radar surveys. *Journal of Hydrology*, **620**, 129527, <https://doi.org/10.1016/j.jhydrol.2023.129527>
- Dirksen J., Baars E., Langeveld G. and Clemens F. (2012). Settlement as a driver for sewer rehabilitation. *Water Science & Technology*, **66**(7), 1534–1539, <https://doi.org/10.2166/wst.2012.347>
- Dirksen J. (2013). Monitoring ground settlement to guide sewer asset management. PhD thesis, Delft University of Technology. ISBN 978-94-6108-474 3. [https://repository.tudelft.nl/islandora/search/author%3A%22Dirksen%20C%20J.%22?f%5B0%5D=mods\\_genre\\_s%3A%22doctoral%5C%20thesis%22](https://repository.tudelft.nl/islandora/search/author%3A%22Dirksen%20C%20J.%22?f%5B0%5D=mods_genre_s%3A%22doctoral%5C%20thesis%22)
- Dirksen J., Clemens F., Korving H., Cherqui F., Le Gauffre P., Ertl T., Plihal H., Mueller K. and Snaterse C. (2013a). The consistency of visual sewer inspection data. *Structure and Infrastructure Engineering*, **9**(3), 214–228, <https://doi.org/10.1080/15732479.2010.541265>
- Dirksen J., Baars E., Langeveld J. G. and Clemens F. H. L. R. (2013b). The impact of fat, oil and grease on the performance of sanitary systems. Proc. Of the 7th int. Conf. On Sewer Processes and Networks (SPN7), Sheffield, UK.
- Doolittle J. A. and Brevik E. C. (2014). The use of electromagnetic induction techniques in soils studies. *Geoderma*, **223–225**, 33–45, <https://doi.org/10.1016/j.geoderma.2014.01.027>
- Drake J. and Bradford A. (2013). Assessing the potential for restoration of surface permeability for permeable pavements through maintenance. *Water Science & Technology*, **68**(9), 1950–1958, <https://doi.org/10.2166/wst.2013.450>
- Duinmeijer S. P. A. (2020). On the free vortex driven motion of buoyant particles. PhD thesis, TU Delft. ISBN 978-946366-271-0, <https://doi.org/10.4233/uuid:a33fa2a9-f347-40a3-96be-51e880018974>
- Duinmeijer S. P. A. and Clemens F. H. L. R. (2021). An experimental study on the motion of buoyant particles in the free-surface vortex flow. *Journal of Hydraulic Research*, **59**, 947–962, <https://doi.org/10.1080/00221686.2020.1845827>
- DWA-A 113. Hydraulic dimensioning and testing of sewage ressure mains (org. Title in German: Hydraulische Dimensionierung und Leistungsnachweis von Abwasserdrucksystemen).
- DWA-M 149-9. Assesment of the condition of drainage systems outside buildings, part 9 : inspection and manitenance of sewage pressure mains.(org title in German : Zustandserfassung und -beurteilung von Entwässerungssystemen außerhalb von Gebäuden – Teil 9: Inspektion und Wartung von Abwasserdruckleitungen).
- El-Housni H., Ouellet M. and Duchesne S. (2018). Identification of most significant factors for modelling deterioration of sewer pipes. *Canadian Journal of Civil Engineering*, **45**(3), 215–226, <https://doi.org/10.1139/cjce-2015-0293>
- Ellis B. and Butler D. (2015). Surface water sewer misconnections in England and Wales: pollution sources and impacts. *Science of the Total Environment*, **526**, 98–109, <https://doi.org/10.1016/j.scitotenv.2015.04.042>
- Emerson C., Wadzuk B. and Traver R. (2010). Hydraulic evolution and total suspended solids capture of an infiltration trench. In *Hydrological processes*, **24**(8), 1008–1014, <https://doi.org/10.1002/hyp.7539>
- EN 13508-2 (2011). Investigation and assessment of drain and sewer systems outside buildings – Part 2: Visual inspection coding system (European Standard). European Committee for Standardization, Brussels, Belgium.
- Erdogmus E. and Tadros M. K. (2009). Behavior and Design of Buried Concrete Pipe-Phase 2. Nebraska Department of Roads, Lincoln, NE, p. 124.



- Eriksen K. (2003). Thaumassite attack on concrete at marbjerg waterworks. *Cement and Concrete Composites*, **25**, 1147–1150, [https://doi.org/10.1016/S0958-9465\(03\)00151-3](https://doi.org/10.1016/S0958-9465(03)00151-3)
- Erickson A., Weiss P. and Gulliver J. (2013). Optimizing stormwater treatment practices. A handbook of assessment and maintenance. Springer New York, NY, ISBN 978-1-899-9401-1/978-1-4614-623-1. <https://doi.org/10.1007/978-1-4614-4624-8>
- European Committee for Standardization (2005). NEN-EN 1992-1-1 – Eurocode 2: Design of concrete structures – Part 1-1: General rules and rules for buildings.
- European Committee for Standardization (2013). NEN-EN 12390-13 – Testing hardened concrete – Part 13: Determination of secant modulus of elasticity in compression.
- Fan Y. F., Hu Z. Q., Zhang Y. Z. and Liu J. L. (2010). Deterioration of compressive property of concrete under simulated acid rain environment. *Construction and Building Materials*, **24**, 1975–1983, <https://doi.org/10.1016/j.conbuildmat.2010.04.002>
- Fan B., Liu X., Zhu Q., Qin G., Li J., Lin H. and Guo L. (2020). Exploring the interplay between infiltration dynamics and critical zone structures with multiscale geophysical imaging: a review. *Geoderma*, **374**, 114431, <https://doi.org/10.1016/j.geoderma.2020.114431>
- Fannin R. J. and Slangen P. (2014). On the distinct phenomena of suffusion and suffosion. *Geotechnique Letters*, **4**, 289–294, <https://doi.org/10.1680/geolett.14.00051>
- Farny J. A. and Kerkhoff B. (1977). Diagnosis and Control of Alkali-aggregate Reactions in Concrete, Portland Cement Association Skokie, IL.
- Fassman E. A., Simcock R. and Wang S. (2013). *Media Specification for Stormwater Bioretention Devices*, Auckland UniServices for Auckland Council. technical report. TR2013/011.
- Fatemi Aghda S., Ganjalipour K. and Nabiollahi K. (2018). Comparison of performance inclinometer casing and TDR technique. *Journal of Applied Geophysics*, **150**, 182–194, <https://doi.org/10.1016/j.appgeo.2018.01.022>
- Faure B. and Lemaire F. (1990). Nettoyage et décolmatage des enrobés drainants en milieu urbain. *Revue générale des routes et aéroports*, N°677.
- Fausett L. V. (1994). Fundamentals of Neural Networks: Architectures, Algorithms, and Applications. Prentice-Hall, New Jersey, USA.
- Fernandes G., Roques O., Lassabatere L., Sarles L., Venisseau A., Marchand P. and Bedell J.-P. (2022). Influence of edaphic conditions and persistent organic pollutants on earthworms in an infiltration basin. , **304**, 119192, <https://doi.org/10.1016/j.envpol.2022.119192>
- Fillot L. A., Hajji P., Gauthier C. and Masenelli-Varlot K. (2006). U-PVC gelation level assessment, part 1: comparison of different techniques. *Journal of Vinyl and Additive Technology*, **12**, 98–107, <https://doi.org/10.1002/vnl.20077>
- Fletcher T., Shuster W., Hunt W. F., Butler D., Scott A., Trowsdale S., Barraud S., Semandeni-Davies A., Bertrand-Krajewski J.-L., Mikkelsen P. S., Rivard G., Uhl M., Dagenais D. and Viklander M. (2015). SUDS, LID, BMPs, WSUD and more – The evolution and application of terminology surrounding urban drainage. *Urban Water Journal*, **12**(7), 525–542, <https://doi.org/10.1080/1573062X.2014.916314>
- Foster M., Fell R. and Spannagle M. (2000). The statistics of embankment dam failures and accidents. *Canadian Geotechnical Journal*, **37**, 1000–1024, <https://doi.org/10.1139/t00-030>
- Fowdar H., Payne E., Deletic A., Zhang K. and McCarthy D. (2022). Advancing the sponge city agenda: evaluation of 22 plant species across a broad range of life forms for stormwater management. *Ecological Engineering*, **175**, 106501, <https://doi.org/10.1016/j.ecoleng.2021.106501>
- Fragoudakis R. (2017). Failure concepts in fiber reinforced plastics. In: Failure Analysis and Prevention, IntechOpen, <https://doi.org/10.5772/intechopen.71822>
- Fujiyama M. and Kondou M. (2004). Effect of degree of polymerization on gelation and flow processability of poly (vinyl chloride). *Journal of Applied Polymer Science*, **92**, 1915–1938, <https://doi.org/10.1002/app.20181>
- Gardner W. H. (1986). Water Content, in: Methods of Soil Analysis. John Wiley & Sons, Ltd, New Jersey, USA, pp. 493–544, <https://doi.org/10.2136/sssabookser5.1.2ed.c21>
- Gautier A. (1998). Contribution à la connaissance du fonctionnement d'ouvrages d'infiltration d'eau de ruissellement pluvial urbain. PhD INSA de Lyon, Villeurbanne, France.
- Gerke H. H., Germann P. and Nieber J. (2010). Preferential and unstable flow: from the pore to the catchment scale. *Vadose Zone Journal*, **9**, 207–212, <https://doi.org/10.2136/vzj2010.0059>
- Géron A. (2019). Hands-on Machine Learning with Scikit-Learn, Keras, and TensorFlow, 2nd edition, O'Reilly Media, California, USA.



## 220 Asset Management of Urban Drainage Systems: if anything exciting happens, we've done it wrong!

- Giakoumis T. and Voulvoulis N. (2023). Combined sewer overflows: relating event duration monitoring to wastewater systems' capacity in England. *Environmental Science Water Research & Technology*, **9**, 707–722, <https://doi.org/10.1039/d2ew00637e>
- Gladchenko A. N., Shevelya I. V., Kiyanita E. V. and Derkach V. V. (1997). Wear of working members of extruders for processing polymers. *Chemical and Petroleum Engineering*, **33**, 367–370, <https://doi.org/10.1007/BF02416718>
- Glaser B., Jackisch C., Hopp L. and Klaus J. (2019). How meaningful are plot-scale observations and simulations of preferential flow for catchment models? *Vadose Zone Journal*, **18**, 1–18, <https://doi.org/10.2136/vzj2018.08.0146>
- Goh H. W., Zakaria N. A., Lau T. L., Foo K. Y., Chang C. K. and Leow C. S. (2017). Mesocosm study of enhanced bioretention media in treating nutrient rich stormwater for mixed development area. *Urban Water Journal*, **14**(2), 134–142, <https://doi.org/10.1080/1573062X.2015.1076861>
- Gokhale S. and Graham J. A. (2004). A new development in locating leaks in sanitary sewers. *Tunnelling and Underground Space Technology*, **19**(1), 85–96, <https://doi.org/10.1016/j.tust.2003.08.003>
- Gonzalez-Merchan C., Barraud S., Le Coustumer S. and Fletcher T. (2012). Monitoring of clogging evolution in the stormwater infiltration system and determinant factors. *European Journal of Environmental and Civil Engineering*, **16**(1), 34–67, <https://doi.org/10.1080/19648189.2012.682457>
- Gonzalez-Merchan C., Barraud S. and Bedell J. P. (2014). Influence of spontaneous vegetation in stormwater infiltration system clogging. *Environmental Science and Pollution Research*, **21**(8), 5419–5426, <https://doi.org/10.1007/s11356-013-2398-y>
- Goutaland D., Winiarski T., Angulo-Jaramillo R., Lassabatere L., Bièvre G., Buoncristiani J.-F., Dubé J.-S., Mesbah A. and Cazalets H. (2007). Hydrogeophysical study of the heterogeneous unsaturated zone of a stormwater infiltration basin, pp. 173–192.
- Green W. H. and Ampt G. A. (1911). Studies on soil physics. *The Journal of Agricultural Science*, **4**, 1–24, <https://doi.org/10.1017/S0021859600001441>
- Green T. R., Ahuja L. R. and Benjamin J. G. (2003). Advances and challenges in predicting agricultural management effects on soil hydraulic properties. *Geoderma, Quantifying Agricultural Management Effects on Soil Properties and Processes*, **116**, 3–27.
- Gregory J., Dukes M., Miller G. and Jones P. (2005). Analysis of double-ring infiltration techniques and development of a simple automatic water delivery system. *Applied Turfgrass Science*, **2**, 1–7, <https://doi.org/10.1094/ATS-2005-0531-01-MG>
- Grengg C., Mittermayr F., Baldermann A., Böttcher M. E., Leis A., Koraimann G., Grunert P. and Dietzel M. (2015). Microbiologically induced concrete corrosion: a case study from a combined sewer network. *Cement and Concrete Research*, **77**, 16–25, <https://doi.org/10.1016/j.cemconres.2015.06.011>
- Grengg C., Mittermayr F., Ukrainczyk N., Koraimann G., Kienesberger S. and Dietzel, M. (2018). Advances in concrete materials for sewer systems affected by microbial induced concrete corrosion: A review. *Water Research*, **134**, 341–352, <https://doi.org/10.1016/j.watres.2018.01.043>
- Gu L., Visintin P. and Bennett T. (2018). Evaluation of accelerated degradation test methods for cementitious composites subject to sulphuric acid attack: application to conventional and alkali activated concretes. *Cement and Concrete Composites*, (87), 187–204, <https://doi.org/10.1016/j.cemconcomp.2017.12.015>
- Guo L., Chen J. and Lin H. (2014). Subsurface lateral preferential flow network revealed by time-lapse ground-penetrating radar in a hillslope. *Water Resources Research*, **50**, 9127–9147, <https://doi.org/10.1002/2013WR014603>
- Haile T. M., Hobiger G., Kammerer G., Allabashi R., Schaerfing B. and Fuerhacker M. (2016). Hydraulic performance and pollutant concentration profile in a stormwater runoff filtration systems. *Water Air Soil Pollution*, **227**(1), 34, <https://doi.org/10.1007/s11270-015-2736-4>
- Hallaji S. M., Fang Y. and Winfrey B. K. (2022). Predictive maintenance of pumps in civil infrastructure: state-of-the-art, challenges and future directions. *Automation in Construction*, **134**, 104049, <https://doi.org/10.1016/j.autcon.2021.104049>
- Hallett P. D. (2008). A brief overview of the causes, impacts and amelioration of soil water repellency – a review. *Soil and Water Research*, **3**, S21–S29, <https://doi.org/10.17221/1198-swr>
- Hallett P. D., Nunan N., Douglas J. T. and Young I. M. (2004). Millimeter-scale spatial variability in soil water sorptivity. *Soil Science Society of America Journal*, **68**, 352–358, <https://doi.org/10.2136/sssaj2004.3520>
- Hamel P. and Fletcher T. D. (2014). The impact of stormwater source-control strategies on the (low) flow regime of urban catchments. *Water Science & Technology*, **69**(4), 739–745, <https://doi.org/10.2166/wst.2013.772>
- Hart T. D. (2017). Root-enhanced Infiltration in Stormwater Bioretention Facilities in Portland, Oregon. Dissertations and Theses, Portland state University. Paper 3468, <https://doi.org/10.15760/etd.5352>

- Harvey R. R. and McBean E. A. (2014a). Comparing the utility of decision trees and support vector machines when planning inspections of linear sewer infrastructure. *Journal of Hydroinformatics*, **16**(6), 1265–1279. Scopus, <https://doi.org/10.2166/hydro.2014.007>
- Harvey R. R. and McBean E. A. (2014b). Predicting the structural condition of individual sanitary sewer pipes with random forests. *Canadian Journal of Civil Engineering*, **41**(4), 294–303. Scopus, <https://doi.org/10.1139/cjce-2013-0431>
- Hatt B. E., Lewis J. F., Fletcher T. D. and Deletic A. (2007). Insights from the design, construction and operation of an experimental biofiltration system. 13th International Rainwater Catchment Systems Conference and 5th International Water Sensitive Urban Design.
- Hatt B. E., Fletcher T. D. and Deletic A. (2009). Hydrologic and pollutant removal performance of stormwater biofiltration systems at the field scale. *Journal of Hydrology*, **365**(3–4), 310–321, <https://doi.org/10.1016/j.jhydrol.2008.12.001>
- Hawari A., Alkadour F., Elmasry M. and Zayed T. (2017). Simulation-based condition assessment model for sewer pipelines. *Journal of Performance of Constructed Facilities*, **31**(1). Scopus, [https://doi.org/10.1061/\(ASCE\)CF.1943-5509.0000914](https://doi.org/10.1061/(ASCE)CF.1943-5509.0000914)
- Hawari A., Alkadour F., Elmasry M. and Zayed T. (2020). A state of the art review on condition assessment models developed for sewer pipelines. *Engineering Applications of Artificial Intelligence*, **93**, 103721, <https://doi.org/10.1016/j.engappai.2020.103721>
- Haws N. W., Das B. S. and Rao P. S. C. (2004). Dual-domain solute transfer and transport processes: evaluation in batch and transport experiments. *Journal of Contaminant Hydrology*, **75**, 257–280, <https://doi.org/10.1016/j.jconhyd.2004.07.001>
- Henderson V. and Tighe S. (2011). Evaluation of pervious concrete pavement permeability renewal maintenance methods at field sites in Canada. *Canadian Journal of Civil Engineering*, **38**(12), 1404–1413.
- Hernández N., Caradot N., Sonnenberg H., Rouault P. and Torres A. (2021). Optimizing SVM models as predicting tools for sewer pipes conditions in the two main cities in Colombia for different sewer asset management purposes. *Structure and Infrastructure Engineering*, **17**(2), 156–169. Scopus, <https://doi.org/10.1080/15732479.2020.1733029>
- Hill J. J., Kurdziel J. M., Nelson C. R., Nystrom J. A. and Sondag M. S. (1999). Minnesota department of transportation overload field tests of standard and standard installation direct design reinforced concrete pipe installations. *Transportation Research Record: Journal of the Transportation Research Board*, **1656**, 64–72, <https://doi.org/10.3141/1656-09>
- Hillel D. (1998). *Environmental Soil Physics: Fundamentals, Applications, and Environmental Considerations*. Elsevier, Amsterdam, The Netherlands.
- Hoes O. A. C., Schilperoort R. P. S., Luxemburg W. M. J., Clemens F. H. L. R. and van de Giessen, N. C. (2009). Locating illicit connections in storm water sewers using fiber-optic distributed temperature sensing. *Water Research*, **43**(20), 5187–5197, <https://doi.org/10.1016/j.watres.2009.08.020>
- Hordijk D. A. (1991). Local approach to fatigue of concrete. Ph.D. thesis, Delft University of Technology, Delft, The Netherlands.
- Horton R. E. (1941). An approach toward a physical interpretation of infiltration-Capacity1. *Soil Science Society of America Journal*, **5**, 399–417, <https://doi.org/10.2136/sssaj1941.036159950005000C0075x>
- Horton R. E. (1945). Erosional development of streams and their drainage basin; hydrophysical approach to quantitative morphology. *Geological Society of America Bulletin*, **56**, 275–370, [https://doi.org/10.1130/0016-7606\(1945\)56\[275:EDOSAT\]2.0.CO;2](https://doi.org/10.1130/0016-7606(1945)56[275:EDOSAT]2.0.CO;2)
- Hosmer D. W. and Lemeshow S. (2000). *Applied Logistic Regression*. Wiley Publishing, New Jersey, USA.
- Hunt W. F., Greenway M., Moore T. C., Brown R. A., Kennedy S. G., Line D. E. and Lord W. G. (2011). Constructed stormwater wetland installation and maintenance: are we getting it right? *Journal of Irrigation and Drainage Engineering*, **137**(8), 469–474, [https://doi.org/10.1061/\(ASCE\)IR.1943-4774.0000326](https://doi.org/10.1061/(ASCE)IR.1943-4774.0000326)
- Hunter R. P. and Bowman E. T. (2018). Visualisation of seepage-induced suffusion and suffosion within internally erodible granular media. *Geotechnique*, **68**, 918–930, <https://doi.org/10.1680/jgeot.17.P.161>
- Hussain I., Hamid S. H. and Khan J. H. (1995). Polyvinyl chloride pipe degradation studies in natural environments. *Journal of Vinyl and Additive Technology*, **1**, 137–141, <https://doi.org/10.1002/vnl.730010305>
- Hutař P., Ševčík M., Nahlik L., Pinter G., Frank A. and Mitev I. (2011). A numerical methodology for lifetime estimation of HDPE pressure pipes. *Engineering Fracture Mechanics*, **78**, 3049–3058, <https://doi.org/10.1016/j.engfracmech.2011.09.001>
- Hutař P., Ševčík M., Frank A., Nahlik L., Kučera J. and Pinter G. (2013). The effect of residual stress on polymer pipe lifetime. *Engineering Fracture Mechanics*, **108**, 98–108, <https://doi.org/10.1016/j.engfracmech.2013.04.014>

## 222 Asset Management of Urban Drainage Systems: if anything exciting happens, we've done it wrong!

- Hutchinson J. M. (1995). Physical aging of polymers. *Progress in Polymer Science*, **20**, 703–760, [https://doi.org/10.1016/0079-6700\(94\)00001-1](https://doi.org/10.1016/0079-6700(94)00001-1)
- Hvitved-Jacobsen T., Vollertsen J. and Nielsen A. H. (2013). Sewer processes. Microbial and chemical process engineering of sewer networks, second edition. eBook, ISBN 9780429110986, <https://doi.org/10.1201/b14666>
- Indiketiya S., Jegatheesan P., Rajeev P. and Kuwano R. (2019). The influence of pipe embedment material on sinkhole formation due to erosion around defective sewers. *Transportation Geotechnics*, **19**, 110–125, <https://doi.org/10.1016/j.trgeo.2019.03.001>
- Ismail N., Nonaka T., Noda S. and Mori T. (1993). Effect of carbonation on microbial corrosion of concretes. *Doboku Gakkai Ronbunshu*, **20**(474), 133–138, [https://doi.org/10.2208/jscej.1993.474\\_133](https://doi.org/10.2208/jscej.1993.474_133)
- Jačka L., Pavlásek J., Kuráž V. and Pech P. (2014). A comparison of three measuring methods for estimating the saturated hydraulic conductivity in the shallow subsurface layer of mountain podzols. *Geoderma*, **219–220**, 82–88, <https://doi.org/10.1016/j.geoderma.2013.12.027>
- Janson L. E. (2003). *Plastics Pipes for Water Supply and Sewage Disposal*, 4th ed., Borealis, Stenungsund.
- Jenkins L., Gokhale S. and McDonald M. (2015). Comparison of pipeline failure prediction models for water distribution networks with uncertain and limited data. *Journal of Pipeline Systems Engineering and Practice*, **6**(2). Scopus, [https://doi.org/10.1061/\(ASCE\)PS.1949-1204.0000181](https://doi.org/10.1061/(ASCE)PS.1949-1204.0000181)
- Jensen A. L. (2018). Characterisation of rag properties and their transport in wastewater pumps. PhD Thesis, Aalborg University. ISBN (online): 978-87-7210-211-5, <https://doi.org/10.5278/vbn.phd.eng.00049>
- Jeong H. Y., Jun S.-C., Cheon J.-Y. and Park M. (2018). A review on clogging mechanisms and managements in aquifer storage and recovery (ASR) applications. *Geosciences Journal*, **22**, 667–679, <https://doi.org/10.1007/s12303-017-0073-x>
- Jiang Y., Zevenbergen C. and Ma Y. (2018). Urban pluvial flooding and stormwater management: A contemporary review of Chia's challenges and “sponge” cities strategy. *Environmental Science and Policy*, **80**(2018), 132–143, <https://doi.org/10.1016/j.envsci.2017.11.016>
- Johansson L. and Tornell B. (1987). Initiation of fractures in rigid PVC pipes by soft particles. *Journal of Vinyl and Additive Technology*, **9**, 103–107, <https://doi.org/10.1002/vnl.730090304>
- Jones J. A. A. (2010). Soil piping and catchment response. *Hydrological Processes*, **24**, 1548–1566, <https://doi.org/10.1002/hyp.7634>
- Kabir G., Tesfamariam S., Hensing J. and Sadiq R. (2020). Handling incomplete and missing data in water network database using imputation methods. *Sustainable and Resilient Infrastructure*, **5**(6), 365–377, <https://doi.org/10.1080/23789689.2019.1600960>
- Kang J., Parker F. and Yoo C. H. (2007). Soil-structure interaction and imperfect trench installations for deeply buried concrete pipes. *Journal of Geotechnical and Geoenvironmental Engineering*, **133**, 277–285, [https://doi.org/10.1061/\(ASCE\)1090-0241\(2007\)133:3\(277\)](https://doi.org/10.1061/(ASCE)1090-0241(2007)133:3(277))
- Kauffman G. J., Belden A. C., Vonck K. J. and Homsey A. R. (2009). Link between impervious cover and base flow in the white clay creek wild and scenic watershed in Delaware. *Journal of Hydrologic Engineering*, **14**(4), 324–334, [https://doi.org/10.1061/\(ASCE\)1084-0699\(2009\)14:4\(324\)](https://doi.org/10.1061/(ASCE)1084-0699(2009)14:4(324))
- Kluge B., Markert A., Facklam M., Sommer H., Kaiser M., Pallasch M. and Wessolek G. (2018). Metal accumulation and hydraulic performance of bioretention systems after long-term operation. *Journal of Soils & Sediments*, **18**(2), 431–441, <https://doi.org/10.1007/s11368-016-1533-z>
- Knapen A., Poesen J., Govers G., Gyssels G. and Nachtergaele J. (2007). Resistance of soils to concentrated flow erosion: a review. *Earth-Science Reviews*, **80**, 75–109, <https://doi.org/10.1016/j.earscirev.2006.08.001>
- Kodešová R., Šimůnek J., Nikodem A. and Jirků V. (2010). Estimation of the dual-permeability model parameters using tension disk infiltrometer and Guelph permeameter. *Vadose Zone Journal*, **9**, 213–225, <https://doi.org/10.2136/vzj2009.0069>
- Kooij C., Muhle S., Clemens F., Pothof I. and Blokzijl F. (2015). Performance Indicators for Complex Wastewater Pumping Stations and Pressure Mains, <https://doi.org/10.4108/icst.iniscom.2015.258385>
- Koppe E., Schneider F. J. A., Londero A. L., de Queiroz R., Buligon L. and Minella J. P. G. (2022). Soil water infiltration evaluation from punctual to hillslope scales. *Environmental Monitoring and Assessment*, **194**, 300, <https://doi.org/10.1007/s10661-022-09893-x>
- Korving J. L. (2004). Probabilistic assessment of the performance of combined sewer systems. PhD Thesis, Delft University of Technology. ISBN: 90-9018056-7.
- Korving J. L. and Ottenhoff E. C. (2008). Analysis of the causes of pump failure and differences of failure characteristics. *Water Science & Technology*, **57**(8), 1271–1276, <https://doi.org/10.2166/wst.2008.304>

- Korving J. L., Clemens F. and van Noortwijk J. (2006a). Statistical modelling of the serviceability of sewage pumps. *Journal of Hydraulic Engineering*, **132**(10), 1076–1085, [https://doi.org/10.1061/\(ASCE\)0733-9429\(2006\)132:10\(1076\)](https://doi.org/10.1061/(ASCE)0733-9429(2006)132:10(1076))
- Korving J. L., Geise M. and Clemens F. (2006b). Failure of sewage pumps: statistical modelling and impact assessment. *Water Science & Technology*, **54**(6–7), 119–126, <https://doi.org/10.2166/wst.2006.577>
- Kotsiantis S. B. (2013). Decision trees: A recent overview. *Artificial Intelligence Review*, **39**(4), 261–283, <https://doi.org/10.1007/s10462-011-9272-4>
- Kuriyama T., Narisawa I., Shina R. and Kotaki M. (1998). Effects of morphology on the fracture toughness of PVC-U pipe. *Journal of Vinyl and Additive Technology*, **4**, 164–168, <https://doi.org/10.1002/vnl.10035>
- Kutlílek M. and Nielsen D. R. (2015). Soil. Springer Netherlands, Dordrecht, <https://doi.org/10.1007/978-94-017-9789-4>
- Laakso T., Kokkonen T., Mellin I. and Vahala R. (2018). Sewer condition prediction and analysis of explanatory factors. *Water (Switzerland)*, **10**(9), 1239. Scopus, <https://doi.org/10.3390/w10091239>
- Lassabatere L., Di Prima S., Bouarafa S., Iovino M., Bagarello V. and Angulo-Jaramillo R. (2019). BEST-2K method for characterizing dual-permeability unsaturated soils with ponded and tension infiltrometers. *Vadose Zone Journal*, **18**, 1–20, <https://doi.org/10.2136/vzj2018.06.0124>
- Le Coustumer S. and Barraud S. (2007). Long-term hydraulic and pollution retention performance of infiltration systems. *Water Science & Technology*, **55**(4), 235–243, <https://doi.org/10.2166/wst.2007.114>
- Le Coustumer S., Fletcher T. D., Deletic A., Barraud S. and Lewis J. F. (2009). Hydraulic performance of biofilter systems for stormwater management: influences of design and operation. *Journal of Hydrology*, **376**(1–2), 16–23, <https://doi.org/10.1016/j.jhydrol.2009.07.012>
- Le Coustumer S., Fletcher T. D., Deletic A., Barraud S. and Poelsma P. (2012). The influence of design parameters on logging of stormwater biofilters: a large-scale column study. *Water Research*, **46**(20), 6743–6752, <https://doi.org/10.1016/j.watres.2012.01.026>
- Le Gat Y. (2008). Modelling the deterioration process of drainage pipelines. *Urban Water Journal*, **5**(2), 97–106, <https://doi.org/10.1080/15730620801939398>
- Lepot M., Hernandez B., Cedillo S., Marzloff I., Goes B., Schellart A., Verlinden J. and Clemens F. (2016). Use of numbered and coloured 3D printed pills a new, low-cost robust and easy method to inspect mis-, cross-, and illicit connections in separate sewers. Proc. of NOVATECH 2016, Lyon, France.
- Lepot M., Makris K. and Clemens F. (2017). Detection and quantification of lateral, illicit connections and infiltration in sewers with infra-red camera: conclusions after a wide experimental plan. *Water Research*, **122**, 679–691, <https://doi.org/10.1016/j.watres.2017.06.030>
- Lindsey G., Roberts L. and Page W. (1992). Inspection and maintenance of infiltration facilities. *J. Soil and Water Conservation*, **47**(6), 481–486.
- Lubbers C. L. (2007). On gas pockets in wastewater pressure mains and their effect on hydraulic performance. Delft University of Press, IOS Press, Amsterdam. ISBN: 978-1-58603-789-5.
- Luimes R. A., Suiker A. S. J., Verhoosel C. V., Jorissen A. J. M. and Schellen H. L. (2018). Fracture behaviour of historic and new oak wood. *Wood Science and Technology*, **52**, 1243–1269, <https://doi.org/10.1007/s00226-018-1038-6>
- Luimes R. A., Schepers I. C., Suiker A. S. J., Bosco E. and Clemens F. H. L. R. (2022). Effect of biochemical attack on the mechanical performance of used concrete sewer pipes. *Construction and Building Materials*, **346**, 128390, <https://doi.org/10.1016/j.conbuildmat.2022.128390>
- Luimes R. A., Schepers I. C., Suiker A. S. J., Bosco E. and Clemens F. H. L. R. (2023). Assessment of chemo-mechanical degradation of concrete sewer pipes through an integrated experimental approach. *Engineering Structures*, **293**, 116590, <https://doi.org/10.1016/j.engstruct.2023.116590>
- MacDougall K., Hoult N. A. and Moore I. D. (2016). Measured load capacity of buried reinforced concrete pipes. *ACI Structural Journal*, **113**, 63–74, <https://doi.org/10.14359/51688059>
- Madanat S., Mishalani R. and Ibrahim W. H. W. (1995). Estimation of infrastructure transition probabilities from condition rating data. *Journal of Infrastructure Systems*, **1**(2), 120–125, [https://doi.org/10.1061/\(ASCE\)1076-0342\(1995\)1:2\(120\)](https://doi.org/10.1061/(ASCE)1076-0342(1995)1:2(120))
- Makris K. F., Langeveld J. G. and Clemens F. H. L. R. (2021). Extensive testing on PVC sewer pipes identifying the factors that affect their operational lifetime. *Journal of Structure and Infrastructure Engineering*, **18**, 1–13, <https://doi.org/10.1080/15732479.2021.1907601>
- Malinowska A. A., Witkowski W. T., Hejmanowski R., Chang L., van Leijen F. J. and Hanssen R. F. (2019). Sinkhole occurrence monitoring over shallow abandoned coal mines with satellite-based persistent scatterer interferometry. *Engineering Geology*, **262**, 105336, <https://doi.org/10.1016/j.enggeo.2019.105336>



- Marquez-Penaranda J. F., Sanchez-Silva M., Hussler J. and Bastidas-Arteaga E. (2015). Effects of biodeterioration on the mechanical properties of concrete. *Materials and Structures*, **49**(2015), 4085–4099.
- Marsalek J., Watt W. and Anderson B. (2006). Trace metal levels in sediments deposited in urban stormwater management facilities. *Water Science & Technology*, **53**(2), 175–183, <https://doi.org/10.2166/wst.2006.051>
- Mashford J., Marlow D., Tran D. and May R. (2011). Prediction of sewer condition grade using support vector machines. *Journal of Computing in Civil Engineering*, **25**(4), 283–290. Scopus, [https://doi.org/10.1061/\(ASCE\)CP.1943-5487.0000089](https://doi.org/10.1061/(ASCE)CP.1943-5487.0000089)
- McCullagh P. and Nelder J. A. (1989). *Generalized Linear Models*, 2nd edn. Chapman & Hall, London, UK, <https://doi.org/10.1201/9780203753736>
- McGrath T. J., Selig E. T., Webb M. C. and Zoladz G. V. (1999). Pipe Interaction with the Backfill Envelope. US Department of Transportation, McLean, VA, p. 269.
- Medjnoun A. and Bahar R. (2016). Shrinking–swelling of clay under the effect of hydric cycles. *Innovative Infrastructure Solutions*, **1**, 46, <https://doi.org/10.1007/s41062-016-0043-6>
- Meguid M. A. and Dang H. K. (2009). The effect of erosion voids on existing tunnel linings. *Tunnelling and Underground Space Technology*, **24**, 278–286, <https://doi.org/10.1016/j.tust.2008.09.002>
- Meguid M. A. and Kamel S. (2014). A three-dimensional analysis of the effects of erosion voids on rigid pipes. *Tunnelling and Underground Space Technology*, **43**, 276–289, <https://doi.org/10.1016/j.tust.2014.05.019>
- Melbourne Water (2023). guidelines. <https://www.melbournewater.com.au/building-and-works/developer-guides-and-resources/guidelines-drawings-and-checklists/guidelines> (07/04/2023).
- Mittermayr F., Rezvani M., Baldermann A., Hainer S., Breitenbücher P., Juhart J., Graubner C.-A. and Proske T. (2015). Sulfate resistance of cement-reduced eco-friendly concretes. *Cement and Concrete Composites*, **55**, 364–375, <https://doi.org/10.1016/j.cemconcomp.2014.09.020>
- Moarcas O. and Irle M. (1999). Determination of Poisson's ratio for particleboard in pure bending. *Wood Science & Technology*, (33), 439–44, <https://doi.org/10.1007/s002260050128>
- Moffat R., Fannin R. J. and Garner S. J. (2011). Spatial and temporal progression of internal erosion in cohesionless soil. *Canadian Geotechnical Journal*, **48**, 399–412, <https://doi.org/10.1139/T10-071>
- Moghri M., Garmabi H. and Akbarian M. (2003). Effect of processing parameters on fusion and mechanical properties of a twin-screw extruded rigid PVC pipe. *Journal of Vinyl and Additive Technology*, **9**, 81–89, <https://doi.org/10.1002/vnl.10067>
- Monteny J., Vincke E., Beeldens A., De Belie N., Taerwe L., Van Gemert D. and Verstraete W. (2000). Chemical, microbiological, and in situ test methods for biogenic sulfuric acid corrosion of concrete. *Cement and Concrete Research*, **30**, 623–634, [https://doi.org/10.1016/S0008-8846\(00\)00219-2](https://doi.org/10.1016/S0008-8846(00)00219-2)
- Moreno-Rodenas A. M., Duinmeijer S. P. A. and Clemens-Meyer F. (2021). Deep learning based monitoring of FOG layer dynamics in wastewater pumping stations. *Water Research*, **202**, 117482, <https://doi.org/10.1016/j.watres.2021.117482>
- Morris P. H., Graham J. and Williams D. J. (1992). Cracking in drying soils. *Canadian Geotechnical Journal*, **29**, 263–277, <https://doi.org/10.1139/t92-030>
- Mubarak I., Mailhol J. C., Angulo-Jaramillo R., Ruelle P., Boivin P. and Khaledian M. (2009). Temporal variability in soil hydraulic properties under drip irrigation. *Geoderma*, **150**, 158–165, <https://doi.org/10.1016/j.geoderma.2009.01.022>
- Najafi M. and Kulandaivel G. (2005). *Pipeline condition prediction using neural network models*. 767–781. Scopus, [https://doi.org/10.1061/40800\(180\)61](https://doi.org/10.1061/40800(180)61)
- Nehdi M. L., Mohamed, N. and Soliman A. (2016). Investigation of buried full-scale SFRC pipes under live loads. *Construction and Building materials*, (102), 733–742, <https://doi.org/10.1016/j.conbuildmat.2015.10.203>
- Nelder J. A. and Mead R. (1965). A simplex method for function minimization. *The Computer Journal*, **7**, 308–313, <https://doi.org/10.1093/comjnl/7.4.308>
- Neville A. (2004). The confused world of sulfate attack on concrete. *Cement and Concrete Research*, **34**(2004), 1275–1296, <https://doi.org/10.1016/j.cemconres.2004.04.004>
- Nguyen L. V., Bui D. T. and Seidu R. (2022). Comparison of machine learning techniques for condition assessment of sewer network. *IEEE Access*, **10**, 124238–124258, <https://doi.org/10.1109/ACCESS.2022.3222823>
- Nielsen D., Biggar J. and Erh K. (1973). Spatial variability of fieldmeasured soil-water properties. *Hilgardia*, **42**, 215–259, <https://doi.org/10.3733/hilg.v42n07p215>
- Nieuwenhuis E., Post J., Duinmeijer A., Langeveld J. and Clemens F. (2018). Statistical modelling of Fat, Oil and grease (FOG) deposits in wastewater pump sumps. *Water Research*, **135**, 155–167, <https://doi.org/10.1016/j.watres.2018.02.026>



- Nimmo J. R., Schmidt K. M., Perkins K. S. and Stock J. D. (2009). Rapid measurement of field-saturated hydraulic conductivity for areal characterization. *Vadose Zone Journal*, **8**, 142–149, <https://doi.org/10.2136/vzj2007.0159>
- North Carolina Department of Environmental Quality (NCDEQ) (2018). Stormwater Design Manual: <https://www.deq.nc.gov/about/divisions/energy-mineral-and-land-resources/stormwater/stormwater-program/stormwater-design-manual> (07/04/2023).
- O’Connell M., McNally C. and Richardson M. G. (2010). Biochemical attack on concrete in wastewater applications: a state of the art review. *Cement and Concrete Composites*, **32**, 479–485, <https://doi.org/10.1016/j.cemconcomp.2010.05.001>
- Olsson L., Barbosa H., Bhadwal S., Cowie A., Delusca K., Flores-Renteria D., Hermans K., Jobbagy E., Kurz W., Li D., Sonwa D. J. and Stringer L. (2019). Land degradation. In: Climate Change and Land: an IPCC Special Report on Climate Change, Desertification, Land Degradation, Sustainable Land Management, Food Security, and Greenhouse gas Fluxes in Terrestrial Ecosystems, P. R. Shukla, J. Skea, E. Calvo Buendia, V. Masson-Delmotte, H.-O. Pörtner, D. C. Roberts, P. Zhai, R. Slade, S. Connors, R. van Diemen, M. Ferrat, E. Haughey, S. Luz, S. Neogi, M. Pathak, J. Petzold, J. Portugal Pereira, P. Vyas, E. Huntley, K. Kissick, M. Belkacemi and J. Malley (eds), Cambridge University Press, Cambridge, UK, pp. 345–436, <https://doi.org/10.1017/9781009157988.006>
- Oral H. V., Carvalho P., Gajewska M., Ursino N., Masi F., Hullebusch E. D., van Kazak J. K., Exposito A., Cipolletta G., Andersen T. R., Finger D. C., Simperler L., Regelsberger M., Rous V., Radinja M., Buttiglieri G., Krzeminski P., Rizzo A., Dehghanian K., Nikolova M. and Zimmermann M. (2020). A review of nature-based solutions for urban water management in European circular cities: a critical assessment based on case studies and literature. *Blue-Green Systems*, **2**(1), 112–136, <https://doi.org/10.2166/bgs.2020.932>
- Ortega J., García-Vera V., Solak A. and Tenza-Abril A. (2019). Pore structure degradation of different cement mortars exposed to sulphuric acid. *Appl. Sci.*, **9**, 1–13.
- Panasiuk O., Hedström A., Marsalek J., Ashley R. M. and Viklander M. (2015). Contamination of stormwater by wastewater: a review of detection method. *Journal of Environment Management*, **152**, 241–250, <https://doi.org/10.1016/j.jenvman.2015.01.050>
- Parker C. D. (1945). The corrosion of concrete. *Australian Journal of Experimental Biology and Medical Science*, **23**, 81–90, <https://doi.org/10.1038/icb.1945.13>
- Paus K. H., Morgan J., Gulliver J. S., Leiknes T. and Hozalski R. M. (2014). Assessment of the hydraulic and toxic metal removal capacities of bioretention cells after 2 to 8 years of service. *Water, Air, and Soil Pollution*, **225**(1), 1–12.
- Pedregosa F., Varoquaux G., Gramfort A., Michel V., Thirion B., Grisel O., Blondel M., Prettenhofer P., Weiss R., Dubourg V., Vanderplas J., Passos A., Cournapeau D., Brucher M., Perrot M. and Duchesnay É (2011). Scikit-learn: machine learning in python. *Journal of Machine Learning Research*, **12**, 2825–2830. Scopus.
- Peter J. M., Chapman D., Moore I. D. and Hoult N. (2018). Impact of soil erosion voids on reinforced concrete pipe responses to surface loads. *Tunnelling and Underground Space Technology*, **82**, 111–124, <https://doi.org/10.1016/j.tust.2018.08.003>
- Petrucci G. (2012). La diffusion du contrôle à la source des eaux pluviales urbaines : confrontation des pratiques à la rationalité hydrologique. PhD, Ecole des Ponts et Chaussées- Université Paris Est, Paris France.
- Philip J. R. (1957). The theory of infiltration: 4 sorptivity and algebraic infiltration equations. *Soil Science*, **84**, 257–264, <https://doi.org/10.1097/00010694-195709000-00010>
- Poduška J., Hutař P., Kučera J., Frank A., Sadilek J., Pinter G. and Nahlík L. (2016). Residual stress in polyethylene pipes. *Polymer Testing*, **54**, 288–295, <https://doi.org/10.1016/j.polymertesting.2016.07.017>
- Poesen J. (2018). Soil erosion in the anthropocene: research needs. *Earth Surface Processes and Landforms*, **43**, 64–84, <https://doi.org/10.1002/esp.4250>
- Pothof I. W. M. (2011). Co-current air-water flow in downward sloping pipes. PhD thesis, Delft University of Technology. ISBN: 978-90-8957-018-5. <https://www.bing.com/search?q=Pothof%2C+I.W.M.+2011+co-current+air-water+flow+in+downward+sloping+pipes&cvid=1b3f4467f6b640889296b2a58b129d8f&aqs=edge..69i57.5508j0j4&FORM=ANAB01&PC=U531>
- Prima S. D., Stewart R. D., Najm M. R. A., Roder L. R., Giadrossich F., Campus S., Angulo-Jaramillo R., Yilmaz D., Roggero P. P., Pirastru M. and Lassabatere L. (2021). BEST-WR: an adapted algorithm for the hydraulic characterization of hydrophilic and water-repellent soils. *Journal of Hydrology*, **603**, 126936, <https://doi.org/10.1016/j.jhydrol.2021.126936>
- Proton A. (2008). Etude hydraulique des tranchées de rétention / infiltration. PhD, INSA Lyon, Villeurbanne, France, 299 p.

- Rabinovitch E. B. and Summers J. W. (1992). The effect of physical ageing on properties of rigid polyvinyl chloride. *Journal of Vinyl Technology*, **14**, 126–130, <https://doi.org/10.1002/vnl.730140303>
- Rajabipour F., Giannini E., Dunant C., Ideker J. H. and Thomas M. D. A. (2015). Alkali-silica reaction: current understanding of the reaction mechanisms and the knowledge gaps. *Cement and Concrete Research*, **76**, 130–146, <https://doi.org/10.1016/j.cemconres.2015.05.024>
- Rakitin B. and Xu M. (2014). Centrifuge modeling of large-diameter underground pipes subjected to heavy traffic loads. *Canadian Geotechnical Journal*, **51**, 353–368, <https://doi.org/10.1139/cgj-2013-0253>
- Reinhardt H. W. and Xu S. (2000). A practical testing approach to determine mode II fracture energy for concrete. *Int. J. Fract.*, **105**, 107–125, <https://doi.org/10.1023/A:1007649004465>
- Reynolds W. D. and Lewis J. K. (2012). A drive point application of the Guelph permeameter method for coarse-textured soils. *Geoderma*, **187–188**, 59–66, <https://doi.org/10.1016/j.geoderma.2012.04.004>
- Riks E. (1979). An incremental approach to the solution of snapping and buckling problems. *Int. Journal of Solids and Structures*, **15**(7), 529–551, [https://doi.org/10.1016/0020-7683\(79\)90081-7](https://doi.org/10.1016/0020-7683(79)90081-7)
- Rizzo P. (2010). Water and Wastewater Pipe Non-destructive Evaluation and Health Monitoring: A Review. *Advances in Civil Engineering*, **2010**, 818597, <https://doi.org/10.1155/2010/818597>
- Robeson L. M. (2013). Environmental stress cracking: a review. *Polymer Engineering & Science*, **53**, 453–467, <https://doi.org/10.1002/pen.23284>
- Robinson M. and Dean T. J. (1993). Measurement of near surface soil water content using a capacitance probe. *Hydrological Processes*, **7**, 77–86, <https://doi.org/10.1002/hyp.3360070108>
- Rodrigues-Iturbe I., Febres De Power B., Sharif M. B. and Georgakakos K. P. (1989). Chaos in rainfall. *Water Resources Research*, **25**(7), 1667–1675, <https://doi.org/10.1029/WR025i007p01667>
- Rokstad M. M. and Ugarelli R. M. (2015). Evaluating the role of deterioration models for condition assessment of sewers. *Journal of Hydroinformatics*, **17**(5), 789–804. Scopus, <https://doi.org/10.2166/hydro.2015.122>
- Rooyackers F. A. M., Bosco E., Suiker A. S. J. and Clemens F. H. L. R. (2022). A chemo-mechanical model for biogenic sulphide corrosion of concrete. *Cement and Concrete Research*, **160**, 106809, <https://doi.org/10.1016/j.cemconres.2022.106809>
- Saulais M. (2011). Colonisation végétale des bassins d'infiltration et de rétention : caractérisation de la flore et évolution des caractéristiques physico-chimiques de l'horizon de surface végétalisé. PhD, INSA, Lyon, France. <https://theses.hal.science/tel-00715802>.
- Saulais M., Bedell J. P. and Delolme C. (2011). Cd, Cu and Zn mobility in contaminated sediments from an infiltration basin colonized by wild plants: The case of *Phalaris arundinacea* and *Typha*.
- Savija B. and Lukovic M. (2016). Carbonation of cement paste: understanding, challenges, and opportunities. *Construction and Building Materials*, **117**, 285–301, <https://doi.org/10.1016/j.conbuildmat.2016.04.138>
- Scheperboer I. C., Luimes R. A., Suiker A. S. J., Bosco E. and Clemens F. H. L. R. (2021). Experimental-numerical study on the structural failure of concrete sewer pipes. *Tunnelling and Underground Space Technology*, **116**, 104075, <https://doi.org/10.1016/j.tust.2021.104075>
- Scheperboer I. C., Suiker A. S. J., Bosco E. and Clemens F. H. L. R. (2022). A coupled hydro-mechanical model for subsurface erosion with analysis of soil piping and void formation. *Acta Geotechnica*, **17**, 4769–4798, <https://doi.org/10.1007/s11440-022-01479-8>
- Schofield A. N. (1980). Cambridge geotechnical centrifuge operations. *Geotechnique*, **30**, 227–268, <https://doi.org/10.1680/geot.1980.30.3.227>
- Scholten F. L., van der Stok E., Gerets B., Wenzel M. and Boege M. (2016). Residual quality of excavated UPVC gas and water distribution pipelines. Proceedings of the 18th International Conference on Plastics Pipes, Berlin, Germany.
- Shaowei H., Qiyong Q. and Nina G. (2018). Effect of acid corrosion on crack propagation of concrete beams. *S'adhaña*, **43**, 1–23.
- Shawe-Taylor J. and Cristianini N. (2004). Kernel Methods for Pattern Analysis. Cambridge University Press, Cambridge, UK, <https://doi.org/10.1017/CBO9780511809682>
- Shi B., Catsamas S., Delectic B., Wang M., Bach P. M., Lintern A., Delectic A. and McCarthy D. T. (2022). Illicit discharge detection in stormwater drains using an arduino-based low-cost sensor network. *Water Science and Technology*, **85**(5), 1372–1383, <https://doi.org/10.2166/wst.2022.034>
- Siegmann A., Buchman A. and Kenig S. (1981). Residual stresses in polymers. II. Their effect on mechanical behaviour. *Polymer Engineering and Science*, **21**, 997–1002, <https://doi.org/10.1002/pen.760211503>
- Siegmann A., Buchman A. and Kenig S. (1982). Residual stresses in polymers I: The effect of thermal history. *Polymer Engineering and Science*, **22**, 40–47, <https://doi.org/10.1002/pen.760220107>

- Silva A., Nascimento N., Seidl M. and Vieira L. (2010). SWITCH in Belo Horizonte, Brazil: infiltration and detention systems for more sustainable stormwater control in Belo Horizonte. *Reviews of Environmental Science and Biotechnology*, **9**, 7–13, <https://doi.org/10.1007/s11157-010-9196-5>
- Šimůnek J., Jarvis N. J., van Genuchten M. T. and Gärdenäs A. (2003). Review and comparison of models for describing non-equilibrium and preferential flow and transport in the vadose zone. *Journal of Hydrology*, **272**, 14–35, [https://doi.org/10.1016/S0022-1694\(02\)00252-4](https://doi.org/10.1016/S0022-1694(02)00252-4)
- Šimůnek J., Šejna M., Saito H. and Van Genuchten M. T. (2008). The HYDRUS-1D software package for simulating the movement of water, heat, and multiple solutes in variably saturated media. *HYDRUS Softw. Ser.*, **3**.
- Šimůnek J., van Genuchten M. Th. and Šejna M. (2016). Recent developments and applications of the HYDRUS computer software packages. *Vadose Zone Journal*, **15**, 1–25, <https://doi.org/10.2136/vzj2016.04.0033>
- Siriwardene N., Deletic A. and Fletcher T. D. (2007). Clogging of stormwater gravel infiltration systems and filters: insights from a laboratory study. *Water Research*, **41**(7), 1433–1440, <https://doi.org/10.1016/j.watres.2006.12.040>
- Sivakumar B., Berndtsson J., Olsson J. and Jinno K. (2009). Evidence of chaos in the rainfall-runoff process. *Hydrological Sciences Journal*, **46**(1), 131–145, <https://doi.org/m10.1080/02626660109492805>
- Skorobogatov A. (2014). Hydrological Functionality of Plants and Its Application to Stormwater Management. Master's thesis, University of Calgary, Calgary, Canada. Retrieved from <https://prism.ucalgary.ca>, <https://doi.org/10.11575/PRISM/26403>
- Smakhtin V. U. (2001). Low flow hydrology: a review. *Journal of Hydrology*, **240**, 147–186, [https://doi.org/10.1016/S0022-1694\(00\)00340-1](https://doi.org/10.1016/S0022-1694(00)00340-1)
- Sousa V., Matos J. P. and Matias N. (2014). Evaluation of artificial intelligence tool performance and uncertainty for predicting sewer structural condition. *Automation in Construction*, **44**, 84–91. Scopus, <https://doi.org/10.1016/j.autcon.2014.04.004>
- Stajanca P., Chruscicki S., Homann T., Seifert S., Sschmidt D. and Habib A. (2019). Detection of leak-induced pipeline vibrations using fiber optic distributed acoustic sensing. *Sensors*, **18**, 2841, <https://doi.org/10.3390/s18092842>
- Stanic N., de Haan C., Tirion M., Langeveld J. G. and Clemens F. H. L. R. (2013). Comparison of core sampling and visual inspection for assessment of concrete sewer pipe condition. *Water Science and Technology*, **67**, 2458–2466, <https://doi.org/10.2166/wst.2013.138>
- Stanic N., Langeveld J., Salet T. and Clemens F. (2017). Relating the structural strength of concrete sewer pipes and material properties retrieved from core samples. *Structure and Infrastructure Engineering*, **13**, 637–651, <https://doi.org/10.1080/15732479.2016.1187631>
- Struik L. C. E. (1977). Physical aging in amorphous polymers and other materials. Doctoral dissertation, Delft University of Technology, The Netherlands. Retrieved from <http://resolver.tudelft.nl/uuid:941d2af6-903a-4260-9953-2efb4cb38d2e>
- Syachrani S., Jeong H. S. and Chung C. S. (2013). Decision tree-based deterioration model for buried wastewater pipelines. *Journal of Performance of Constructed Facilities*, **27**(5), 633–645, [https://doi.org/10.1061/\(ASCE\)CF.1943-5509.0000349](https://doi.org/10.1061/(ASCE)CF.1943-5509.0000349)
- Talesnick M. and Baker R. (1999). Investigation of the failure of a concrete-lined steel pipe. *Geotechnical and Geological Engineering*, **17**, 99–121, <https://doi.org/10.1023/A:1008913408452>
- Tan Z. (2007). Nonlinear finite element study of deteriorated sewers including the influence of erosion voids. Master's thesis, Queen's University, Kingston, Ontario, Canada.
- Toronto and Region Conservation Authority (TRCA) (2016). Low Impact Development Stormwater Management Practice Inspection and Maintenance Guide. <https://sustainabletechnologies.ca/app/uploads/2016/08/LID-IM-Guide-2016-1.pdf> (07/04/2023).
- Tran H., Perera B. and Ng A. (2007). Neural Network Based Prediction Models For Structural Deterioration of Urban Drainage Pipes. MODSIM07 – Land, Water and Environmental Management: Integrated Systems for Sustainability, Proceedings.
- Trautmann C. H. and O'Rourke T. D. (1985). Lateral force-displacement response of buried pipe. *Journal of Geotechnical Engineering*, **111**, 1077–1092, [https://doi.org/10.1061/\(ASCE\)0733-9410\(1985\)111:9\(1077\)](https://doi.org/10.1061/(ASCE)0733-9410(1985)111:9(1077))
- Tscheikner-Gratl F., Caradot N., Cherqui F., Leitão J. P., Ahmadi M., Langeveld J. G., Le Gat Y., Scholten L., Roghani B., Rodríguez J. P., Lepot M., Stegeman B., Heinrichsen A., Kropp I., Kerres K., Almeida M. D. C., Bach P. M., Moy de Vitry M., Sá Marques A., ... Clemens F. (2019). Sewer asset management—state of the art and research needs. *Urban Water Journal*, **16**(9), 662–675. Scopus, <https://doi.org/10.1080/1573062X.2020.1713382>

- Tu J. V. (1996). Advantages and disadvantages of using artificial neural networks versus logistic regression for predicting medical outcomes. *Journal of Clinical Epidemiology*, **49**(11), 1225–1231. Scopus, [https://doi.org/10.1016/S0895-4356\(96\)00002-9](https://doi.org/10.1016/S0895-4356(96)00002-9)
- Tukker M., Kooij C. and Pothof I. (2016). Hydraulic Design and Management of Wastewater Transport Systems. IWA Publishing, London, UK, <https://doi.org/10.2166/9781780407814>
- Utsi E. C. (2017). Ground Penetrating Radar: Theory and Practice. Butterworth-Heinemann.
- Valdelfener M., Barraud S., Sibeud E., Bacot L., Perrin Y., Jourdain F. and Marmonier P. (2018). Do sustainable drainage systems favour mosquito proliferation in cities compared to stormwater networks? *Urban Water Journal*, **16**(6), 436–443, <https://doi.org/10.1080/1573062X.2018.1523442>
- Van Bijnen M. (2018). The impact of sewer condition on the performance of sewer systems. PhD thesis, Delft University of Technology. ISBN 978-94-6233-987-3.
- Van Bijnen M., Korving H. and Clemens F. (2012). Impact of sewer condition on urban flooding: an uncertainty analysis based on field observations and Monte Carlo simulations on full hydrodynamic models. *Water Science and Technology*, **65**, 2219–2227, <https://doi.org/10.2166/wst.2012.134>
- Van Bijnen M., Korving H., Langeveld J. and Clemens F. (2016). Calibration of hydrodynamic model driven sewer maintenance. *Structure and Infrastructure Engineering*, **13**, 1167–1185, <https://doi.org/10.1080/15732479.2016.1247287>
- Van Bijnen M., Korving H., Langeveld J. and Clemens F. (2018). Quantitative impact assessment of sewer condition on health risk. *Water*, **10**(3), 245, <https://doi.org/10.3390/w10030245>
- Van Duin B. (2023). Private communication on clogging of geotextiles in practical UDAM applications.
- Van Duin B., Brown C., Chu A., Marsalek J. and Valeo C. (2008). Characterization of long-term solids removal and clogging processes in two types of permeable pavement under cold climate conditions. 11th International Conference on Urban Drainage, Edinburgh, pp. 1–10.
- Van Genuchten M. T. (1980). A closed-form equation for predicting the hydraulic conductivity of unsaturated soils. *Soil Science Society of America Journal*, **44**, 892–898, <https://doi.org/10.2136/sssaj1980.03615995004400050002x>
- van Riel W. A. P. (2016). On decision-making for sewer replacement. PhD thesis Delft University of Technology. ISBN:978-94-6233-327-7, <https://doi.org/10.4233/uuid:92b10448-795d-43ac-8071-d779af9d374d>
- van Riel W., Langeveld J., Herder P. and Clemens F. (2016). The influence of information quality on decision making for networked infrastructure management. *Structure and Infrastructure Engineering*, **13**(6), 1–13, <https://doi.org/10.1080/15732479.2016.1187633>
- van Schaik N. L. M. B., Hendriks R. F. A. and van Dam J. C. (2010). Parameterization of macropore flow using dye-tracer infiltration patterns in the SWAP model. *Vadose Zone Journal*, **9**, 95, <https://doi.org/10.2136/vzj2009.0031>
- Verachert E., Maetens W., Van Den Eeckhaut M., Poesen J. and Deckers J. (2011). Soil loss rates due to piping erosion. *Earth Surface Processes and Landforms*, **36**, 1715–1725, <https://doi.org/10.1002/esp.2186>
- Verruijt A. and van Baars S. (2007). Soil Mechanics. VSSD, Delft, the Netherlands.
- Virahsawmy H., Stewardson M., Vietz G. and Fletcher T. (2014). Factors that affect the hydraulic performance of raingardens: implications for design and maintenance. *Water Science & Technology*, **69**(5), 982–988, <https://doi.org/10.2166/wst.2013.809>
- Visser H. A. (2009). Residual lifetime assessment of uPVC gas pipes, PhD Thesis University of Twente, <https://doi.org/10.3990/1.9789036529587>.
- Visser H. A., Bor T. C., Wolters M., Warnet L. L. and Govaert L. E. (2011). Influence of physical aging on impact embrittlement of uPVC pipes. *Plastics, Rubber and Composites*, **40**, 201–212, <https://doi.org/10.1179/1743289810Y.0000000021>
- Vollertsen J., Nielsen A. H., Jensen H. S., Wium-Andersen T. and Hvitved-Jacobsen T. (2008). Corrosion of concrete sewers – the kinetics of hydrogen sulfide oxidation. *Science of The Total Environment*, **394**, 162–170, <https://doi.org/10.1016/j.scitotenv.2008.01.028>
- Waltham T., Bell F. G. and Culshaw M. G. (2005). Sinkholes and Subsidence – Karst and Cavernous Rocks in Engineering and Construction. Springer-Verlag, Berlin-Heidelberg-New York.
- Wang Z., Wu Q. J., Wu L., Ritsema C. J., Dekker L. W. and Feyen J. (2000). Effects of soil water repellency on infiltration rate and flow instability. *Journal of Hydrology*, **231–232**, 265–276, [https://doi.org/10.1016/S0022-1694\(00\)00200-6](https://doi.org/10.1016/S0022-1694(00)00200-6)
- Wang J., Huang H., Xie X. and Bobet A. (2014). Void-induced liner deformation and stress redistribution. *Tunnelling and Underground Space Technology*, **40**, 263–276, <https://doi.org/10.1016/j.tust.2013.10.008>



- Watlet A., Kaufmann O., Triantafyllou A., Poulain A., Chambers J. E., Meldrum P. I., Wilkinson P. B., Hallet V., Quinif Y., Van Ruymbeke M. and Van Camp M. (2018). Imaging groundwater infiltration dynamics in the karst vadose zone with long-term ERT monitoring. *Hydrology and Earth System Sciences*, **22**, 1563–1592, <https://doi.org/10.5194/hess-22-1563-2018>
- Werey C., Cherqui F., Le Nouveau N., Rodriguez F., Sibeud E., Joannis C. and Barraud S. (2016). Asset management of Best Management Practices: a new story for urban stormwater management (Gestion patrimoniale des techniques alternatives : une nouvelle histoire à écrire pour la gestion des eaux pluviales en ville). 9th International Conference Novatech, Lyon, France.
- Whalley W. R. (1993). Considerations on the use of time-domain reflectometry (TDR) for measuring soil water content. *Journal of Soil Science*, **44**, 1–9, <https://doi.org/10.1111/j.1365-2389.1993.tb00429.x>
- Willard L. L., Wynn-Thompson T., Krometis L. H., Neher T. P. and Badgley B. D. (2017). Does it pay to be mature? Evaluation of bioretention cell performance seven years postconstruction. *J. Environ. Eng.*, **143**(9), 04017041, [https://doi.org/10.1061/\(ASCE\)EE.1943-7870.0001232](https://doi.org/10.1061/(ASCE)EE.1943-7870.0001232)
- Winston R., Al-Rubaei A., Blecken G.-T., Viklander M. and Hunt W. (2016). Maintenance measures for preservation and recovery of permeable pavement surface infiltration rate – the effects of street sweeping, vacuum cleaning, high pressure washing, and milling. *Journal of Environmental Management*, **169**, 132–144, <https://doi.org/10.1016/j.jenvman.2015.12.026>
- Wirahadikusumah R., Abraham D. and Iseley T. (2001). Challenging issues in modeling deterioration of combined sewers. *Journal of Infrastructure Systems*, **7**, 77–84, [https://doi.org/10.1061/\(ASCE\)1076-0342\(2001\)7:2\(77\)](https://doi.org/10.1061/(ASCE)1076-0342(2001)7:2(77))
- Wolpert D. H. and Macready W. G. (1997). No free lunch theorems for optimization. *IEEE Transactions on Evolutionary Computation*, **1**(1), 67–82, <https://doi.org/10.1109/4235.585893>
- Xu X. P. and Needleman A. (1994). Numerical simulations of fast crack growth in brittle solids. *Journal of the Mechanics and Physics of Solids*, **42**, 1397–1434, [https://doi.org/10.1016/0022-5096\(94\)90003-5](https://doi.org/10.1016/0022-5096(94)90003-5)
- Xu M. and Shen D. (2020). The influence of erosion voids on the longitudinal behaviour of a jointed large-diameter reinforced concrete pipeline. *Tunnelling and Underground Space Technology*, **103**, 103494, <https://doi.org/10.1016/j.tust.2020.103494>
- Xu M., Shen D. and Rakitin B. (2017). The longitudinal response of buried large-diameter reinforced concrete pipeline with gasketed bell-and-spigot joints subjected to traffic loading. *Tunnelling and Underground Space Technology*, **64**, 117–132, <https://doi.org/10.1016/j.tust.2016.12.020>
- Yang J., Yin Z. Y., Laouafa F. and Hicher P. Y. (2019). Internal erosion in dike-on-foundation modeled by a coupled hydromechanical approach. *International Journal for Numerical and Analytical Methods in Geomechanics*, **43**, 663–683, <https://doi.org/10.1002/nag.2877>
- Yang F., Fu D., Zevenbergen C. and Rene E. A. (2022). Comprehensive review on the long-term performance of stormwater biofiltration systems (SBS): operational challenges and future directions. *Journal of Environmental Management*, **302**, 113956, <https://doi.org/10.1016/j.jenvman.2021.113956>
- Yasuda N., Tsukada K. and Asakura T. (2017). Elastic solutions for circular tunnel with void behind lining. *Tunnelling and Underground Space Technology*, **70**, 274–285, <https://doi.org/10.1016/j.tust.2017.08.032>
- Yilmaz D., Lassabatere L., Deneele D., Angulo-Jaramillo R. and Legret M. (2013). Influence of carbonation on the microstructure and hydraulic properties of a basic oxygen furnace slag. *Vadose Zone Journal*, **12**, 1–15, <https://doi.org/10.2136/vzj2012.0121>
- Yilmaz D., Di Prima S., Stewart R. D., Abou Najm M. R., Fernandez-Moret D., Latorre B. and Lassabatere L. (2022). Three-term formulation to describe infiltration in water-repellent soils. *Geoderma*, **427**, 116127, <https://doi.org/10.1016/j.geoderma.2022.116127>
- Younis A., Ramadan A., Wong L. and Nehdi M. (2020). New rational test for reinforced-concrete pipe eliminating subjective crack-width criteria. *Structures*, (28), 2507–2522, <https://doi.org/10.1016/j.istruc.2020.10.076>
- Zaqout T., Ólöf Andradóttir H. and Arnalds Ó (2022). Infiltration capacity in urban areas undergoing frequent snow and freeze-thaw cycles: implications on sustainable urban drainage systems. *Journal of Hydrology*, **607**, 127495, <https://doi.org/10.1016/j.jhydrol.2022.127495>
- Zeng X., Wang Z., Wang H., Zhu S. and Chen S. (2023). Progress in drainage pipeline condition assessment and deterioration prediction models. *Sustainability*, **15**(4), Article 4, <https://doi.org/10.3390/su15043849>
- Zhang S., Liu B. and He J. (2019). Pipeline deformation monitoring using distributed fiber optical sensor. *Measurement*, **133**, 208–213, <https://doi.org/10.1016/j.measurement.2018.10.021>
- Zhao K., Xu Q., Liu F., Xiu D. and Ren X. (2020a). Field monitoring of preferential infiltration in loess using time-lapse electrical resistivity tomography. *Journal of Hydrology*, **591**, 125278, <https://doi.org/10.1016/j.jhydrol.2020.125278>



## 230 Asset Management of Urban Drainage Systems: if anything exciting happens, we've done it wrong!

- Zhao S., Jia Y., Gong J., Niu C., Su H., Gan Y. and Liu H. (2020b). Spatial variability of preferential flow and infiltration redistribution along a rocky-mountain hillslope, northern China. *Water*, **12**, 1102, <https://doi.org/10.3390/w12041102>
- Zoladz G. V., McGrath T. J. and Selig E. T. (1996). Laboratory tests of buried pipe installation procedures. *Transportation Research Record: Journal of the Transportation Research Board*, **1541**, 86–96, <https://doi.org/10.1177/0361198196154100111>